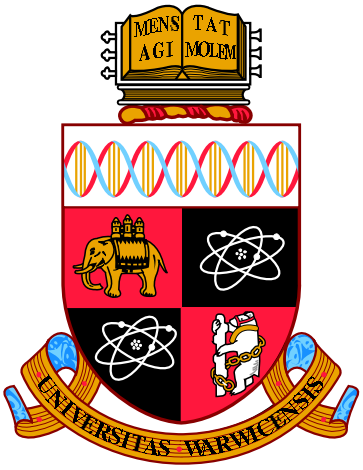

Ultrafast Spectroscopy of Metal Halide Perovskites and III-V Semiconductors

by

Maurizio Monti

Thesis

Submitted to the University of Warwick

for the degree of

Doctor of Philosophy in Physics

University of Warwick, Department of Physics

April 2020

Contents

List of Tables

List of Figures

Acknowledgments

I would like to thank first and foremost my supervisor Dr. James Lloyd-Hughes for his help, support, guidance and the patience he showed in these years.

Special thanks go to Dr. Michael Staniforth who taught me how to properly align a laser, provided invaluable support and rescued me countless times in the lab.

Thanks to the people who made possible this thesis by providing good quality samples: Anjana Wijesekara, Prof. Ross Hatton, Dr. Imalka Jayawardena, Chapa Bandara, Prof. Ravi Silva and Dr. Mark Ashwin.

Thanks to the people who helped me by collecting the complementary data that I needed to complete this work: Edward Butler-Caddle, Adam Crocker and Edward Griffin. Thanks also to Dr. ShuXia Tao for her DFT calculations.

Great thanks go to the THz group in Warwick, which now got so big I can't name them all, but the people have provided useful discussions, help, and a great environment to work in. I would particularly like to thank Dr. Michele Failla and Dr. Connor Mosley for mentoring, helping and advising me. Thanks also to Maria Burdanova for being a great colleague in these almost four years.

I would like to thank all the friends I have made in these years in Coventry, for their support and the great time spent together, unfortunately I don't have the space to name them all.

Great thanks have to go to my older friends, who even from faraway kept supporting me: Jack, Orso, Sara, Luca, Pellic, and also Canta, Sca, Manta, Costa, and Onofrio.

Finally all of this could not have been possible without the help and support from my wonderful parents and my little brother (who is not so little anymore) to whom this work is dedicated.

Grazie a tutti!

This thesis was typeset with LaTeX 2$_\varepsilon$[1] by the author.

[1] LaTeX 2$_\varepsilon$ is an extension of LaTeX. LaTeX is a collection of macros for TeX. TeX is a trademark of the American Mathematical Society. The style package *warwickthesis* was used.

Declarations

I declare that this thesis has been composed by myself and has not been submitted in any previous application for any degree. The work reported in this thesis was carried out by myself, except in the cases outlined below, under the supervision of Dr. James Lloyd-Hughes between 2016 and 2020 at the University of Warwick.

The $CsSnI_3$, $Rb_{0.1}Cs_{0.9}SnI_3$ and $Rb_{0.2}Cs_{0.8}SnI_xBr_{1-x}$ samples used in chapter 4 were prepared by Anjana Wijesekara and Dr. Ross A. Hatton at the department of Chemistry at the University of Warwick. The $Cs_{0.05}(FA_{0.83}MA_{0.17})_{0.95}Pb_xSn_{1-x}I_3$ and $Cs_{0.05}(FA_{0.83}MA_{0.17})_{0.95}Pb(I_{0.83}Br_{0.17})_3$ samples in chapter 5 were prepared by Dr. K.D.G Imalka Jayawardena, Rajapakshe M. I. Bandara and Prof. S. Ravi P. Silva at the Advanced Technology Institute at the University of Surrey. The InSb and $Al_{0.05}In_{0.95}Sb$ samples in chapter 6 were made by Dr. Mark Ashwin at the University of Warwick.

The photoluminescence spectra in chapter 4 were acquired by Adam Crocker and Edward Griffin, under the supervision of Dr. Michael Staniforth at the University of Warwick. The DFT calculations in chapter 4 were performed by Dr. Shuxia Tao at the Eindhoven University of Technology and analysed by Dr. James Lloyd-Hughes. The photoluminescence and absorbance spectra in chapter 5 were acquired by Edward Butler-Caddle at the University of Warwick and analysed by myself. The terahertz cyclotron spectroscopy experiments in chapter 6 were performed by myself and Chelsea Xia in Prof. Michael B. Johnston's laboratory at the University of Oxford and analysed by myself.

Parts of this thesis have been published by the author, as described in the relevant chapters.

Publications

The following is a list of the publications I have contributed to during my PhD, in reverse chronological order:

1. **M. Monti**, K. D. G. I. Jayawardena, E. Butler-caddle, R. M. I. Bandara, J. M. Woolley, M. Staniforth, S. R. P. Silva, and J. Lloyd-Hughes, *Hot carriers in mixed Pb-Sn halide perovskite semiconductors cool slowly while retaining their electrical mobility*, under writing.

2. D. J. L. Coxon, M. Staniforth, B. G. Breeze, E. Greenough, J. P. Goss, **M. Monti**, J. Lloyd-Hughes, V. G. Stavros, M. E. Newton, *An ultrafast shakedown reveals the energy landscape, relaxation dynamics and concentration of N_3VH defects in diamond*, Journal of Physical Chemistry Letters, submitted

3. K. D. G. I. Jayawardena, R. M. I.Bandara, **M. Monti**, E. Butler-Caddle, T. Pichler, H. Shiozawa, Z. Wang, S. J.Hinder, M. G. Masteghin, M. Patel, H. M. Thirimanne, W. Zhang, R. A. Sporea, J. Lloyd-Hughes, S. R. P. Silva, *Approaching the Shockley-Queisser limit for fill factors in lead-tin mixed perovskite photovoltaics*, Journal of materials chemistry A, 2020, **8**, pp 693-705.

4. M. G. Burdanova, A. P. Tsapenko, D. A. Satco, R. Kashtiban, C. D. W. Mosley, **M. Monti**, M. Staniforth, J. Sloan, Y. G. Gladush, A. G. Nasibulin, J. Lloyd-Hughes, *Efficient ultrafast THz modulators based on negative photoconductivity in controllably doped carbon nanotubes*,2019 44th International Conference on Infrared, Millimeter, and Terahertz Waves (IRMMW-THz), Paris, France, 2019, pp. 1-1.

5. **M. Monti**, J. M. Woolley, E. Butler-Caddle, M. Staniforth, A. Wijesekara, S. X. Tao, R. M. I. Bandara, K. D. G. I. Jayawardena, A. Crocker, E. Griffin, S. R. P. Silva, R. A. Hatton and J. Lloyd-Hughes, *Rapid Hot Carrier Relaxation and mobility increase in Sn- and Pb-containing Halide perovskite semiconductors*, CLEO/EQEC, paper jsiii_1_2, 2019.

6. M. G. Burdanova, A. P. Tsapenko, R. Kashtiban, J. Sloan, C. D. W. Mosley, **M. Monti**, M. Staniforth, Y. G. Gladush, A. G. Nasibulin and J. Lloyd-Hughes, *Giant negative photoconductivity in controllably-doped carbon nanotube networks*, ACS Photonics, 2019, **6**(4), pp 1058-1066.

7. **M. Monti**, J. M. Woolley, M. Staniforth, A. Wijesekara, S. X. Tao, R. M. I. Bandara, K. D. G. I. Jayawardena, A. Crocker, E. Griffin, S. R. P. Silva, R. A. Hatton and J. Lloyd-Hughes, *Efficient Intraband Hot Carrier Relaxation in Sn and Pb Pervoskte Semiconductors mediated by Strong Electron-phonon Coupling*, Proc. SPIE, 10916, pp. 109160M, 2019.

8. **M. Monti**, S. X. Tao, M. Staniforth, A. Crocker, E. Griffin, A. Wijesekara, R. A. Hatton and J. Lloyd-Hughes, *Efficient Intraband Hot Carrier Relaxation in the Perovskite Semiconductor* $Cs_{1x}Rb_xSnI_3$ *Mediated by Strong Electron-Phonon Coupling*, J. Phys. Chem. C, 2018, **122**(36), pp 20669-20675.

The following is a list of all my conference presentations in reverse chronological order, the * denotes the presenter.

1. Contributed talk *Influence of lead and tin concentration on hot carrier cooling in mixed lead-tin perovskite semiconductors*, **M. Monti***, E. Butler-Caddle, M. Staniforth, R.M.I. Bandara, I. Jayawardena, S. R. P. Silva and J. Lloyd-Hughes, 5th conference on Perovskite Solar Cells and Optoelectronics, Lausanne (SWI), September 2019

2. Contributed talk *Probing Hot Carrier Relaxation in Sn and Pb containing halide Perovskite Semiconductors*, **M. Monti***, J. A. Woolley, M. Staniforth, A. Wijesekara, S. X. Tao, R.M.I. Bandara, I. Jayawardena, A. Crocker, E.

Griffin, S. R. P. Silva, R. A. Hatton and J. Lloyd-Hughes, Condensed Matter and Quantum Materials conference, St. Andrews (UK), July 2019

3. Contributed talk *Rapid Hot Carrier Relaxation and mobility increase in Sn and Pb containing halide Perovskite Semiconductors*, **M. Monti***, J. A. Woolley, M. Staniforth, A. Wijesekara, S. X. Tao, R.M.I. Bandara, I. Jayawardena, A. Crocker, E. Griffin, S. R. P. Silva, R. A. Hatton and J. Lloyd-Hughes, CLEO/Europe-EQEC 2019, Munich (GER), June 2019

4. Invited Talk: *Hot carrier cooling in tin- and lead-based metal halide perovskites* **M. Monti**, J. A. Woolley, M. Staniforth, A. Wijesekara, S. X. Tao, R.M.I. Bandara, I. Jayawardena, S. R. P. Silva, R. A. Hatton, R. L. Milot and J. Lloyd-Hughes*, CLEO 2019, San Jose (California, US), May 2019

5. Poster: *Efficient Intraband Hot Carrier Relaxation in Sn and Pb Perovskite Semiconductors Mediated by Strong Electron-phonon Coupling*, **M. Monti***, J. A. Woolley, M. Staniforth, A. Wijesekara, S. X. Tao, R.M.I. Bandara, I. Jayawardena, A. Crocker, E. Griffin, S. R. P. Silva, R. A. Hatton and J. Lloyd-Hughes, Optical Terahertz Science and Technology 2019, Santa Fe (New Mexico, US), March 2019

6. Contributed talk: *Efficient Intraband Hot Carrier Relaxation in Sn and Pb Perovskite Semiconductors Mediated by Strong Electron-phonon Coupling*, **M. Monti***, J. A. Woolley, M. Staniforth, A. Wijesekara, S. X. Tao, R.M.I. Bandara, I. Jayawardena, A. Crocker, E. Griffin, S. R. P. Silva, R. A. Hatton and J. Lloyd-Hughes, SPIE Photonics West 2019, Ultrafast Phenomena and Nanophotonics XXIII, San Francisco (US), February 2019

7. Poster: *Efficient Intraband Hot Carrier Relaxation in the Perovskite Semiconductor Cs1xRbxSnI3 Mediated by Strong ElectronPhonon Coupling*, **M. Monti**, S. X. Tao, M. Staniforth, A. Crocker, E. Griffin, A. Wijesekara, R. Hatton and J. Lloyd-Hughes, THz instrumentation and applications workshop, University of Warwick (Coventry), December 2018

Abstract

A key phenomenon to improve even further the efficiency of photovoltaic technology is hot carrier dynamics: the possibility of harvesting hot, energetic carriers in photovoltaics could increase the efficiency of such devices beyond the Shockley-Queisser limit.

In this thesis advances in the understanding of hot carrier dynamics in metal halide perovskite semiconductors (MHP) are reported: the influence of the composition on the hot carrier cooling process was investigated by means of optical pump terahertz probe spectroscopy (OPTP) and transient absorption spectroscopy (TA). In particular the role of the metal in controlling the electron-phonon coupling and phonon-phonon coupling was studied.

A new phenomenological model aimed at describing the cooling dynamics of hot carriers is introduced, and its parameter linked to the microscopical physical processes underlying energy relaxation.

A fully inorganic tin-based perovskite semiconductor is studied using OPTP and the hot carrier cooling time connected to the first stage of cooling is measured, compared to the prototypical III-V semiconductor GaAs, and linked to the Fröhlich electron-LO phonon interaction. The influence of the bandstructure on the dynamics is also assessed.

A series of mixed lead-tin perovskites with controlled Pb/Sn ratio is investigated by both OPTP and TA spectroscopy. The numerical outcome of the two techniques is investigated and the differences linked to the different physical processes the two techniques probe, helping clarify discrepancies that appeared in previous works on the subject. The influence of the metal fraction on the cooling dynamic is also established, and linked to the modification of the electron-phonon and phonon-phonon interaction caused by alloying.

Finally the simpler, narrow-gap semiconductor InSb is studied for the first time via terahertz cyclotron spectroscopy. The effective mass of InSb was measured during the cooling of hot carriers towards the band edge, finding that the change in effective mass during this process is indeed measurable and can be described by a simple model assuming a nonparabolic band dispersion.

These findings suggest possible new directions for the design and implementation of future of future semiconductor materials and devices with optimised carrier cooling profiles.

Abbreviations

BGR	Band gap renormalization
EM	Electromagnetic
ESC	Energy selective contacts
GSB	Ground state bleach
HC	Hot carrier
HCC	Hot carrier cooling
HCSC	Hot carrier solar cell
LED	Light emitting diode
LL	Landau levels
MHP	Metal halide perovskites
MBS	Moss-Burstein shift
MPP	Maximum power point
NSR	Non-spectrally-resolved
OC	Open circuit
OPTP	Optical pump terahertz probe
PIA	Photoinduced absorption

PSC	Perovskite solar cell
PV	Photovoltaic
SC	Short circuit
SQ	Shockley-Queisser
SR	Spectrally-resolved
SRH	Shockley-Read-Hall
TA	Transient absorption
TCS	Terahertz cyclotron spectroscopy
THz	Terahertz

Chapter 1

Metal halide perovskite photovoltaics

To understand the importance of the work reported in this thesis, it is necessary to provide an overview of the field of solar cells, and how and why metal halide perovskites (MHP) stole the scene in a matter of a few years. This chapter aims to do exactly that: first by giving a general introduction on the theory of solar cells (section 1.1), secondly to explain what MHPs are, and why they are important (section 1.2), and, finally, a detailed description of the current state-of-the-art for the research on hot carriers in MHP is given in section 1.3. The concepts developed in this chapter will be useful to understand the results presented in subsequent chapters.

1.1 Theory of solar cells

1.1.1 Solar cells: a quest for efficiency

To find a sustainable energy source is one of the most important challenges in the recent history of humankind. Solar power may provide clean, sustainable energy: in one hour more energy falls on earth from the sun than is used by everyone in the world in one year. Making the best use of this energy would completely change our energy production landscape. For this reason scientists have tried for decades to harvest this energy, and most of their efforts focused on devices using the photovoltaic effect. The photovoltaic effect is the generation of a voltage and a current in a material under the exposure of light. It was first discovered by Edmond Becquerel in 1839[1]. From a modern physics picture the photovoltaic effect consists in a photon being absorbed and generating an electron-hole pair which can then give

rise to a photocurrent. A good description of the fundamentals of light absorption and emission are given in standard semiconductor physics books[2], or in books discussing the physics of solar cell devices[3, 4]. In order to understand some of the discussions that will follow it is necessary to introduce few basic concepts and definitions regarding the basics of semiconductor physics and the theory of solar cells.

It is well-known that a semiconducting material will absorb incident light only when said light (*i.e.* photons) have an energy, E_{photon}, larger than the semiconductor band gap, E_g. In this case the electron-hole pair will be generated at an energy higher than the band gap within the bandstructure (the exact energy distribution between the two carriers will depend on the specific bandstructure) and will dissipate the excess energy by exchanging heat with the lattice. The excess energy is defined as $E_{ex} = E_{photon} - E_g$. This process is extremely relevant for solar cell operation as this is one of the major causes of efficiency loss in solar cells and it is as such investigated in this work. It will be discussed further in the following sections.

The theory of solar cells is a wide and interesting topic, here only few basic concepts will be given, and the interested reader can find numerous books on the topic[3, 4] and article reviews, especially regarding perovskite solar cells[5]. The simplest way to describe a solar cell is by using a simple diode model[4]. The typical rectification current density-voltage characteristic of a diode (j-V) is: $j = j_0 \left(e^{eV/mk_BT}\right)$, where V is the voltage, e is the elementary charge, k_B is the Boltzmann constant, T is the temperature, m is the ideality factor and j_0 is the reverse saturation current. From the diode characteristic, assuming a photocurrent density j_{ph} (arising from the incident radiation) and a recombination current density j_{rec}, the total current can be calculated:

$$j = j_{ph} - j_{rec} + j_0. \tag{1.1}$$

Knowing that the recombination current of such a device is $j_{rec} = j_0 e^{qV/mk_BT}$, then the current-voltage (j-V) characteristic of a solar cell can be expressed as:

$$j = j_{ph} - j_0 \left(e^{eV/mk_BT} - 1\right). \tag{1.2}$$

An example of such a characteristic is reported in Figure 1.1 (a), the corresponding electrical power generated by the device, $P = j \times V$, is reported in panel (b). From the plot is possible to identify three main important points: the short-circuit point, the open-circuit point and the maximum power-point. The short-circuit point is defined as the point where the applied voltage is 0 and $j_{rec} = j_0$, and all the generated carriers contribute to the external current. The current at this point is

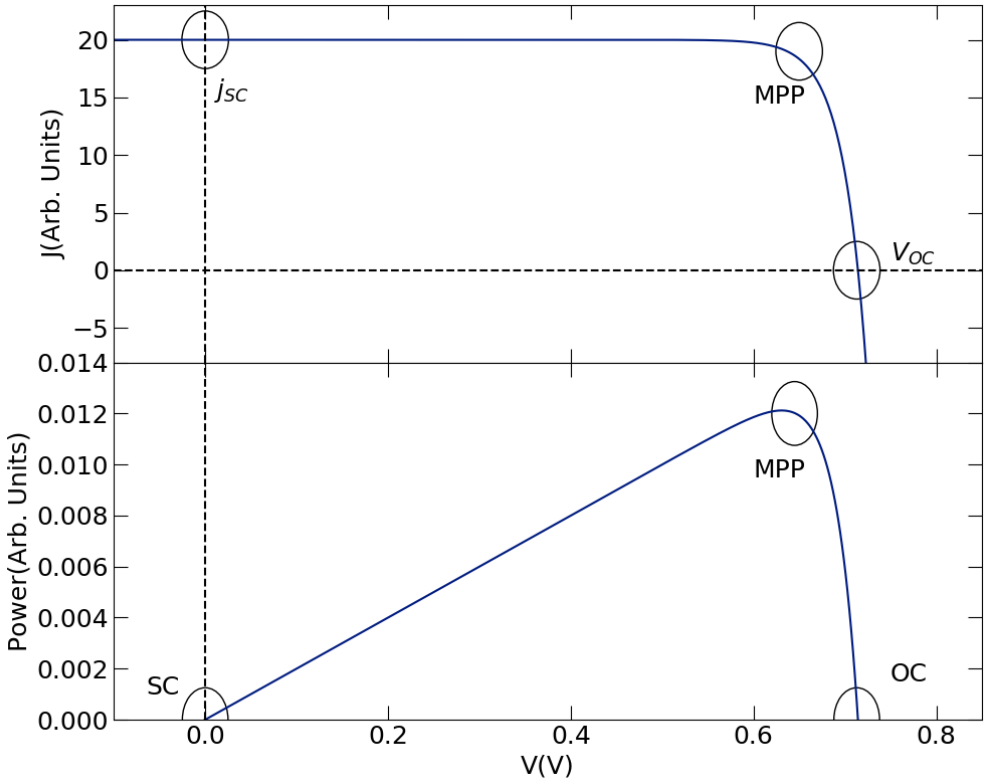

Figure 1.1: (a) current-voltage characteristic of a diode solar cell, the dotted lines correspond to $j = 0$ and $V = 0$. The points corresponding to short circuit (SC), open circuit (OC) and maximum power (MPP) are highlighted. Panel (b) power output of a diode solar cell. The relevant points corresponding to the ones in panel (a) are reported.

defined as the short-circuit photocurrent: $j_{SC} = j_{ph}$. This allows j_{ph} to be defined in terms of an operating device: it is equivalent to the current at short circuit (SC). The second point is the open-circuit point, which corresponds to the condition $j = 0$, and therefore the recombination current and the photogeneration currents are balanced. The voltage at which this happens is called the open-circuit (OC) voltage, and it is:

$$V_{OC} = \frac{mk_BT}{e} ln\left(\frac{j_{ph}}{j_0} + 1\right). \tag{1.3}$$

It should be noted that the voltage resulting from illumination corresponds to the separation of the electron and holes Fermi energies, therefore in open circuit configuration:

$$V_{OC} = \frac{\mu_e - \mu_h}{e} = \frac{\Delta\mu}{e}, \tag{1.4}$$

where μ_e and μ_h are the electron and hole quasi-Fermi levels. Finally, between these two points, lies the point where the output power of a device is maximum, this is called the maximum power point (MPP). It is obvious that the MPP is the ideal operating condition for a solar cell. The maximum power generated by the device is then: $P_m = j_{MP}V_{MP}$, and so it is possible to define an operational definition of efficiency, as a power conversion efficiency:

$$\eta = \frac{j_{MP}V_{MP}}{\Phi_T}, \tag{1.5}$$

where Φ_T is the total incident power from the source (the sun), usually defined as the standard terrestrial spectrum AM1.5G, corresponding to an integrated power of $1\,\mathrm{kW/m^2}$.

The shape of the jV characteristic defines at which operational point the device works best, however differences in the shape of the characteristic may lead to a higher/lower optimal voltage. It is possible to define a figure of merit that quantifies how the shape of the j-V characteristic performs, this is called the fill factor:

$$FF = \frac{j_{MP}V_{MP}}{j_{SC}V_{OC}}, \tag{1.6}$$

which allows the convenient reformulations: $P_m = J_{SC}FFV_{OC}$, and $\eta = \frac{j_{SC}FFV_{OC}}{\Phi_T}$.

Shockley and Queisser [7] in 1961 provided a simple model to describe the maximum efficiency of a solar cell, given a certain band gap, assuming an incident power corresponding to a 6000 K black body. It can be shown that the maximum efficiency occurs for a band gap of around 1 eV, and corresponds, within the approximations of the model, to a $\sim 30\%$ efficiency. The reasons behind this value are now discussed.

A model of the major causes of loss in a solar cell is reported in Figure 1.2 as a function of the band gap. The blue-shaded area consists of the maximum theoretical efficiency (also called the Schockley-Queisser limit), while red, green, and violet correspond to three different loss mechanisms that are now going to be detailed. The oscillations in the plot arise from the fact that the AM1.5G spectrum was used as a source, rather than a black body spectrum. The main causes of energy loss are:

1. The trade-off given by the MPP (fill factor)
2. Transparency below the band gap

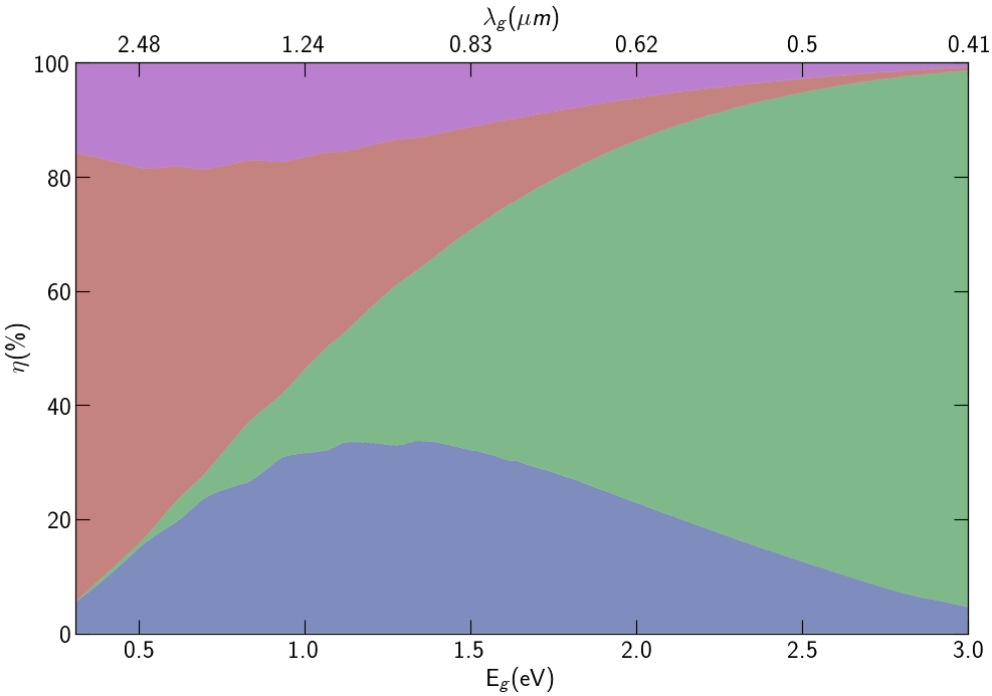

Figure 1.2: Plot representing the efficiency losses as a function of the band gap: blue is the power fraction that can be theoretically converted (the Shockley-Queisser limit), green is the efficiency lost because photons below the band gap are not absorbed, red is the efficiency lost because of carriers losing energy as heat and violet is the efficiency lost because of the trade-off between current and voltage in the j-V characteristic. The wiggles in the spectra are caused by the absorption in the AM1.5G spectrum used as a source.
Figure made by modification of the software SolarCellEfficiencyLimits on GitHub, distributed under the MIT License[6]

3. Relaxation of hot carriers

4. Other minor causes

Cause 1 has already been discussed: it consists in the unavoidable trade-off between the high voltage and the high recombination current described by the FF (violet in Figure 1.2). Issue 2 consists in the fraction of photons that are lost because they have an energy lower than the band gap (green in Figure). Loss 3 is the energy that is lost because an electron-hole pair generated by a photon with an energy higher than the band gap loses this excess energy into heat (red). Finally in item 4 are contained other minor loss mechanisms, that might arise from more realistic models of a solar cell, such as the conversion of thermal energy or the mismatch of absorption and emission angles (see for example Hirst and Ekins-Daukes [8]). A

simple solution to 2 is to use lower-bandgap material, and in fact the maximum power is attained at a relatively small band gap of 1 eV. However, using materials with smaller bandgaps dramatically increases mechanism 3, creating a trade-off at around 1eV.

As a well-known issue, multiple possible solutions to beat the Shockley-Queisser limit have been proposed over the years, : light concentration, photon upconversion [9], multiple exciton generation [10], multi-junction solar cells and hot carrier extraction, to name a few. Of these, the most mature technology is certainly the one based on multi-junction solar cells (also known as tandem cells), which consist in the stacking of materials with different band gaps in order to use efficiently all the parts of the solar spectrum. However, the architecture of such devices is quite complex (and expensive) which represents a significant drawback. A recent review of the most common approaches to improve device efficiency beyond the SQ limit is reported in Tanabe [11].

A less travelled, but nonetheless fascinating, road consists in finding a mechanism capable of extracting hot carriers before they lose their energy. A device based on hot carriers rather than cold ones (*i.e.* a standard solar cell) could theoretically reach an efficiency of 65% under 1 sun illumination [12], and 85% under concentrated sunlight [12–14]. How such devices work and the possible advantages and drawbacks are going to be extensively discussed in section 1.3.1.

1.1.2 Material properties

The previous section explained important external parameters fundamental to the characterisation of a photovoltaic (PV) device. In this section, however, the intention is to take a step back to look at the internal quantities and parameters of the light absorbing layer that are useful to characterise a material's properties from a PV point of view.

While the external parameters are extremely useful and provide a direct link to the real-world performance of a solar cell candidate, there are some sensible drawbacks in relying only on device operation: to test a solar cell candidate in a device, it is necessary to fabricate a device in the first place, which could be not straightforward, as there might be the need to tailor the specific device architecture for that specific candidate (for example, using different charge transport layers, or by using different geometries). In second instance all the quantities measured in a device are, for the most part, dependent on the specific device, as contingent characteristics such as the sample quality and morphology or the quality of the contacts can influence the measurements. Moreover a material can be good in certain

architectures, but not in others, therefore exponentially complicating the analysis. Therefore it is obvious that having a way to assess the candidate material's possible performances before making a device is extremely useful. The performance of a generic semiconductor as a light converter depends on different internal parameters that are now going to be discussed.

First it is useful to define the *external* quantum efficiency, for a solar cell operating as a light-emitting diode (LED), as the ratio of the recombination current (leading to radiative recombination and emission of photons) and the total recombination current as [15, 16]:

$$\eta_e = \frac{j_{em}}{j_{rec}}. \tag{1.7}$$

This definition, seemingly arbitrary, has its roots in so called reciprocity relation: a PV device and an LED work by using effectively the same physical process, a photon creating an e-h pair in the first case, and an electron-hole pair annihilating and emitting a photon in the second. As such the properties that characterize both are linked and, in general, a good solar cell material is also a good LED material [16].

The definition in Equation 1.7, however, helps to quantify the effect that non-radiative processes have on the solar cell parameters, specifically on V_{OC}:

$$V_{OC}^{rad} - V_{OC} = -\frac{k_B T}{e} \ln(\eta_e), \tag{1.8}$$

where V_{OC}^{rad} is the OC voltage in the limit that all the recombination is radiative. It follows the definition (Equation 1.7) that $\eta_e \leq 1$ and therefore $V_{OC} \leq V_{OC}^{rad}$, with the equalities occurring only in an ideal device. As a rule of thumb, each order of magnitude change in η_e yields a change in V_{OC} of $\frac{k_B T}{e} ln(10)$ $\simeq$60mV. As V_{OC} is one of the most important device parameters, it follows that so is η_e.

It is also possible to define an *internal* quantum efficiency as the ratio of recombination rates:

$$\eta_i = \frac{R_R}{R_T} = \frac{R_R}{R_R + R_{NR}}, \tag{1.9}$$

where R_R is the radiative recombination rate, and R_{NR} is the nonradiative recombination rate. R_T is the total recombination rate. The most common example of a radiative recombination process is a bimolecular recombination process (electron and hole recombining), which can be expressed as:

$$R = k_R np, \tag{1.10}$$

where n and p are the electron and hole densities and k_R is the radiative recombination coefficient. The nonradiative rate R_{NR} can also be expressed as a function of the carrier density, assuming a Shockley-Read-Hall (SRH) trap-assisted recombination model[17, 18]:

$$R_{NR} = R_{SRH} = \frac{n}{\tau_{SRH}}, \tag{1.11}$$

where τ_{SRH} is the average SRH recombination time. All these processes will affect the overall dynamics of carrier recombination. It is in fact possible to generalize the carrier density charge dependence (assuming $n \simeq p$) as:

$$\frac{dn}{dt} = G - k_1 n - k_2 n^2 - k_3 n^3 = G - n R_T(n), \tag{1.12}$$

where k_1 is the monomolecular recombination coefficient, that can be identified with Equation 1.11, k_2 is the bimolecular recombination coefficient (identifiable with Equation 1.10), and k_3 is the Auger recombination coefficient, corresponding to an Auger process (an electron and a hole recombining by giving energy to a third electron), which won't be discussed further here as it is not necessary to understand the key concepts. $R_T(n)$ is the total recombination rate and G is the carrier generation rate.

It is of great importance to properly define the recombination rates and coefficients, as most time-resolved spectroscopy techniques (such as time-resolved photoluminescence, transient absorption or optical pump terahertz probe spectroscopy) are capable of tracking the recombination dynamic, so to effectively measure the total recombination rate, R_T. Moreover, appropriate fluence-dependent measurements allow a global fit using Equation 1.12, allow the k_i coefficients to be measured. This is, of course, of great importance in the characterization of PV materials.

Once these basic quantities and the basic definitions have been introduced, it is possible to extend the discussion on how to identify a potential candidate for a PV technology. There are three important parameters: the absorption coefficient α, the charge-carrier lifetime τ and the mobility μ. A peculiar case of interest is the case of high absorbing materials, which is the case of most MHP. A highly absorbing material requires a lower thickness to completely absorb the incident light. In general the short-circuit current can be expressed as:

$$j_{SC} = \int_0^\infty \alpha(E)\Phi_T(E)dE, \tag{1.13}$$

where $\alpha(E)$ is the absorption coefficient, and it is possible to simulate what the SC current and the OC voltage do as a function of thickness. Such simulations are

reported in Kirchartz *et al.* [15] and show that while j_{SC} is monotonously increasing with thickness, V_{OC} is generally monotonously decreasing. Therefore there exist an optimal thickness that yields the best efficiency. For materials with strong absorption, such as MHPs, thicknesses below 1μm provide already optimal efficiencies for realistic values of the lifetime. This discussion allows the determination of a critical mobility, *i.e.* the minimum mobility required to achieve efficient collection.

Assuming a carrier diffusion model as a lower limit of the collection efficiency, then it is possible to express the efficient extraction when the diffusion length is at least twice the optimal thickness. Recalling the Einstein relation:

$$D = \frac{\mu k_B T}{e}, \tag{1.14}$$

where D is the diffusion constant and μ the mobility, then the diffusion length can be estimated as:

$$l_D = \sqrt{D\tau} \tag{1.15}$$

with τ the lifetime. The simulations reported in Kirchartz *et al.* [15] show that for a strongly absorbing material, with a relatively long lifetime (100 ns-1 μs), the critical mobility lies in the range $0.1 - 10\text{cm}^2/\text{Vs}$. As such, a relatively low mobility (as for MHP, which have mobilities rarely above $100\text{m}^2/\text{Vs}$, which is an order of magnitude lower than Si, Ge or GaAs) is not detrimental at all to solar cell performance, given a long enough lifetime. This could explain why the low mobilities of MHP (even lower than what would be expected by their effective mass, as it will be explained shortly) don't seem to affect their efficiency as PV materials.

The last piece left is the link between the lifetime and the recombination coefficients. As presented in Equation 1.12 the recombination dynamic of carriers can be expressed, neglecting generation, as: $\frac{dn}{dt} = -nR(n)$, and it is possible to identify τ as $\tau = \frac{1}{R(n)}$. Recalling that $R(n) = k_1 + k_2 n + k_3 n^2 = R_1 + R_2 + R_3$, it follows that the lifetime can be expressed as:

$$\frac{1}{\tau} = \frac{1}{\tau_1} + \frac{1}{\tau_2} + \frac{1}{\tau_3} \tag{1.16}$$

where $\tau_i = \frac{1}{R_i}$.

To conclude, there are three fundamental properties that identify a good PV candidate: α, τ and μ, of which two can be measured with time-resolved spectroscopy techniques such as optical pump terahertz probe spectroscopy (OPTP), which is capable to estimate the mobility and the lifetime, as will be shown in the following chapter. The performance of MHPs with regard to these properties is now

discussed.

1.2 Metal halide perovskites

In recent years the interest in solar cells based on metal halide perovskites (MHPs) has undergone an outstanding growth: from a few seminal papers in 2009 and 2012 [19, 20] it has reached an impressive thousands of papers per year on the topic. There are a number of reasons for this interest: one of them is evident in Figure 1.4. This is a plot of all the most relevant technologies in photovoltaics; the perovskite-based materials have reached an efficiency above 25%, comparable with silicon, the benchmark for any photovoltaic technology that has any hope to be considered by industry, in an extremely short amount of time. These levels of efficiency have been reached thanks to a combination of excellent qualities, such as strong absorption in the visible[21, 22] and low recombination rates at moderate defect densities[23–26].

MHPs are also characterised by a range of unconventional characteristics as: low optical phonon energies[27–29], moderate mobilities despite low effective mass[26, 30] and a high resistance to defects that gives rise to high-quality materials at low preparation temperatures[26, 31–34].

All of these features, make MHP a rather peculiar class of materials, whose physics seem to be in contrast with decades of research on semiconductor physics[26]. This makes them already interesting from a physical point of view, as understanding why this is the case could help us increase our knowledge of solid state physics even further and maybe design other materials with similar properties. From an application point of view, some of the performances reached by perovskite solar cells (PSC) are so outstanding that there is already a debate on how to actually implement them in real-world devices.

Such a great amount of work has been put into studying MHP that to attempt to provide a comprehensive overview of all the field's ramifications is a daunting task. Moreover the field is so fast-paced that good reviews/comments written just few years ago[35, 36] seem now outdated. Hence, in the following, the aim will be to provide a very broad overview of some of the most important research directions in the field, with a focus on the topics that seem more relevant for this work's research, without the claim to be exhaustive.

1.2.1 What are metal halide perovskites?

The perovskite structure has the formula ABX_3, where X is an anion and A and B are cations, where A is larger than B. MHP consist of a class of materials with

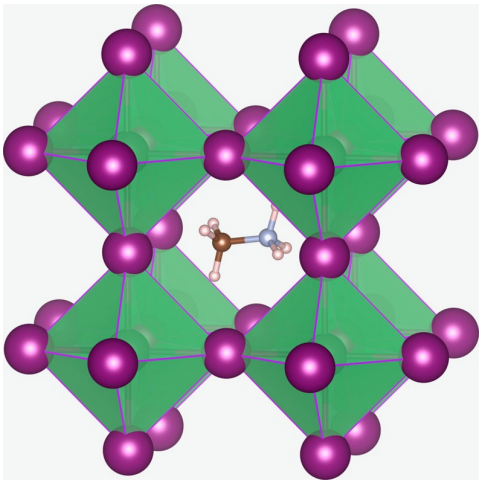

Figure 1.3: Schematic representation of the perovskite structure: at the centre lies the A-site cation, inside the octahedra lies B-site metal and purple spheres are the X-site halides. Image taken from Eames *et al.* [37] and used in accordance with the Creative Commons Attribution license (https://creativecommons.org/licenses/by/4.0/).

perovskite structure, where the B site is a metal (Pb or Sn), the X site is an halogen (generally iodine, although Br and Cl have been used, usually in mixed composition) and the A site can be an organic molecule, such as methylammonium ($CH_3NH_3^+$, MA) or Formamidinium ($NH_2CHNH_2^+$, FA), or an inorganic element such as Cs or Rb or a mixture of these. A unit cell of the perovskite structure is represented in Figure 1.3. The structural phase and stability of perovskites can be assessed with a tolerance factor t and an octahedral factor μ [36]. Assuming a solid-sphere model, these two parameters can be expressed as $t = \frac{R_A+R_X}{\sqrt{2}(R_B+R_X)}$, and $\mu = {}^{R_B}/_{R_X}$, where R_A, R_B, and R_X are the ionic radii of the corresponding ions. For halide perovskites (X=F, Cl, Br, I) generally $0.81 < t < 1.11$ and $0.44 < \mu < 0.90$ [38]; values of t within 0.89-1.0 are likely to give rise to a cubic structure, with lower values corresponding to tetragonal or orthorhombic structure. However multiple temperature-induced phase transitions between the different structures are known to happen.

The first time lead and tin halides were synthesized was as early as 1893 [40], although the first evidence that $CsPbI_3$ had a perovskite structure occurred only in 1958 [41]. To have the first organic-inorganic hybrid perovskite one had to wait till 1978, where for the first time Cs was replaced by MA [42, 43]. However these materials remained mostly unstudied until 2009 when $MAPI_3$ was introduced by Kojima *et al.* [19] as a sensitizer for dye-sensitized solar cells. In the course of a

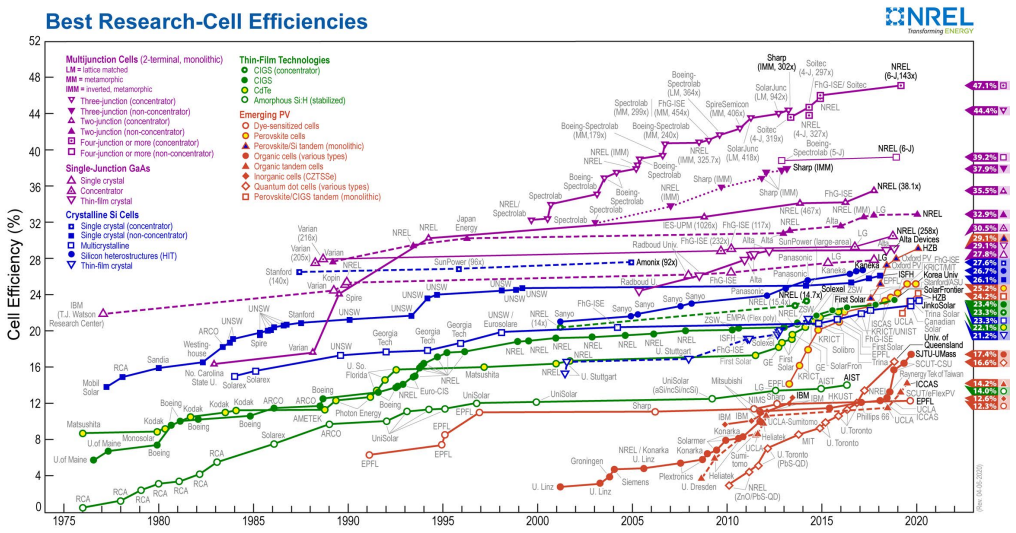

Figure 1.4: Efficiency chart of the most common photovoltaic technologies. Perovskite photovoltaics correspond to the yellow-filled orange circles, Si-based cells are in blue. This plot is courtesy of the National Renewable Energy Laboratory, Golden, CO [39].

few years, in 2012, Lee *et al.* [20] discovered that that $MAPI_3$ had good transport properties. Since then MHP have undergone an impressive growth, as highlighted by the chart in Figure 1.4, showing now efficiencies exceeding 20% [39, 44, 45], and the efficiency will only increase with the better implementation of silicon-perovskite and perovskite-perovskite tandem solar cells[46], and this in only a decade of active research.

As already explained at the beginning, MHP have, in the span of few years, surged to a prominent position in the field of photovoltaics thanks to their outstanding properties, which will now be reviewed.

The first clear strength of MHP is the high absorption coefficient and sharp absorption edge [22] both important properties for an absorber material in allowing a thin film geometry. The sharp absorption edge is related to the direct bandgap for both organic-inorganic [47] and fully inorganic [48] MHP. The absorption, moreover, shows low values of Urbach energy at room temperature [22]. The band gaps of $MAPbI_3$ and $FAPbI_3$ lie around 1.5 eV [49] which is relatively close to the optimal value of 1 eV, however tin-based perovskites show much smaller bandgaps, around 1.3-1.4 eV [48], which is very close to the optimal value for power conversion. The bandgap however is widely tunable by changing the composition, for example by changing the size of the cation [50], or by alloying the X-site [49], while still maintaining a sharp absorption edge. More complex compositions are also employed,

for example mixed lead-tin perovskites have raised interest thanks to their very low band gap (1.2 eV) very close to the optimum value [51, 52].

The most outstanding characteristic of MHP, however, is probably the (surprisingly) long recombination time [53]. The recombination time (or lifetime), as discussed above, is one of the most important parameters in predicting the performance of a solar cell material, the recombination times of MHP are very long, often exceeding 100s of ns [26, 53], and sometimes approaching the μs range [24, 54]. The surprising part is that these recombination times are much longer than expected [23, 25]. The low temperature at which these materials are processed, should give rise to elevated defect densities, however MHP seem quite resistant to the presence of defects [31–34]. This has produced a substantial amount of work on the study of defects in MHP and the reason behind this peculiar behaviour is not understood yet.

1.2.2 Polarons

Another element of surprise is certainly the low mobility observed in MHP. The mobility can be expressed as $\mu = \frac{e\tau}{m^*}$, where m^* is the effective mass, τ is the momentum scattering time and e is the elementary charge. The value of μ can be low if the effective mass is high, or if τ is small. Given the calculated effective mass (around 0.1-0.2m_e[30, 47], with m_e the free electron mass), and assuming a scattering rate similar to that of classic inorganic semiconductors as GaAs the mobility of MHP should be more or less comparable to the mobility of inorganic semiconductors. However, the mobilities are much more limited, ranging in the 1-100 cm^2/Vs, depending on material quality, composition and technique, but in most cases, in compositions routinely used for solar cells, occurring in the 20-30 cm^2/Vs range[30]. It has to be said that there had been some inconsistency in the reported mobility values in MHP [30], however even measurements performed on single crystals or via techniques less influenced by the morphology (*e.g,* optical pump terahertz probe spectroscopy, or microwave conductivity measurements) have not shown substantially higher mobilities. This has sparked a debate on the origin of this limited mobility and its consequences on the PV efficiency. However, as explained in section 1.2, as long as the mobility reaches a critical value, the carrier extraction efficiency is not limited by it; given the benign defect chemistry and consequent very long recombination times found in MHP the diffusion length is long enough to allow efficient carrier extraction even at the very low mobility observed in virtually all thin-film solar cell geometries, explaining why the mobility does not seem to limit the device efficiency.

The estimated values for the effective mass given above imply (for $\mu < 100\text{cm}^2/\text{Vs}$) a scattering time of the order of 10 fs, much lower than GaAs, or other similar semiconductors. Such a low scattering time can be attributed to a strong electron-phonon coupling. The dominant electron-phonon scattering effect at room temperature is the electron-LO (longitudinal optical) phonon scattering mediated by the Fröhlich interaction [55]. Ab initio calculations have been able to reproduce the right order of magnitude of the mobility and its correct temperature dependence assuming that Fröhlich scattering dominates[30, 56, 57]. The interesting consequence is the formation of a polaron, and the need to take into account the polaronic nature of carriers in MHP[56], as it is now discussed.

Placing an electron in a ionic lattice polarizes the surrounding, giving rise to a polarization field that travels with the particle. This effect can be described as a quasiparticle with different properties than a band electron: a polaron. This description was established by the works of Fröhlich [58] and Feynman [59], and the important consequences, for this discussion, are an increase in the effective mass and a reduction of the mobility. The electron-phonon coupling constant, that characterizes the strength of the electron-phonon interaction, is:

$$\alpha = \frac{e^2}{4\pi\varepsilon_0\hbar}\sqrt{\frac{m^*}{2\hbar\omega_{LO}}}\left(\frac{1}{\varepsilon_\infty} - \frac{1}{\varepsilon_s}\right), \tag{1.17}$$

where e is the elementary charge, ε_0 is the vacuum permittivity, $\hbar$ is the reduced Planck constant, m^* is the effective mass, ω_{LO} is the angular frequency of the lowest LO phonon mode, ε_∞ is the high-frequency dielectric constant and ε_s is the low frequency dielectric constant. Given the estimated value of α in MHP (around 2), and the temperature dependence of the mobility (suggesting band-like transport) it has been deduced that the interaction gives rise to large polarons (*i.e.* a polaron radius that is substantially bigger than the unit cell size). From these premises theoretical calculations have shown that most of the reduction in mobility could be accounted by such a model [56].

At this point, given their importance in both the transport properties and HC potential of MHP it is important to discuss phonons. Leguy *et al.* [55] assigned observed Raman and THz spectroscopy peaks to phonon modes calculated through density functional theory (DFT). Organic-inorganic MHP, given their complexity have 36 possible modes for the cubic phase, which increase to 144 for the less symmetric tetragonal and orthorhombic configurations. Leguy *et al.* [55] identified two frequency ranges: the low frequency modes (less than $\sim$200 cm^{-1}, around 6 THz) correspond to cage-dominated optical modes, while the high frequency modes cor-

respond to the cation (MA) modes. In particular, it is relevant for this work that the modes around 1 THz are optical and assigned to the Pb-X cage distortion. This is important because alloying the B and X sites would mostly affect these low frequency modes and would shift the LO phonon modes that are responsible for the Fröhlich interaction, therefore affecting the polaronic nature of the transport (effective mass, mobility) and the hot carrier cooling process. Finally in the same work they suggested that optical phonon modes are likely to dominate at room temperature, therefore justifying the conclusions from the mobility measurements [30].

1.2.3 Open issues

However, despite the outstanding performances and the impressive effort the research community has put in, there are still some significant open issues that stand in the way of the long-term goal of a real-world application. The most serious of these are long-term stability and toxicity of the MHP. The former has been tackled directly since the early days of perovskite research, and concerns three practical sources of degradation: moisture, oxygen and light exposure, among many others [60, 61]. The research has focused mainly in two directions: improvement of the device structure in order to reduce the causes of degradation and change the composition (for example the addition of bromine) and the processing techniques in order to improve the chemical stability in the long run[60]. Despite the good results so far more work is needed to address these problems [61].

The second issue is more practical as most of the best performing materials to date contain some quantity of lead, which is notoriously toxic. Studies have tried to assess the possible biological impact of a lead-based photovoltaic technology, which is in general thought to be a significant issue[62]. The most followed path to solve this problem is by substituting the metal (lead) with the metal just above on the periodic table: tin, which is thought to be less toxic. Since this idea was proposed, the research has focused even more on the study of organic and inorganic tin perovskites, as well as alloying lead and tin in the hope of finding improved properties. Although it has to be said that Sn-based perovskites are also susceptible to the degradation mechanisms described in the previous paragraph. This thesis follows this research path by studying the influence of Sn on hot carrier cooling (HCC), first by studying a pure Sn-based perovskite and secondly by studying mixed lead-tin compounds with a variable Pb/Sn ratio.

1.2.4 Beyond perovskite solar cells

Solar cells are the primary field where MHP have been implemented but different applications have been investigated, such as LEDs (a good solar cell material tends to be a good LED material)[63], x-ray detectors[64, 65], photodetectors[66, 67] and lasers [68]. A good description of MHP properties as photodetectors and x-ray detectors is reported in Dong *et al.* [66], Wei and Huang [65] and Jena *et al.* [45].

Finally it is worth mentioning the more novel structures, especially lower-dimensional ones, as 2D perovskites and quasi-2D perovskites. A 2D perovskite is a structure where monolayers of the MHP in question are alternated with a bulky organic cation (an additional, larger cation than the usual MA or FA). By altering the precursor composition it is also possible to form structures dominated by two perovskite layers alternated by the organic cations, three perovskite layers, four and so on, up to infinity where the normal 3D structure is recovered. Such structures are called quasi-2D perovskites, as they are characterized by intermediate properties between 2D and 3D perovskites. A recent review of 2D and quasi-2D perovskite is Zhang *et al.* [63]. 2D perovskites do not offer better photovoltaic performances, due to the larger band gap caused by the confinement, but show greater stability than the 3D counterparts, so they have been applied in 2D-3D compositions to increase the stability of the overall cell. A strong interest has risen towards colloidal nanostructures, such as MHP nanocrystals, thanks to their great PL properties and wide tunability of optical properties, see for example Fu [69]. Finally, the search for lead-free alternatives has pushed the research to investigate structures where the Pb is substituted by Sb or Bi or by noble metals as gold and silver, forming more complex structures named double-perovskites for their doubled unit cell size [70]. Note that these categories can mix forming even more complex structures, such as double perovskite nanocrystals [71].

1.3 Hot carrier cooling in perovskite solar cells: models and experiments

As explained in section 1.1, the relaxation of hot carriers is one of the main limiting factors in solar cell efficiency. As such, numerous ideas have been proposed to overcome these limitations. In this section the discussion focuses on one of these ideas that the recent developments in the field of MHP have brought back into consideration: a hot carrier solar cell (HCSC). A HCSC is based on the simple idea of extracting the carriers right after photoexcitation, before they completely relax

and lose their energy. The concept was first proposed in 1982 by Ross and Nozik [12], and in the same work it was proved that an increase in the temperature of the extracted carriers (from 300 K to 1000 K) could lead to a maximum efficiency of around 60%, with a maximum theoretical efficiency of 65% under 1 sun illumination, which could reach values close to 86% for concentrated sunlight [13]. Now the concept of a HCSC will be briefly introduced, and the remarkable performances of MHP in this context are going to be presented.

1.3.1 Hot carrier solar cells

Since the concept of HCSC has found a resurgence with the novel interest sparked by MHP, there are a number of recent reviews that deal with the concept, although from a MHP point of view. Kahmann and Loi [14] provided a good background to the HCSC concept, to the characteristics of a suitable absorber material and to the extraction mechanism. The same review gave a broader overview to other possible HCSC candidates, such as the III-Vs and quantum dots (QD). More perovskite-focused reviews are going to be discussed later on. Other reviews that approach the issue (mostly on III-V nanostructures or wurzite semiconductors) are: Conibeer [72], Konig *et al.* [73], Conibeer *et al.* [74].

In the original work Ross and Nozik [12], estimated the maximum theoretical efficiency by modelling a solar cell as a ideal black-body light converter, much as in Shockley and Queisser [7]. Under such assumptions the problem consists in maximizing the power output of such a device:

$$P = \Delta\mu_{use} I_{use}, \tag{1.18}$$

where $\Delta\mu_{use}$ is the potential difference of hot carriers at a temperature T_H, and I_{use} is the number of photons absorbed less the number of photons emitted. A device so modelled can have theoretical efficiencies as high as 65% (under normal sunlight illumination) [12]. More recently, more realistic models have been proposed [13, 75–78], however the efficiencies estimated are still around 50%[77].

One of the first basic HCSC designs is reported in Würfel [79], it consists of of an architecture similar to a conventional solar cell, with an absorbing material sandwiched between two extraction layers and external electrodes. For the sake of this discussion this model is more than appropriate to highlight the key facts. The extracting layers need to have very specific characteristics: they need to have a very narrow energy-dependent extraction range: they should be able to extract all electron and holes at energies E_e, E_h in a narrow range of energy $\delta E < k_B T_L$,

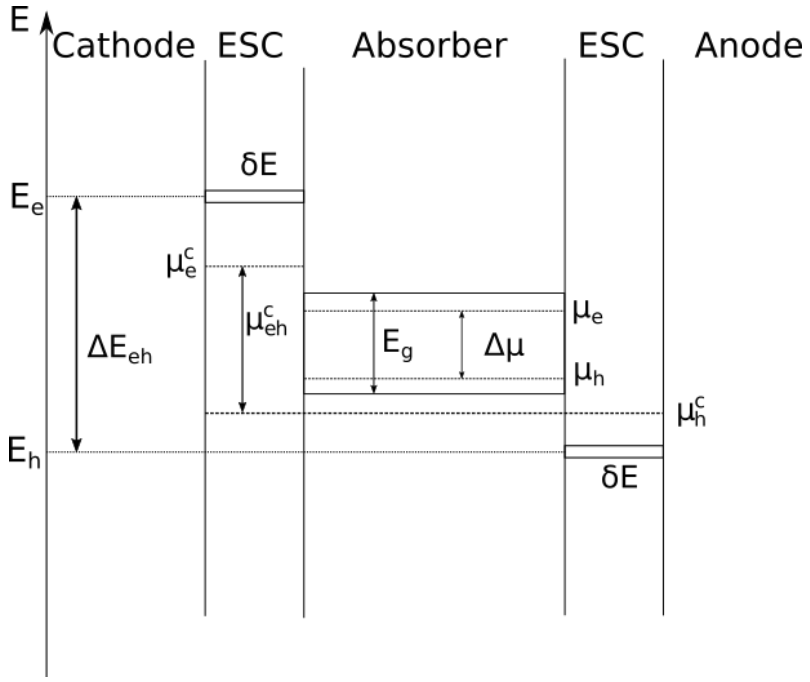

Figure 1.5: Schematic representation of a possible hot carrier solar cell similar to Würfel *et al.* [13] and Kahmann and Loi [14]. E_g is the band gap, $\Delta\mu = \mu_e - \mu_h$ is the equilibrium chemical potential separation, δE is the width of the ESC, ΔE_{eh} is the energy separation of the ESC, $\mu^c_{eh} = \mu^c_e - \mu^c_h$ is the separation of the quasi Fermi energies in the contacts.

with T_L the lattice temperature. This is necessary to avoid interaction with the electrodes and injection of cold carriers from the contacts or the electrodes. Such extractors are termed energy selective contacts (ESC). The identification, realization and assessment of appropriate ESC is an important and interesting topic, however, in this work, the focus is directed at the absorber material, so for the sake of simplicity it won't be discussed, the interested reader can consult the relevant literature [73, 80–83].

A device such as the one just described can be shown, assuming the electron temperature equal to the hole temperature $T_e = T_h = T_c$, with T_c the carrier temperature, to have a OC voltage given by [78]:

$$V_{OC} = \frac{\mu^c_{eh}}{e} = \frac{\Delta E_{eh}}{e}\left(1 - \frac{T_L}{T_c}\right) + \frac{\Delta\mu}{e}\frac{T_L}{T_c}, \tag{1.19}$$

where ΔE_{eh} is the separation of the ESC, μ^c_{eh} is the difference between the quasi-chemical potentials (electron and holes) of the contacts and $\Delta\mu$ is the Separation of quasi-Fermi level at steady-state. Interestingly the V_{OC} is not limited by the band

gap energy as in Equation 1.4.

From the discussion in the literature [14, 76, 77, 83] two critical issues have been established: the carrier relaxation time in the absorber and the width δE of the ESC that controls the carrier extraction. The latter, as said, won't be discussed further in this thesis, the former, however, is quite possibly *the* parameter that characterizes the absorbing material. Numerous reports [75–77] identified the energy relaxation time τ_r as the most impacting the overall efficiency. To avoid confusion a few definitions are necessary: the names "energy relaxation" and "carrier cooling" refer to the process where carriers have a thermal distribution, characterized by a temperature $T_c > T_L$, and progressively cool down and lose energy until $T_c \sim T_L$. The name "thermalization", instead, is referred to the process of carrier being injected by photons with a non-thermal distribution, and progressively, mainly thanks to carrier-carrier scattering, redistribute the energy among themselves and reach a thermal (Maxwell-Boltzmann) distribution. Both processes are characterized by typical times: τ_r for the energy relaxation time, and τ_t for the thermalization; both times have an influence on the efficiency of a HCSC. τ_t also describes the timescale for the carrier distribution to re-equilibrate after part of them have been extracted by the ESC.

As said, τ_r is possibly the most important parameter, and it has been found that it needs to be on the timescale of radiative recombination; Takeda *et al.* [76] found 1 ns to be the threshold value at which an HCSC could break the SQ limit efficiency. However, this is not the only constraint, as, in the same work, it has been found that the thermalization time τ_t needs to be $\sim \tau_r/1000$, for the extraction process to be efficient, as the levels depleted by the ESC need to be quickly repopulated, to avoid energy loss. Finally, the last parameter is the carrier retention time (τ_{ret}), the time that carriers spend in the absorber before extraction. Takeda *et al.* [75] found that for optimal performance τ_{ret} has to be around 10 times smaller than τ_r.

Finally, to ensure a slow cooling time, it is important to understand the mechanisms that contribute to the energy loss, which consist of the interaction of the hot carriers with optical phonons, the interaction of optical phonons with acoustic phonons and, in general, of the phonon bandstructure[73]. A soon as carriers have been injected by photons, in fact, carriers thermalize via carrier-carrier scattering, until they reach a thermal distribution (Maxwell-Boltzmann) and a temperature can be defined. These carriers are then at a temperature T_c higher than the lattice temperature T_L. Said hot carriers will then cool down by interacting with LO phonons; if the temperature is high enough and the carrier concentration is high enough, then the phonon population cannot disperse the energy quickly enough, as

the LO phonons lose energy by interacting with acoustic phonons, which is generally less efficient. The phonon temperature will then reach the carrier temperature and the energy loss is then limited, and theretofore determined, by phonon decay. This mechanism is called "hot phonon bottleneck" (HPB) and it is considered to be of paramount importance, as most research has focused in reducing the efficiency of the phonon decay[73, 81, 82].

From the previous paragraph it follows that the carrier cooling is as slow as the phonon decay, and that a way to improve the HCC time is by reducing the efficiency of the phonon decay [73]. A thorough description of the various phonon decay pathways is given in Chapter 3, where all the process is better described as it is the theoretical basis of the model there described. For the discussion in this Chapter, it is important to note that one of the way to suppress one of the decay channels (the Klemens channel) is by increasing the separation between the optical phonon branches and the acoustic phonon branches, realizing what is called a phonon gap (in analogy with the electronic band gap). A way to achieve this phonon gap is usually by coupling elements with different masses. For a good description of the parameters that an absorber needs to have to achieve a slower energy loss the reader should refer to Conibeer *et al.* [81, 82].

Candidates that have been considered for a practical realization of a HCSC absorber, thanks to their large phononic band gap are: InN, GaN, BiN, where the light nitrogen atom helps the formation of a large gap and SnO, Bi_2O_3, InP and AlSb[81, 82]. There is also research on the Bi-based compounds [73], II-VI nitrides [74] and III-V with large anion mass [74]. Although most of these materials show conflicting properties as a low band gap, suitable absorption, carrier mobility *etc.* Moreover the times observed seem lower than required for an efficient HCSC. Most research has then focused on nanostructures: a different type of phonon bottleneck is thought to happen in quantum dots (QD), and a suitable phononic bandstructure could be engineered with quantum well superlattice structures. However observations in these structures are caused by more complex effects.

1.3.2 Hot carrier cooling in perovskite halide semiconductors

Among their other outstanding properties (already extensively discussed), it was recently observed that the hot carrier cooling of MHP was much longer than expected, taking, depending on the experimental conditions such as sample composition, excess carrier energy and carrier density, up to 100s of ps, close to the 1 ns threshold identified as the point where an HCSC start to become realistic and efficient. As such recently numerous review articles have been published tackling different sides

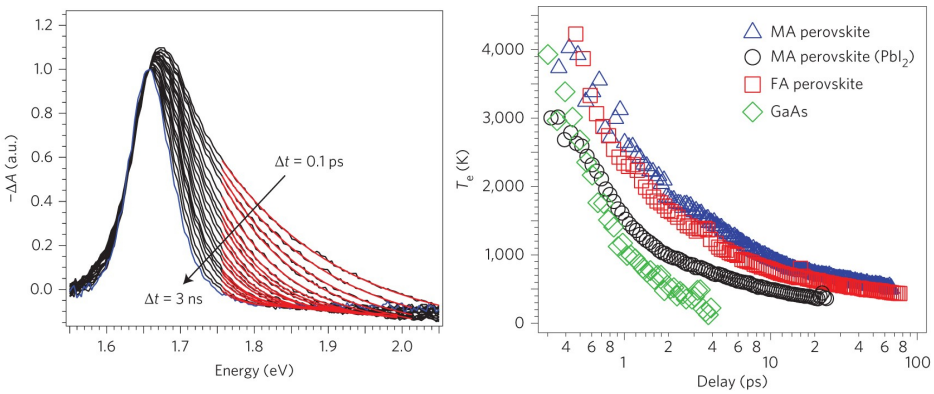

Figure 1.6: Left panel: example of a TA spectrum and the fit to extract the temperature. Right panel: temperature dynamics for $FAPbI_3$, $MAPbI_3$, $MAPbI_3$ with a large fraction of unreacted PbI_2 and GaAs. The enhancement of the HPB effect compared to GaAs is evident. Both images reprinted by permission from Springer Nature, Nature Photonics, Copyright 2016[86]

of the problem. Li *et al.* [84] and Kahmann and Loi [14] focused more on the possible photovoltaic applications (Kahmann and Loi [14] does also a good review of the operation of an HCSC and the state of the art of the field before MHP entered the scene). Joshi *et al.* [85], instead, focused more on the polaronic effects and how these might cause the slow cooling observed in MHP.

The first observation of a possible presence of hot carriers in MHP occurred in 2013 [87], where a delay in the rise of the ground state bleach in a transient absorption (TA) experiment was observed upon shorter wavelength excitation. This was attributed to a relaxation of hot holes from a second valence band to the top of the valence band in~ 0.4 ps. In the same work it was observed that that time was relatively long compared to most organic semiconductors [87], and suggested the possibility of extracting those hot holes. After few years, crucially, Price *et al.* [88] found that the broadening in TA spectra was connected to the temperature of the carrier population, fitted it to extract the carrier temperature using a Boltzmann factor (as in the left panel in Figure 1.6) and observed an enhancement in the carrier cooling time with the injected carrier density which they linked to a hot phonon bottleneck effect. Around the same time Flender *et al.* [89] observed a similar phenomenon in a MHP on a mesoporous TiO_2 scaffold, analysed the TA spectra in a similar way and, crucially, observed that the cooling dynamic was complex, divided into different stages and difficult to fit with a simple exponential, or two-exponentials fit. They attributed this behaviour to regimes dominated by scattering with optical or acoustic phonons, reaching similar conclusions to Price

et al. [88]. An example of the cooling curves extracted is reported in Figure 1.6. These findings were deemed even more intriguing as it was proved that these times were long enough to allow for long-range transport [90].

It should be noted, however, how the TA spectra are usually quite complex, especially for more complex systems as MHP: effects such as band gap renormalization (BGR), Moss-Burstein shift (MBS), refractive index change and excitonic effects all contribute to form the spectral shape observed. As such, very recently, it has been suggested that the usual procedure of fitting the high-energy tail of the ground state bleach (GSB) with a Boltzmann factor might lead to numerical errors [91]. However a confirmation of the validity of the approach was given by Yang *et al.* [86], in a thorough study of the various mechanisms that occur in TA spectra in MHP. They confirmed that the high-energy broadening of the GSB was indeed explainable by the presence of hot carriers. In the same work they compared the slowed-dynamic, again attributed to a hot-phonon bottleneck effect, to GaAs, observing a trigger of the effect at much lower carrier densities compared to the III-V semiconductor (see Figure 1.6). A possible reason was suggested as early as 2016 by Zhu *et al.* [92]: they proposed that the slowing of hot carrier cooling (this time observed with time-resolved photoluminescence) was caused by the screening caused by the formation of large polarons. This effect is not mutually exclusive with a more common HPB, but would occur at lower carrier density, therefore suggesting a possible competition of mechanisms strongly dependent of the carrier density (see also Niesner *et al.* [93] for another observation of slow cooling at low carrier density, this time with two-photon photoemission spectroscopy and Evans *et al.* [94] for a discussion on the competition between hot carrier effects and large polaron screening). As a matter of fact, more recently, it was suggested in a theoretical work that the this low carrier density was equivalent to the Mott density for polarons [95].

In general, this phenomenon seems to be observable with different techniques, such as TA [86, 88], Two-dimensional electron spectroscopy (2DES) [96, 97] photoluminescence (PL) [93, 98, 99], Pump-push-probe spectroscopy (PPP) [100, 101], terahertz spectroscopy [48, 102], imaging [103] and ultrafast microscopy techniques [90]. This seems to confirm that this phenomenon is not limited to a mistake in interpretation of TA spectra. Although numerical values seem to differ, especially comparing TA or PL broadening studies (which report usually 10s or 100s of ps of cooling times) and studies that focus on a specific wavelength or an average value (TA[87], THz spectroscopy [48, 99] and PPP[100]) which seem to not be able to detect the slowed-down part of the cooling curves, and report times around 1 ps. It seems obvious then, that this peculiar phenomenon is not the result of one (al-

beit complicated) mechanism, but it is the result of several competing mechanisms, which depend on the excess energy and on the carrier density in a non-trivial way. For example, up until now, the problem of carrier thermalization was neglected: TA is capable of measuring the carrier temperature from the broadening of the GSB, but this is meaningful only if the carriers have equilibrated to a thermal distribution, it seems that in MHP this take less than 100 fs, however, also this time seems to be dependent on the carrier density [96, 104].

At the time of writing the accepted view is that, as already observed by Flender *et al.* [89], this slowed-down cooling can be roughly subdivided in two stages: a quick (around 1 ps) stage where the cooling is fast, comparable to GaAs[86], followed by a more or less abrupt passage to a slowed-down cooling (10s-100s ps) which is the signature of this intriguing phenomenon. This dynamic however is likely not the result of one or two processes, as empirical fitting methods seem to require more than two exponentials to accurately model the dynamic [89]. It should be noted however, as already noted, that this is not observed by all reports, in fact there seems to be a marked difference between "spectrally-resolved" studies and "non-spectrally resolved" ones. With this terminology it is not meant that the techniques do not consist of spectrally-resolved data, but that the "spectrally-resolved" (SR) studies extract the temperature from the broadening of the high energy tail of a TA or PL spectrum, while "non-spectrally-resolved" (NSR) track a single wavelength (as the maximum of the GSB in TA) or an averaged wavelength response (as the THz studies). While the SR experiments observe this multiple-stage cooling dynamics and a slow-down of the cooling up to 100s of ps[86, 88, 97, 99], the NSR experiments seem to be sensitive only to the first fast dynamic and less sensitive (if sensitive at all) to the second stage[48, 87, 100, 102]. As such care has to be taken when comparing different works which used different experiments, as sometimes this distinction could be not as clear.

A special case of interest for this work consist in the comparison between TA and THz spectroscopy as both contribute to the results presented in this thesis. TA is possibly the main technique used for these kinds of studies [86, 88, 105], while THz spectroscopy only recently has started to be used for this purpose [48, 102, 106, 107]. A comprehensive study on the different physical phenomena these two techniques probe is reported in Chapter 2, and a systematic comparison of their outcome is one of the results presented in Chapter 5.

As discussed in section 1.3.1 and as will be discussed more deeply in Chapter 3 where the microscopic physics is presented and elaborated to obtain a phenomenological model to describe the HCC dynamics, phonons play a fundamental role in

describing the resulting temperature dynamic. In a similar fashion to classic hot carrier materials, one of the requirements for the enhancement of the hot phonon bottleneck effect is by increasing the phonon band gap [73, 81, 82]. Therefore the first stage of cooling is generally attributed to electron-phonon coupling, specifically LO phonons, through the Fröhlich interaction, possibly enhanced by the HPB effect[14, 88, 103, 108]. The second stage instead is thought to be dominated by the LO phonon decay to acoustic phonons [14], and seem justified by an observed weak coupling between LO and acoustic phonons [97]. Recently it was suggested that only low-frequency modes can be excited[109]. In addition to this picture Fu *et al.* [105] suggested a significant importance of the heating caused by the Auger process. Finally some works have suggested a possible influence of the low thermal conductivity, and generally poor heat transport properties of MHP[95, 110].

Regarding the composition, early reports focused mostly on $MAPbI_3$[86, 88, 89, 93], or $FAPbI_3$[86], showing similar observations. However a study on $A PbBr_3$, with A=FA, MA, Cs, observed a marked absence of slowed-down cooling in the inorganic-cation sample compared to the other two[92]. This was then confirmed by a theoretical and experimental study on the influence of the A-site cation on the HCC[111], a contemporary study on $CsPbI_3$ [112]. In general the organic cation is considered to play an important role [14], but albeit the FA cation seems to be slightly better performing than the MA cation [111], there is no consensus as in other studies they seem equivalent [86] (reported in Figure 1.6). It is clear that both FA and MA MHPs have substantially slower energy relaxation than the inorganic-cation[111], although, regarding the first stage of cooling, Hopper *et al.* [100] and Monti *et al.* [48] found the opposite to be true, which suggests the two stages may be affected differently by the composition. The influence of the X-site is less systematically studied: works have identified the Br-perovskites as having a faster cooling in the first stage (NSR) [108] and a very recent work studied a mixed halide I-Cl finding evidence of slow cooling [113] (using a SR measurement), but no systematic study. Reports on Sn-based perovskites are also scarce, as one report on $FASnI_3$ found evidence of an even more enhanced effect (SR) [114] and one, reported in this thesis in Chapter 4, on $CsSnI_3$ found a slower cooling effect of the first stage (NSR) and attributed it to the anisotropic bandstructure [48]. Recently one work studied the influence of the metal by changing the Pb/Sn ratio and found an enhanced effect in mixed compositions [115].

The enhanced effect in MHP and the influence in composition could be explained by the peculiar phononic characteristics found in these materials. The optical phonon energies are relatively low in MHP, laying in the THz range (few meV)

[55], compared to, say, GaAs (8.5 THz, 35 meV). This lower phonon energy could imply that the first stage of cooling is slower because of more interactions are required to reach the lattice temperature, and perhaps, as they are already populated at room temperature, they could more quickly reach a point where phonon re-absorption is relevant. Both conditions beneficial for HCSC. A comparison of a MHP and GaAs during the first stage of cooling is reported in Chapter 4, and in the corresponding article [48]. For what regards the second stage the current explanation lies in the same framework as traditional hot carrier candidates: suppression of the Klemens decay via a large phonon band gap, an explanation supported by the observations, already mentioned, of a weak interaction between optical and acoustic modes [97].

The recent interest in HCC in MHPs has sparked studies towards more exotic samples, as 2D perovskites [116] (finding an enhanced effect) and on perovskite nanocrystals [117–121].

1.4 Summary

Looking at this complicated picture, where different physical processes intertwine, and different techniques provide non-equivalent information, there is the necessity for studies on different compositions than the "normal" $MAPbI_3$ in order to disentangle the different mechanisms behind this complex phenomenon. It is exactly to address these issues that the work reported in this thesis was undertaken. The focus of this work was the study of electron-phonon and phonon-phonon interaction in different Pb-based and Sn-based MHP. While Chapter 3 provides a detailed overview of the mechanisms at play and builds a phenomenological model capable of describing the complex carrier cooling dynamic and to relate it to the fundamental processes that lie behind it, Chapter 4 presents a study of the carrier cooling in the first stage on a simpler inorganic perovskite, $CsSnI_3$, using THz spectroscopy. The study of the first stage on a simpler system is extremely important, as it allows to limit the number of effects at play. Chapter 5 will present a systematic study of the HCC in mixed lead-tin perovskites with variable Pb/Sn ratio. This allows the tuning of the phonon mode frequencies and thus of the electron-phonon and phonon-phonon interaction. The same chapter compares the outcome of an optical pump terahertz probe experiment with a more common TA experiment, elucidating the similarities and differences in these two techniques, and possibly answer the question whether these two techniques are comparable or not. Finally the last Chapter (6) presents a similar type of study on a III-V semiconductor, InSb, to check the soundness of the THz experiments on a much simpler and better studied system.

Chapter 2

Ultrafast Spectroscopy

This chapter is devoted to the experimental techniques and methods used throughout the course of this thesis. First terahertz (THz) spectroscopy and its derivatives (optical pump terahertz probe, cyclotron spectroscopy) are introduced in section 2.1. Section 2.2 is dedicated to the presentation of transient absorption spectroscopy and how to analyse it to extract the carrier temperature. Finally the last section will introduce the static techniques that have been used sometimes in the course of the work (photoluminescence, absorbance).

2.1 Terahertz spectroscopy

THz spectroscopy is a technique that is nowadays routinely used in condensed matter physics (and beyond) to study the properties of matter in the so called THz range, the section of the electromagnetic (EM) spectrum that lies between the infrared and the microwaves:

- frequency range: 0.1-10 THz
- wavelength range: 3000-30 μm
- wavenumber range: 3.33-333 cm^{-1}
- energy range: 0.4-40 meV.

This part of the EM spectrum is especially interesting for a variety of reasons: quasiparticle excitations, carrier scattering processes, low-frequency phonon modes in solids, molecular rotations and superconducting gaps all have characteristic energies that lie in the THz range. Over of the years, various implementation of THz spectroscopy (transmission, reflection, polarization-resolved, optically-pumped

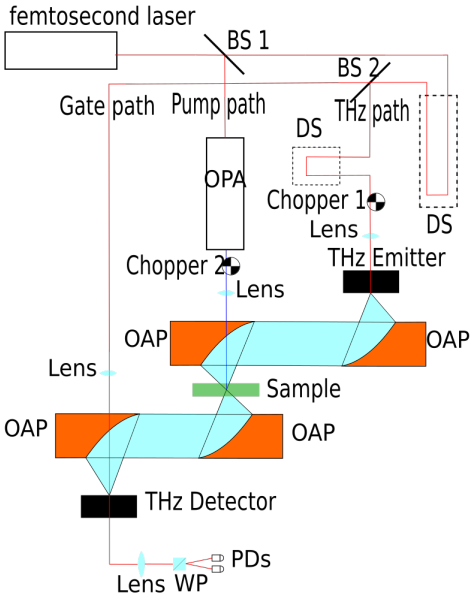

Figure 2.1: A schematic representation of a THz-TDS with an optical pump. BS stands for beam splitter, OAP is off-axis parabolic mirror, OPA is optical parametric amplifier WP is a Wollaston prism and PDs are the photodiodes.

spectroscopy, nonlinear spectroscopy...) have been applied to all of these possible applications and more. Review articles that present a broad overview of terahertz spectroscopy and its different possible applications to semiconductors and novel nano-materials are Ulbricht *et al.* [122], Jepsen *et al.* [123], Baxter and Guglietta [124], Lloyd-Hughes and Jeon [125], Neu and Schmuttenmaer [126]. Recent reviews have focused more on the characterization of nano-materials, such as: Lloyd-hughes [127], Joyce *et al.* [128], Kužel and Němec [129] and metal halide perovskites (MHPs): Johnston and Herz [130].

2.1.1 Terahertz spectroscopy: experimental set-up

Most spectroscopic techniques, in general, work by measuring and recording the light intensity as a function of frequency/energy $I(\omega) = |E(\omega)|^2$. The problem of this approach is the loss of part of information intrinsic in the electric field: the *phase*. Retaining the amplitude and phase of the electric field means that, through a Fourier transform (FT), a complex transmission (and, as will be clear by the end of this section, the complex conductivity) can be easily obtained at all frequencies (within the system's bandwidth). In principle, in frequency-resolved

techniques the phase information can be obtained by using the Kramers-Krönig (KK) relations, however this approach relies on the assumption that the transmission amplitude $|T|$ is known at all frequencies, *i.e.* the spectrum outside the experimental bandwidth is totally negligible. This is not the case for the FT-based approach. An experiment that measures the complex frequency-dependent THz transmission of a sample over a suitable reference is called THz time domain spectroscopy (THz-TDS). The addition of an extra excitation pulse forms a resulting technique called optical pump terahertz probe (OPTP) spectroscopy or, sometimes, time-resolved terahertz spectroscopy (TRTS). In the course of this thesis the first denomination is preferred. Such a technique makes possible to measure the frequency-dependent photo-induced transmission change.

A typical OPTP system is reported in Figure 2.1; without considering the pump line the figure describes a THz-TDS scheme. The scheme represented in the figure can be easily modified, by addition of a magnet, a polarization-resolved detection system or a prism to allow variations of THz spectroscopy such as THz-cyclotron spectroscopy (TCS)[127], polarization-resolved terahertz spectroscopy[131] and thin-film total internal reflection[29].

In all experiments reported in this work (with the exception of the experiments performed in Oxford) the pump beam came of an OPA, an optical parametric amplifier (TOPAS Prime, Light Conversion), which converted the laser pulse from 800 nm into a variable wavelength between 0.3 and 8 μm. This excitation flexibility in principle allows a wide-range of experiments to be performed. The Oxford OPTP system was in all respects very similar to the one represented in Figure 2.1; the main differences are: no OPA, so the sample is excited directly with the 800 nm pump beam, and the fact that the sample was placed inside a helium cryostat inside a superconductive magnet. The spectrometer mostly used throughout this work is based on a Ti:sapphire amplifier (Newport Spectra Physics Spitfire Ace, 13 mJ, 1kHz, 40 fs). The OPA was pumped by 2.5 mJ of the amplifier's beam, generating tunable 50 fs-duration pump pulses in the range from 300 nm to 8000 nm.

The THz pulse in the current work was generated through optical rectification (a second-order nonlinear process in which a low-frequency polarization is developed when a strong laser beam passes in a non centro-symmetric crystal), in a crystal (ZnTe, or GaP). The detection occurs through electro-optic sampling: when the THz beam passed through a nonlinear crystal, it induced a transient birefringence that changed the gate polarization, which was then detected through a quarter wave plate and a Wollaston prism (see Figure 2.1). Alternative generation and detection methods consist of photoconductive antennas based on low-temperature

grown GaAs, spintronic emitters or air-plasma generation. A good discussion of the various methods of generation and detection is reported in Jepsen *et al.* [123] and Baxter and Guglietta [124]; a very recent review of pros and cons of various generation and detection methods is reported in Neu and Schmuttenmaer [126].

The acquisition of the electro-optic signal was then done with a balanced photodiode scheme and a high-precision, high-resolution oscilloscope (Pico Technology PicoScope 4262) for data acquisition. A 4-pulse scheme, with the THz beam chopped at 500 Hz, and the optical pump chopped at 250 Hz, provided the transmitted THz electric field amplitudes E_{off} and E_{on}, and $\Delta E/E = (E_{\text{on}} - E_{\text{off}})/E_{\text{off}}$, where E_{off} and E_{on} are the transmitted electric fields with and without the pump excitation. The short stage in Figure 2.1 controls the time delay between the generated THz pulse and the gate pulse. By changing the optical delay between the two the complete THz waveform can be measured. The long delay stage controls the time delay between the THz (and gate) and the pump beam, allowing for pump-probe experiments where the change between the photoexcited sample's transmitted field and the unexcited sample's transmitted field can be measured as an electric field waveform. Using this approach, applying a FT, it is possible to study the frequency-dependent change in transmission at different time delays after photoexcitation.

Finally, the THz and optical pump beam diameters were measured by the knife-edge method, and yielded a Gaussian profile with standard deviation around 300 μm (relatively consistent in the course of all the experiments) for the THz beam and of variable sizes for the pump beam, depending on the specific wavelength and alignment, but usually ranging between 0.9 mm and 1.5 mm. The optical pump beam was realigned after each wavelength change by maximising $\Delta E/E$ on a GaAs reference sample.

2.1.2 Photoconductivity from terahertz spectroscopy

As discussed in the previous paragraphs, OPTP is a powerful technique that allows the frequency-dependent photoinduced change in transmission to be measured. This is of great importance as the change in transmission is induced by a change of the refractive index. Therefore knowledge of the transmission implies knowledge (within some approximations that will be soon detailed) of the refractive index, and of the dielectric function and conductivity as all such quantities are related to each other.

In order to find an expression for the optical conductivity, starting from the change in transmission, a schematic of the experiment is represented in Figure 2.2 and the refractive indeces of the unexcited sample, photoexcited sample and of the material in front and behind are named: $n_s(\omega)$,$n_i(\omega)$, $n_f(\omega)$ and$n_j(\omega)$. The material

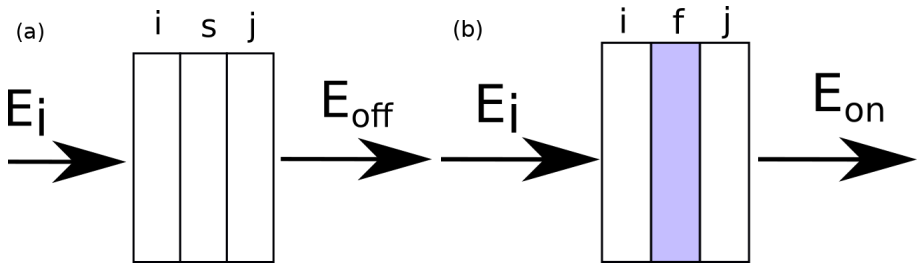

Figure 2.2: Panel (a) schematically represents a non-photoexcited transmission experiment, with a sample film s enclosed between two materials i and j, with an incident electric field E_i and a transmitted electric field E_{off}. panel (b) reports a similar configuration but after photoexcitation of the sample film, denoted as layer f. The transmitted field in this case is denoted E_{on}.

behind could be air (in case of a free-standing film), a substrate, or an unexcited part of the same sample. The material in front is very often air, or, more rarely, an encapsulation with glass or a plastic polymer. Two particular cases are of interest in this thesis and they will be detailed at the end of the section. The electric field before the sample is labelled E_i, and the electric field transmitted through the sample is E_{on} and E_{off} corresponding, respectively, to when the sample is photoexcited or not. Assuming the two materials in front and behind are much thicker so their multiple reflections can be windowed out, the two electric fields can be expressed as:

$$E_{off} = t_{is}t_{sj}e^{in_s\omega\delta/c}FP_{isj}, \tag{2.1}$$

$$E_{on} = t_{if}t_{fj}e^{in_p\omega\delta/c}FP_{ifj}, \tag{2.2}$$

where the Fresnel coefficients are $t_{ij} = \frac{2n_j}{n_i+n_j}$, and FP_{ijk} are the Fabry-Perot (FP) terms that take into account multiple reflections, ω is the light angular frequency, δ is the thickness of the photoexcited region and c is the speed of light in vacuum. The FP terms can be expressed as:

$$FP_{ijk} = \sum_{p=0}^{P}\left[r_{ij}r_{jk}e^{2n\omega\delta/c}\right]^p, \tag{2.3}$$

where the Fresnel coefficients are: $r_{ij} = \frac{n_j-n_i}{n_i+n_j}$. Assuming the photoexcited region δ is optically thin, *i.e.* $n\omega\delta/c \ll 1$ then two important simplifications can happen: (1) the upper limit in Equation 2.3 tends to infinity $P \to \infty$ so:

$$FP_{ijk} = \lim_{P\to\infty}\sum_{p=0}^{P}\left[r_{ij}r_{jk}e^{2n\omega\delta/c}\right]^p = \frac{1}{1-r_{ij}r_{jk}e^{2n\omega\delta/c}}, \tag{2.4}$$

and (2) the exponentials in Equations 2.1 and 2.2 can be expanded in a Taylor series:

$$e^{in\omega\delta/c} \sim 1 + \frac{in\omega\delta}{c}. \tag{2.5}$$

Therefore, defining the transmission $T(\omega)$ as $T(\omega) = \frac{E_{on}(\omega)}{E_{off}(\omega)}$, then the conductivity can be expressed as:

$$\Delta\sigma(\omega) = \frac{(n_i + n_j)}{Z_0\delta}(\frac{1}{T(\omega)} - 1) = \frac{(n_i + n_j)}{Z_0\delta}\left(-\frac{\Delta E}{E_{on}}\right) \simeq \frac{(n_i + n_j)}{Z_0\delta}\left(-\frac{\Delta E}{E_{off}}\right), \tag{2.6}$$

where Z_0 is the impedance of free space, $\Delta E = E_{on} - E_{off}$ and the last equality holds if ΔE is small. In the course of this work these assumptions are almost always met: the MHPs have a thickness between 300-500 nm, for which $\omega\delta/c \sim 10^{-2}$, so although the refractive index in the THz is not well-known it is safe to assume the thin-film limit holds. Regarding the change in the electric field, all the experiments on MHPs in this work were performed with the care to not exceed a $\Delta E/E$ of around 0.1. More care is needed in the case of InSb reported in Chapter 6. In this case at the temperature of 2 K the absorption length at 1.55 eV (800 nm) is around 100 nm, so the optical thickness is: $\omega\delta/c \sim 8 \times 10^{-3}$. In this case the problem of the magnitude of the electric field change is not relevant as the conductivity is never calculated and all experiments are reported in transmission, as will be clear in the section regarding cyclotron spectroscopy (section 2.1.6).

2.1.3 Drude conductivity

An established model to describe the conductivity of semiconductors is the Drude model of conductivity. A detailed description of the model can be found on most solid state physics textbooks, such as Ashcroft and Mermin [132] or Kittel [133] and books on the physics of semiconductors [2]. For the materials of interest in this work, the Drude model describes the frequency dependent conductivity of most semiconductors in the THz range quite well[122, 125], and takes the form:

$$\sigma(\omega) = \frac{Ne^2\tau/m^*}{1 - i\omega\tau}, \tag{2.7}$$

where N is the carrier density, e is the elementary charge, m^* is the effective mass and τ is the momentum scattering time. A typical Drude conductivity is reported in Figure 2.3 for different values of τ. Interestingly, as the momentum scattering time τ becomes smaller, the real part of the conductivity becomes broader, up to the point it could drop off well outside the experimental bandwidth. From basic

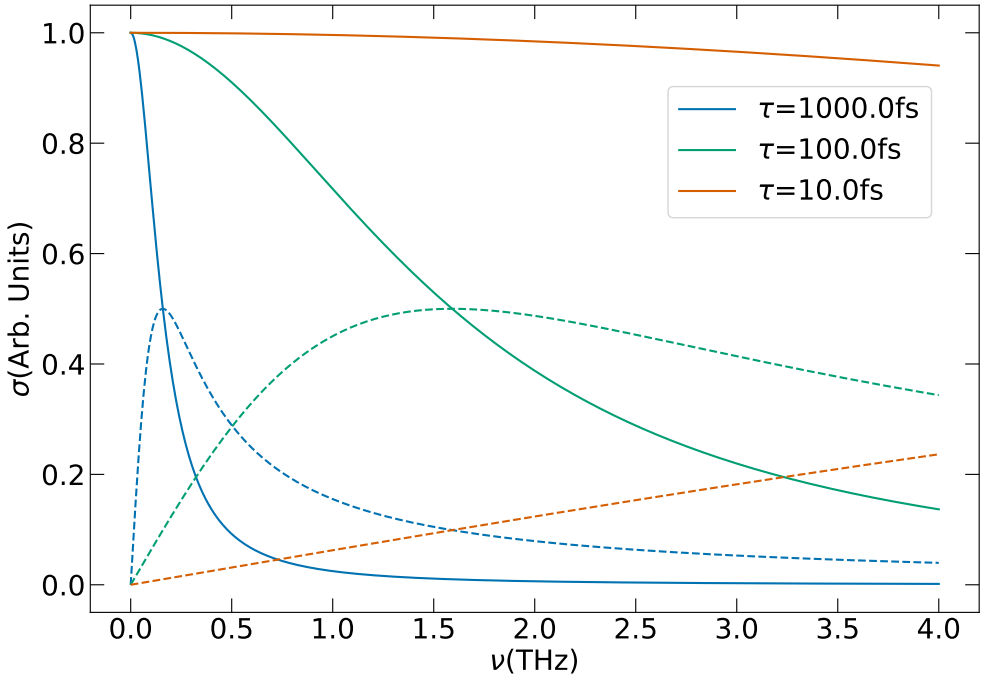

Figure 2.3: Drude conductivity spectra are shown normalised to the real part (continuous lines) for three different momentum scattering times. The imaginary parts are shown by the dashed lines.

solid state physics it is known the static conductivity is directly proportional to the mobility:

$$\sigma_0 = Ne\mu, \tag{2.8}$$

which is the DC limit of the Drude model. Therefore it can be deduced that:

$$\mu = \frac{e\tau}{m^*}, \tag{2.9}$$

and that the Drude conductivity can be expressed as:

$$\sigma(\omega) = \frac{Ne\mu}{1 - i\omega\tau}. \tag{2.10}$$

From which follows that an accurate knowledge of m^* and of τ allows the mobility to be accurately measured from THz spectroscopy techniques. These relationships will be useful when dealing with the study of hot carriers.

2.1.4 Mobility from knowledge of the carrier density

As said, a good way to measure the mobility of a semiconductor is to fit the conductivity spectrum to obtain the momentum scattering time and use known values of the effective mass (from THz cyclotron spectroscopy, for example) to calculate the mobility from Equation 2.9. However if the scattering time is quite short, a Drude spectrum could appear as flat (see Figure 2.3), in such a case, which is typical of MHPs[30], a very common way [30, 130, 134–136] to estimate the carrier mobility is by estimating the sheet carrier density and use it to estimate the mobility, effectively applying Equation 2.8. This methodology will now be reviewed. Starting from the expression of conductivity from the change in the transmitted field:

$$\Delta\sigma(\omega) = -\frac{(n_i + n_j)}{Z_0\delta}\frac{\Delta E(\omega)}{E(\omega)}. \tag{2.11}$$

If the momentum scattering time is small, then: $\Delta\sigma(\omega) \simeq \Delta\sigma_0$. In this case:

$$\Delta\sigma_0 = Ne\mu = -\frac{(n_i + n_j)}{Z_0 d}\frac{\Delta E}{E}. \tag{2.12}$$

To get the absorbed carrier density the incident fluence F (energy per pump pulse per unit area) was calculated; the fluence can be described as $F(r,\theta) = F_0 e^{-r^2/2\sigma^2}$ from the measured Gaussian standard deviation σ and total energy per pulse incident on the sample, E_{pump}. Here, $F_0 = E_{pump}/2\pi\sigma^2$ such that the integral of the fluence over all area yields the energy per pulse. The number of charges generated per unit area is $n(r,\theta) = F(r,\theta)f\phi/E_p$ where E_p is the energy per pump photon, f is the fraction of incident photons absorbed, and ϕ is the quantum efficiency (fraction of absorbed photons that create free charges). Thus

$$n(r,\theta) = n_0 e^{-r^2/2\sigma^2} = \frac{E_{pump}}{E_p 2\pi\sigma^2}\phi(1-R)(1-T)e^{-r^2/2\sigma^2} \tag{2.13}$$

where $f = (1-R)(1-T)$ accounts for the loss of the pump due to power reflection R from the sample, and in transmission T through the sample. It is common to assume $\phi = 1$ for perovskites, however in this work the mobility will often be expressed as the product $\phi\mu$. If the THz pulse is small in area then it samples just the peak of $n(r,\theta)$, i.e. n_0.

Since the THz and pump beams have known profiles the average sheet carrier density $\langle n \rangle$ probed by the beam can be evaluated by integrating the above expression for $n(r,\theta)$ over all area, weighted by the Gaussian profile of the THz pulse. This

yields

$$\langle n \rangle = n_0 \sigma^2 / (\sigma^2 + \sigma_{THz}^2). \tag{2.14}$$

The expression for $\Delta\sigma_0$ (Equation 2.8) can instead be written as a sheet photoconductivity $\Delta S = \Delta\sigma_0 \delta = \langle n \rangle e\mu$, assuming that there is one carrier type with the same mobility (and that μ is not a function of carrier density). Putting all of this together gives the expression

$$\phi\mu = -\frac{(n_i + n_j)}{eZ_0} \frac{2\pi(\sigma^2 + \sigma_{THz}^2)E_p}{(1-R)(1-T)E_{pump}} \frac{\Delta E}{E} \tag{2.15}$$

The transmitted fraction T can be estimated from an absorption measurement. The reflection can be estimated as: $R = |\frac{n-n_i}{n+n_i}|^2$ where n_i is the front material refractive index and n_j is the sample refractive index at the pump wavelength.

2.1.5 Hot carrier cooling

Intraband carrier cooling in semiconductors is a fascinating topic with potentially strong influence in the photovoltaic field, as extensively described in the previous chapter. THz spectroscopy can be used to track the dynamic of hot carriers within the bandstructure, as originally reported by Ralph *et al.* [137] and subsequently by Beard *et al.* [138]. The dynamic of hot carriers can be traced by studying the onset of the photoconductivity rise: as hot carriers lie high in the band the effective mass depends directly on the curvature of the band at that specific energy state:

$$\frac{1}{m^*} = \frac{1}{\hbar^2 k} \frac{dE_c}{dk}, \tag{2.16}$$

where k is the momentum, m^* the effective mass and E_c is the conduction band energy. Here the assumption of an isotropic band has been made, on the contrary in the general case including anisotropy Equation 2.16 becomes a mass tensor. Recalling Equation 2.9:

$$\mu = \frac{e\tau}{m^*} \tag{2.17}$$

where τ is the momentum scattering time, the mobility of hot carriers depends on the position within the bandstructure, and in general higher positions correspond to higher mass *i.e.* lower mobility. Therefore when carriers cool from high in the band to the Γ point (the bottom of the conduction band) they pass from a low mobility state to a high mobility state at the band edges. They then remain there up until recombination occurs. This means that when carriers pass from this low mobility state to an high mobility state the photoconductivity will increase. As the change in

the transmitted THz electric field is directly proportional to the mobility (Equation 2.15), when the mobility increases $\Delta E/E$ increases. It is then possible to track the rise of the transmitted field from zero to its maximum value and directly connect it to the cooling of hot carriers.

In order to quantitatively describe the phenomenon a suitable model (and a consequent fitting function) needs to be established. In this case a simple three-level model has been employed: the carriers in equilibrium have been labelled as ground state (g) (valence band (VB) for holes and conduction band (CB) for electrons), the bottom of the opposite band has been labelled as (Γ) and the variable state high in the band as excited (e). The dynamics of carriers in this simple model can be described by a set of rate equations, assuming one dominant carrier, or the perfect symmetry of the two carriers. The three rate equations are:

$$\begin{aligned} \frac{dN_e}{dt} &= -\frac{N_e}{\tau}, \\ \frac{dN_\Gamma}{dt} &= \frac{N_e}{\tau} - \frac{N_\Gamma}{\tau_{\text{Rec}}}, \\ \frac{dN_g}{dt} &= \frac{N_\Gamma}{\tau_{\text{Rec}}}, \end{aligned} \tag{2.18}$$

where τ is the cooling time between state e and state Γ, and τ_{Rec} is the recombination time between state Γ and g. Given the boundary conditions, which correspond to a total number of carriers N injected to the excited state (e):

$$\begin{aligned} N_e(0) &= N, \\ N_\Gamma(0) &= N_g(0) = 0, \\ N_e(t) + N_\Gamma(t) + N_g(t) &= N, \end{aligned} \tag{2.19}$$

then a solution is easily found:

$$\begin{aligned} N_e(t) &= Ne^{-t/\tau}, \\ N_\Gamma(t) &= N\frac{\tau_{\text{Rec}}}{\tau_{\text{Rec}} - \tau}\left(e^{-t/\tau_{\text{Rec}}} - e^{-t/\tau}\right), \\ N_g(t) &= N\left[1 - \left(\frac{\tau_{\text{Rec}}}{\tau_{\text{Rec}} - \tau}e^{-t/\tau_{\text{Rec}}} - \frac{\tau}{\tau_{\text{Rec}} - \tau}e^{-t/\tau}\right)\right]. \end{aligned} \tag{2.20}$$

Assuming all the photoconductivity arises from the carriers in the state (Γ), *i.e.* that the mobility of the excited state is negligible, the transmitted field can be expressed as:

$$-\frac{\Delta E}{E} \propto \Delta\sigma_0 = Ne\mu \propto N_\Gamma(t) = N\frac{\tau_{\text{Rec}}}{\tau_{\text{Rec}} - \tau}\left(e^{-t/\tau_{\text{Rec}}} - e^{-t/\tau}\right). \tag{2.21}$$

Therefore the function that describes the dynamic of $-\frac{\Delta E}{E}$ is:

$$-\frac{\Delta E}{E} = A\left(e^{-t/\tau_{\mathrm{Rec}}} - e^{-t/\tau}\right). \tag{2.22}$$

If $\tau_{\mathrm{Rec}} \gg \tau$ (a recombination times that is significantly longer than the cooling time, which is true for most semiconductors) then:

$$-\frac{\Delta E}{E} = A\left(1 - e^{-t/\tau}\right). \tag{2.23}$$

However, in case the recombination time is small enough that it becomes comparable with the HCC time the more complex function has to be used.

If the characteristic time of the process is significantly short (*i.e.* comparable with the duration of the THz pulse probe, around 0.3 ps) it becomes necessary to take into account the instrument response, and this is done by defining an instrument response function (IRF) describing the temporal resolution. Modelling the IRF as a Gaussian:

$$G(t) = e^{-t^2/\sigma^2} \tag{2.24}$$

then the convolution of $N_\Gamma(t)$ with $G(t)$ yields:

$$\begin{aligned} N_\Gamma(t) = \frac{\sqrt{\pi}}{2}\frac{\tau_{\mathrm{Rec}}\sigma}{\tau_{\mathrm{Rec}}-\tau}\Bigg\{&\left[\mathrm{erf}\left(\frac{\sigma^2-2t\tau_{\mathrm{Rec}}}{2\sigma\tau_{\mathrm{Rec}}}\right)-1\right]e^{\left(\frac{\sigma^2-2t\tau_{\mathrm{Rec}}}{2\sigma\tau_{\mathrm{Rec}}}\right)^2} \\ &-\left[\mathrm{erf}\left(\frac{\sigma^2-2t\tau}{2\sigma\tau}\right)-1\right]e^{\left(\frac{\sigma^2-2t\tau}{2\sigma\tau}\right)^2}\Bigg\}e^{-t^2/\sigma^2}. \end{aligned} \tag{2.25}$$

In the case $\tau_{\mathrm{Rec}} \gg \tau$ this becomes:

$$N_\Gamma(t) = \frac{\sqrt{\pi}}{2}\sigma\left\{\left[2+\mathrm{erfc}\left(t/\sigma\right)\right]e^{t/\tau} - \left[1+\mathrm{erf}\left(2t\tau-\sigma^2\right)\right]e^{\sigma^2/4\tau^2}\right\}e^{-t/\tau} \tag{2.26}$$

where $\mathrm{erf}(x)$ is the error function and $\mathrm{erfc}(x)$ is the complementary error function. This model will be extensively used to determine the HCC time from terahertz spectroscopy in the subsequent chapters.

2.1.6 Cyclotron spectroscopy

As discussed in the previous sections a vital property of a semiconductor is the effective mass, both because it allows accurate measurements of the mobility (a fundamental parameter for any technological application) and because it contains important information regarding the bandstructure (see Equation 2.16). A tradi-

tional way to measure the effective mass of semiconductors is cyclotron resonance (CR) spectroscopy. A modern implementation of this technique consist in the application of a magnetic field in a THz-TDS or OPTP experiment, taking advantage of the large bandwidth and high signal-to-noise ratio of THz experiments. This section will be relevant when, at the end of this thesis, a simple semiconductor, InSb, will be studied to show a detailed study of the hot carrier dynamics by tracking the effective mass during the process.

In the classical picture, charges under the influence of a magnetic field B move in circular orbits with angular frequency $\omega_c = {}^{eB}/_{m^*}$. In the quantum-mechanical picture, the presence of a magnetic field along z, quantizes the cyclotron orbits in the x-y plane, with energy given by, for 3D semiconductors[127]:

$$E_{n,\sigma} = \left(n + \frac{1}{2}\right)\hbar\omega_c + \sigma g^* \mu_B B, \tag{2.27}$$

where n is an integer that denotes the Landau level (LL) index, σ is the spin ($\pm\frac{1}{2}$), g^* is the g-factor and μ_B is the Bohr magneton. The second term is called Zeeman term. Optically-allowed transitions between LLs are allowed when the index change is $\Delta n = \pm 1$. In case of low magnetic fields (as is the case in this work) the Zeeman term can be neglected as it is smaller than the width of LLs. So the allowed transitions between two LLs exchange energy $E_{n+1} - E_n = \hbar\omega_c$, and therefore carriers in LLs can emit and absorb electromagnetic radiation with energy $\hbar\omega_c = {}^{eB}/_{m^*}$.

For a CR to be experimentally observed the period of the orbit has to be shorter than the time between scattering events, *i.e.* $\omega_c \gg {}^{2\pi}/_{\tau}$, where τ momentum scattering time. Therefore for materials with short scattering time (low mobility) CRs can be observed only at high frequency.

In practice in a TCS experiment the sample is placed inside a superconducting DC magnet, and a normal THz-TDS or an OPTP experiment is performed. The presence of a CR appears as an oscillation in the time domain waveform, and a dip in the transmission $T = \frac{E(B)}{E(0)}$, is observed. The underlying magnetoconductivity can be modelled with a Drude-Lorentz model (similar to a Drude model, but with a resonance centred at finite frequency), however to simplify the analysis, complicated by the very high change in transmitted THz field in InSb (caused by the extremely high mobility), all the analysis was performed on an empirical fit of the transmission resonances using a simple Lorentzian-shaped dip.

In the case of InSb the sample was cooled at 2 K to completely freeze-out all the thermal carriers (present as the band gap is very small, as will be thoroughly discussed in Chapter 6), and carriers were injected with a 1.55 eV (800 nm) pump

beam. The transmission, in this case, was then computed as $T = \frac{E_{on}}{E_{off}}$ as the absence of photoexcitation implied the absence of carriers and thus no resonance was observed. The magnetic field was then swept to measure the cyclotron frequency as a function of the magnetic field and then obtain the effective mass as the slope of $\omega_C(B)$.

These experiments will be extensively discussed in Chapter 6.

2.2 Transient absorption spectroscopy

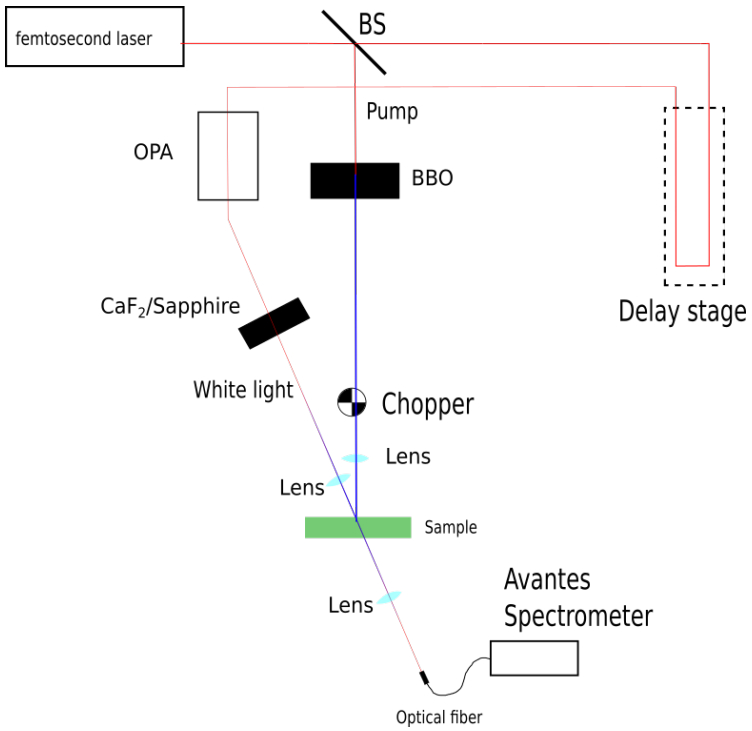

Figure 2.4: A schematic representation of a typical TAS set-up. The angle between the pump and probe beams has been exaggerated for clarity.

Transient absorption spectroscopy (TAS) is a valuable tool capable of investigating the ultrafast excitation dynamics of solids and molecules in the visible range. it consists of a visible or UV pump beam and a white light supercontinuum probe, generated using different materials for different wavelength ranges. A TAS experiment measures the transmitted light with and without the pump, in order to measure the change in the absorption coefficient induced by the pump. Usually the photoinduced change is expressed as the change in optical density, which is

equivalent to:

$$\Delta mOD = -1000 \log \frac{I}{I_0} \tag{2.28}$$

where I and I_0 are the pumped and unpumped transmitted intensities.

2.2.1 Experimental set-up

A typical TAS experiment is reported in Figure 2.4: a femtosecond laser beam (originated from the same amplifier system that fed the THz experiment) is split into a pump and a probe, the pump is 400 nm (3.1 eV) generated in a Beta-Barium-Borate (BBO) crystal, while the probe is a white-light supercontinuum generated either in a CaF_2 window or a sapphire window. The CaF_2 window, pumped by the 800 nm beam allows light to be generated in the 400-850 nm range, while the sapphire, pumped with a 1300 nm beam (coming out of an OPA) generates white light in the 500-1300 nm range. The white light is then detected with an Avantes spectrometer, which has a resolution of 1.2 nm, with an integration time of 0.85 ms, allowing a maximum sample rate of 1.1 kHz, thus fully sampling each pulse of the 1 kHz laser. It is thus able to measure the difference between the probe light intensity when the sample is pumped or unpumped, over a 900nm spectral range.

2.2.2 Photoinduced change in absorption

Having described the experimental method, the theory behind the analysis and interpretation of the resulting data is now discussed. The absorption coefficient of a direct-gap semiconductor can be expressed, including exciton contributions, by the Elliott formula[139]:

$$\alpha = [A\Theta(\hbar\omega - E_g)D_{cv}(\hbar\omega)] \left[\frac{\pi x e^{\pi x}}{\sinh \pi x}\right] + AR_{ex} \sum_{n=1}^{\infty} \frac{4\pi}{n^3} \delta(\hbar\omega - E_g + {}^{R_{ex}}/_{n^2}). \tag{2.29}$$

Where A is a constant related to the transition matrix element, ω is the light frequency, D_{cv} is the joint density of sates, Θ is the Heaviside step function, E_g is the band gap, $\delta(x)$ is the Dirac delta function, R_{ex} is the exciton binding energy and $x = R_{ex}/(\hbar\omega - E_g)^{1/2}$. The first term is the absorption of continuum states, $D_{cv} \propto \sqrt{\hbar\omega - E_g}$ which gives the well-known square root dependence: the term in the square brackets gives the Coulomb enhancement (the Coulomb interaction between electron-hole pairs enhances the interband absorption in the region of the bandgap). The second term describes the contribution of the discrete exciton states that lie below the band gap. Yang *et al.* [86] provided a comprehensive description

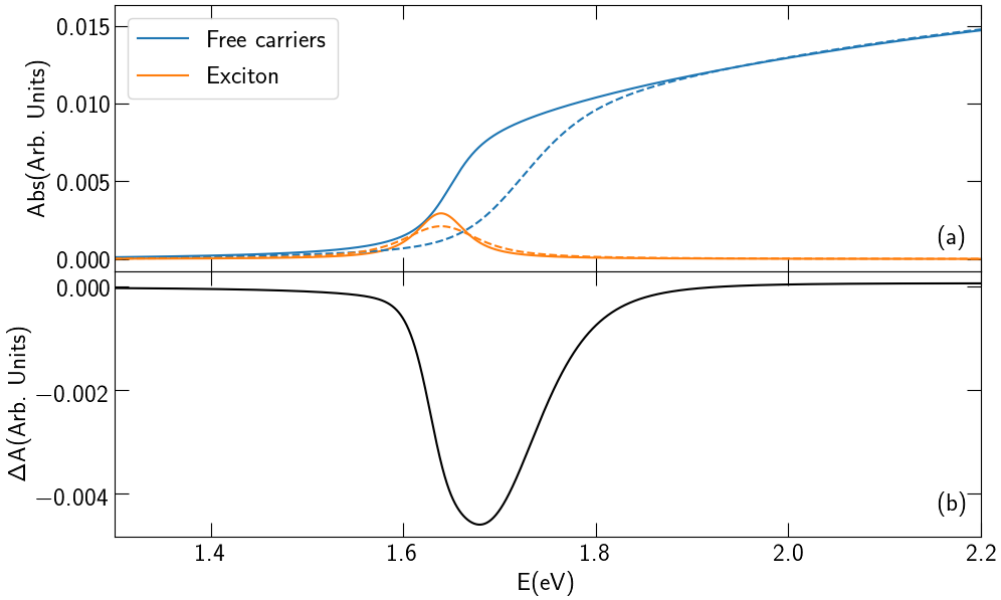

Figure 2.5: Panel (a) equilibrium (continuous lines) and photoexcited (dashed lines) absorption coefficients for free carriers (blue) and excitons (orange). Panel (b) simulated transient absorption spectrum calculated as the difference between the photoexcited and equilibrium absorptions of both exciton and free carrier contributions.

of how these terms are affected by an excess of carriers in a MHP. The two contributions are both affecting the spectral shape of a transient absorption spectrum. This is not entirely obvious for the exciton contribution as most perovskites have exciton binding energies in the 10s of meV range [140], so at room temperature there should be only (or predominantly) free carriers. However it has been noticed [86] that the exciton transitions are necessary to correctly describe the transient absorption spectra. Moreover there is an argument suggesting that in case of high excitation densities the carriers are pushed close enough to form excitons. This possibility has been studied using the Saha ionization equation, providing results that seem compatible with the experimental observations[141]. For all those reasons the exciton contribution cannot be neglected.

An example of an absorption edge modelled by Equation 2.29 is reported in Figure 2.5 (a). There the continuous line represents the equilibrium free carriers (blue) and exciton (orange) contributions for a semiconductor with band gap 1.65 eV and exciton binding energy 10 meV at 300 K. These were calculated from Equation 2.29 convoluted with a Voigt profile to take in account the broadening induced by finite temperature and disorder. The linewidth (Γ) of the Voigt profile was assumed to be 40 meV, which is consistent with the observations and modelling in Yang *et al.*

[86].

It is possible to study how both terms are affected by the injection of carriers by the excitation pulse, which is exactly what is represented as the dashed lines in Figure 2.5. These are calculated as follows. The total transient absorption can be described as[86]: $\Delta A = \Delta A_{free} + \Delta A_{ex}$, where the two terms are obviously the free carriers and exciton contributions. The free carrier part can be calculated as:

$$\Delta A_{free}(E) = A_{free}(E, E_g - \Delta E_g)\left[1 - f_c(E, \mu_q, T_c)\right]^2 - A_{free}(E, E_g). \tag{2.30}$$

Where f_c is the Fermi-Dirac (FD) distribution under photoexcitation, and is characterized by a quasi-chemical potential μ_q and a temperature T_c. $A_{free}(E, E_g)$ is the absorption spectrum before photoexcitation and $A_{free}(E, E_g - \Delta E_g)$ is the absorption coefficient after band gap renormalization (BGR)which will be defined shortly. The modified absorption corresponding to the first term in Equation 2.30 is reported as the dashed line in Figure 2.5. It is implicit in Equation 2.30 that the distributions of electrons and holes are identical: $f_e = f_h = f_c$. This is roughly correct in the case where the effective masses are similar. As a second consequence this assumption implies that $T_e \sim T_h \sim T_c$ at equilibrium, and right after photoexcitation, which is an underlying assumption also in the case of the THz study of carrier cooling.

The exciton contribution to the TA signal can be calculated in a similar fashion:

$$\Delta A_{ex}(E) = A_{ex}(E, \Gamma) * b(n) - A_{ex}(E, \Gamma_0), \tag{2.31}$$

where $b(n)$ is a factor describing the reduction in amplitude of the exciton peak due to photoexcitation and Γ and Γ_0 are the Voigt linewidths after and before photoexcitation. A_{ex} is the Voigt function describing the exciton resonance in the absorption. The reduction and the broadening of an exciton peak due to photoexcitation are documented phenomena[86, 142]. The reduction factor in amplitude is given by: $b(n) = \frac{1}{1+n/n_c}$ where n_c is a critical carrier density at which the amplitude is reduced to half its value. The broadening was observed by Yang *et al.* [86] to grow linearly with carrier density: $\Gamma = \Gamma_0 + c_b n$, where c_b is an experimental parameter. The modified exciton peak is reported as a dashed line in Figure 2.5.

Putting together Equations 2.30 and 2.31 the photoinduced absorption change can be calculated and it is reported in Figure 2.5(b). The resulting change in absorption is a strong bleach at energies above the band gap. There are three competing effects that contribute to this ground state bleach (GSB). The three effects are: the exciton reduction, the Moss-Burstein shift (MBS) and the BGR. The exciton reduction corresponds exactly to the effect described by Equation 2.31, so

it won't be discussed further. The other two are two competing effects that are evident in the free carrier contribution. BGR consists of a redshift in the band gap, induced by the presence of photoexcited carriers, this is taken into account by the parameter ΔE_g in Equation 2.30. The last effect, the MBS, consists of the occupation of states close to the band edge by carriers, which therefore reduce the overall absorption at those energy. This induces an apparent blueshift of the band gap as the states are filled starting at lower energy. In Figure 2.5 (b) on the blue side it is possible to notice a slight photoinduced absorption (PIA), which is a consequence of the BGR[86].

The discussion could be made even more quantitative by quantifying the carrier distribution in energy and consequent quasi-chemical potential by assuming a parabolic, isotropic, non-degenerate band dispersion. In such case the total number of carriers injected is:

$$\begin{aligned} n_0 &= \int_{E_g}^{\infty} n(E)dE = \int_{E_g}^{\infty} D_{cv}(E) f_c(E) dE \\ &= \frac{1}{2\pi}\left(\frac{2m}{\hbar^2}\right)^{3/2} \int_{E_g}^{\infty} \frac{\sqrt{E-E_g}}{e^{(E-\mu/k_B T_c)}+1} dE = 2\left(\frac{m^* k_B T_c}{2\pi\hbar}\right)^{3/2} e^{\left(\frac{\mu-E_g}{k_B T_c}\right)}. \end{aligned} \tag{2.32}$$

Which gives an expression for the total number of injected carriers and an expression for the energy distribution of carriers.

2.2.3 Carrier temperature extraction

This discussion just presented makes it possible to effectively interpret the transient absorption spectra and use it to infer important information such as as the recombination dynamics or the possible dynamics of excitons. Another important outcome of the previous modelling, the most relevant for this work in fact, is the possibility to easily measure the carrier temperature. To explain this, it is useful to refer to Figure 2.6 (a) where the FD distribution (dash-dotted lines) for two different temperatures (300 and 1000 K) have been plotted alongside the corresponding carrier population (continuous lines) and the consequent TA spectra (Figure 2.6 (b)). From the figure it is possible to notice how the tail of the carrier distribution follows quite closely the tail of the FD. This is reflected in the blue-side shape of the GSB: at higher energies the states are occupied according to the FD statistics at finite temperature and therefore the GSB will drop to zero following the same form. It is useful to remember the definition of the FD distribution:

$$f_c = \frac{1}{e^{E-\mu/k_B T_c}+1}. \tag{2.33}$$

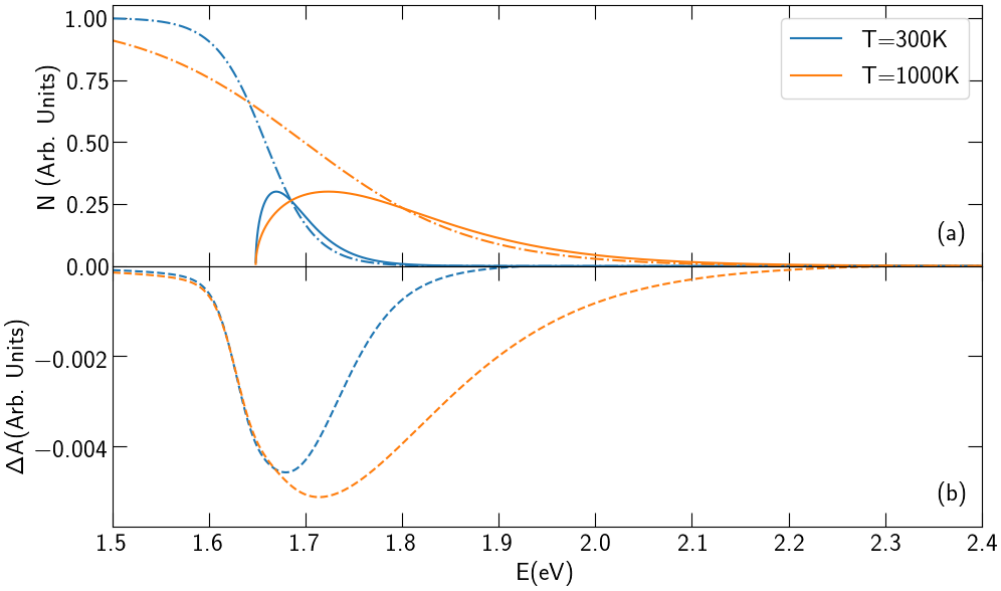

Figure 2.6: Panel (a) FD distributions (dash-dotted lines) and carrier populations (continuous lines) for two different temperatures. Panel (b) corresponding transient absorption, looks clear the slow-down of the high-energy side tail drop-off at higher temperature.

At temperatures around room temperature (and higher) and low particle density (non-degenerate), Equation 2.33 can be approximated with a Maxwell-Boltzmann factor (for a formal derivation, see for example Pathria and Beale [143]):

$$f_c = \frac{1}{e^{E-\mu/k_B T_c}+1} \sim e^{-(E-\mu)/k_B T_c}. \tag{2.34}$$

From this discussion it follows that the blue tail of the TA spectrum follows the tail of a MB distribution. The approach followed in the literature [86, 88, 105, 115, 144, 145], and followed in this work, is to fit the tail of the TA spectra with a decaying exponential, in order to extract the carrier temperature:

$$\Delta A = A_0 e^{-E/k_B T_e} + \Delta A_0. \tag{2.35}$$

Where A_0 is the equilibrium absorption, k_B is the Boltzmann constant, T_c is the carrier temperature and ΔA_0 is an offset that takes into account the broad PIA at higher energies possibly caused by BGR [86] or a photoinduced change in the refractive index[88].

2.3 Complementary spectroscopy techniques

In this brief section the instruments used for basic sample characterization are presented.

2.3.1 Absorbance

The absorbance data were measured with a UV-Vis spectrophotometer (Cary 60), which measures transmission spectra in the 190-1100 nm range. Starting from the transmission data the absorbance was calculated as:

$$Abs = -\log_{10}(T), \tag{2.36}$$

with T the transmission over a suitable reference (usually the sample substrate). Absorbance is important as allows the fraction of absorbed carriers to be extracted, which is crucial in the estimation of the mobility, as reported in section 2.1.4.

2.3.2 Photoluminescence

Photoluminescence (PL) spectra were acquired using an Horiba fluorolog, which allows the PL spectra to be acquired in a broad range of wavelengths. PL is a very useful technique in the field of photovoltaic materials (for a detailed discussion of PL spectra in photovoltaic-relevant material see the relevant chapters in Bisquert [4]), however in this work its use was primarily to extract a precise measurement of the band gap, fundamental to estimate the excess energy at which carriers have been injected. A typical semiconductor PL spectrum is a peak centred at the band gap, so in order to extract the gap values said peaks were fitted with a Gaussian peak:

$$G(E) = Ae^{-(E-Eg)^2/2\sigma^2}, \tag{2.37}$$

where E_g is the band gap, and σ is the standard deviation of the distribution.

2.4 Summary of the chapter

All these models and techniques detailed in this chapter will be of use in the remainder of this thesis, THz spectroscopy of hot carriers will be relevant in Chapter 4, 5 and partly Chapter 6, TCS will be used extensively in Chapter 6, TAS will be applied in Chapter 5.

As a last note, regarding the study of hot carriers, it has been mentioned that both TAS and OPTP were used to study the phenomenon, although the two

techniques rely on substantially different principles. As discussed at the beginning of this thesis and extensively in Chapter 1, the results of these two techniques are not necessarily equivalent *a priori*, but there might be quantitative, if not qualitative, differences between the two. This is an open issue that was intentionally not discussed in this chapter as it will be addressed appropriately in Chapter 5, as the answer is not obvious and consists in a research question in itself.

Chapter 3

Modelling carrier cooling

The cooling of hot carriers in semiconductors and metals is a fascinating phenomenon, interesting from both a fundamental and an application viewpoint, as extensively explained in Chapter 1. In this chapter a description of the hot phonon bottleneck mechanism is given, and a phenomenological model, developed to describe the dynamical change in temperature, is presented. Links between this model and the microscopic physics are drawn.

3.1 Hot carrier cooling processes

The phenomenon of the "hot phonon bottleneck" and, in general, the dynamics of hot carriers, has been extensively studied in recent years [14, 85, 86], thanks to the rising interest in the long cooling times observed in metal halide perovskites (MHPs) [86, 90]. The path from photoexcitation back to equilibrium can not be, however, described as a single process; in fact there are numerous processes happening simultaneously, with different rates. In the following paragraphs the goal will be to describe these processes and identify different regimes which can be then studied by focusing on a single simpler process.

3.1.1 Hot phonon bottleneck

When incident photons with energy higher than the band gap energy arrive at a semiconductor, they generate e-h pairs. The photon energy is distributed to both electrons and holes, which are generated in the conduction band (CB) and valence band (VB). If the photon energy is greater than the band gap the carriers are generated at an energy much higher than the band extrema and have a non-thermal distribution (Figure 3.1 (a)). Subsequently several processes happen:

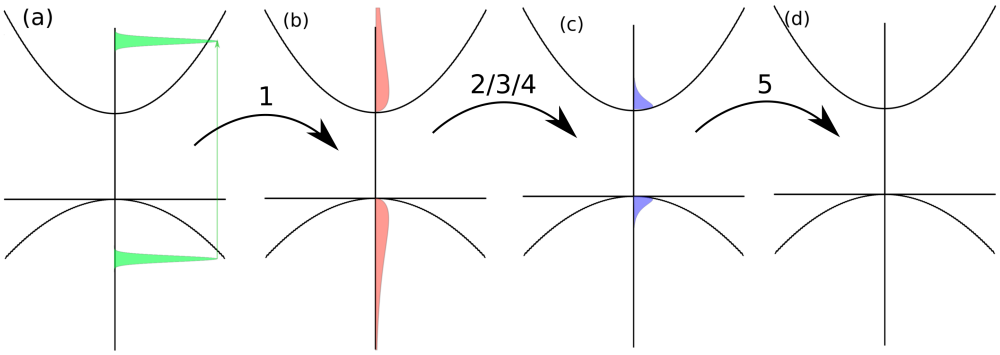

Figure 3.1: A schematic representation of carrier cooling process, as describe in the text. (a) carriers are excited in the band and have a non-thermal distribution, (b) carriers have a Maxwell-Boltzmann distribution but their temperature is much higher than the lattice temperature. (c) after a time that could span between 100s of fs and 100s of ps carriers have cooled down and recombination dynamics dominate (5). (d) The semiconductor has reached the equilibrium it had before the laser pulse excitation.

1. Carriers will equilibrate among each other through elastic carrier-carrier interactions (thermalisation) and will reach a thermal distribution, e.g. described by the Maxwell-Boltzmann (MB) distribution (Figure 3.1 (b))

2. the carriers will undergo cooling by emitting LO phonons and/or acoustic phonons

3. the LO phonon population acquires energy through the electron-phonon interaction and will cede energy via phonon-phonon interaction to acoustic phonons

4. carriers reach a thermal equilibrium with LO phonons, but still have a higher temperature than the lattice. During this regime carriers undergo cooling through acoustic phonon emission

5. Electrons and holes recombine on a 100s of ps to 100s of ns timescale

The process 1, called thermalisation (not to be confused with carrier cooling), undergoes immediately after photoexcitation. The carriers will have a non-thermal distribution of energies (Figure 3.1 (a)) and they will subsequently reach an equilibrium through elastic carrier-carrier scattering and, possibly, at high carrier density, impact ionization and Auger recombination. Once carriers have reached an equilibrium (this usually happens in 10-100 fs) they will occupy states according to

the Fermi-Dirac (FD) statistics (which, for temperatures equivalent of higher than room temperature, can be simplified with a MB distribution), allowing us to define a temperature (hence the name thermalisation): T_e and T_h, for electrons and holes respectively; in general different from each other. These temperatures are much higher than the lattice temperature T_L and therefore the carriers are denoted hot carriers (Figure 3.1 (b)). In this condition it is possible to define two dynamic quasi-Fermi levels: μ_e and μ_h for electrons and holes.

At this point, it is important to stress that all these definitions are dynamical and they are well-defined as long as the timescale of the processes is much shorter than the carriers' recombination time, hence allowing the definition of a dynamical equilibrium. In the case of most semiconductors (and MHPs in particular) this poses no issue since the recombination time is, in the worst case, tens of ps, but generally several ns. As such it is longer than the hundreds of fs considered here, guaranteeing the validity of the definitions. The successive regime (step 2) is dominated by the interaction of the hot carriers with the lattice through the emission of LO phonons and the loss of excess energy. The electron and hole temperatures then reduce and, if the carrier density is not too great, reach the equilibrium value T_L (Figure 3.1 (c)). The time needed for the latter process is the energy relaxation time τ_E, which is the subject of the study of this work. In the case that the injected carrier density is high, this simple representation must be slightly modified, as it was presumed that a certain number of carriers exchange energy with the phonon bath without affecting it, *i.e.* without increasing the phonon population. In reality the cooling process is more complex. In polar semiconductors the energy loss occurs through the so-called Fröhlich interaction[146, 147]: carriers interact with LO phonons, and exchange energies that are multiples of the lowest phonon energy. Therefore lower phonon energy tends to slow this step of the cooling. Interaction with acoustic phonons also takes place, but the energy exchanged per interaction is negligible since these interactions happen close to the zone centre where the acoustic phonon energy is minimal. LO phonons can decay into two (or more, but the process is proportionally suppressed) acoustic phonon (step 3). Thus, at later times, acoustic phonons are the main mechanism for heat dissipation, which could be more or less efficient depending on the thermal conductivity.

The key process here is the decay of an LO phonon into two acoustic phonons. The different ways this could happen will be discussed in section 3.2.4 and are schematically represented in Figure 3.5. Depending on the phonon bandstructure this process can be more or less efficient, up to the point where it could be much more inefficient (*i.e.* slower) than the Fröhlich cooling. In this case the LO phonon

population can't disperse the energy acquired from the hot carriers to the acoustic phonon quickly enough and the LO phonon temperature rises. In this case the carrier-LO phonon system reaches a dynamic equilibrium where the Fröhlich interaction doesn't cool down the carriers because of the equal carrier and LO phonon temperatures, and the system's cooling is limited by the phonon-phonon interaction. This phenomenon is called the "hot phonon bottleneck" (step 4), where the system dissipates heat through acoustic phonons. Finally (step 5), electron-hole recombination dominates and the semiconductor will reach the original equilibrium condition (Figure 3.1 (d)). A more detailed description of the phonon decay processes will be given in the following sections, where the Three-temperature model (TTM) will be described.

3.1.2 Influence of the Auger process

The previous discussion, following the established description of the cooling in perovskites[14, 85], ignored the impact of Auger heating. The Auger process is a well-known process in semiconductors (see for example Yu and Cardona [2], Seeger [147]), which consists of an electron and a hole recombining by giving energy to a third electron. The influence of Auger events in the recombination dynamics of perovskite semiconductors is well-established[130], as the charge-carrier recombination dynamic in MHPs is governed by monomolecular as well as higher order processes. The dynamic is easily described by a rate equation[130]:

$$\frac{dn}{dt} = G - k_1 n - k_2 n^2 - k_3 n^3, \tag{3.1}$$

where n is the carrier density, G is the charge-density generation rate, k_1 is the monomolecular recombination rate constant, k_2 is the bimolecular electron-hole recombination rate constant and k_3 is the Auger recombination rate constant. At higher carrier densities, then, the recombination dynamic is dominated by bimolecular recombination and Auger recombination. However, even in cases where the Auger recombination rate is not dominating the recombination its influence on the carrier temperature cannot be neglected. If the carrier density is high enough then the process happens often enough to slightly warm up the carrier distribution. Because of that, the influence of the Auger mechanism in the heating of hot carriers is thought to be relevant [105, 119]. In the following sections cooling dynamics are described using the "three-temperature model" combined with the Auger process.

3.2 Three Temperature Model

A phenomenological approach based on the three-temperature model (TTM) was developed. This model was applied previously to the electron-phonon interaction in the metals Au and Ag [148] and to spin-lattice relaxation in manganite oxides[149]. This approach is intended to provide an intuitive and quantitative way to describe the different cooling regimes, including the hot phonon bottleneck mechanism, in halide perovskites. Previously, two analysis methods have been reported: an empirical approach, aimed to obtain a quantitative fit to experimental data but without links to the microscopic mechanisms[115], and a more complete microscopic approach[105]. This second approach calculated the energy loss rate including the heating of the phonon population in the Fröhlich scattering model. This is complex to implement, computationally demanding, and requires a detailed knowledge of microscopic quantities such as the effective mass, static and high frequency dielectric constants, and LO phonon energies. Some of these constants are difficult to measure in particular halide perovskites: for instance Sn-rich compounds exhibit high levels of p-doping, making it difficult to determine phonon frequencies and the static dielectric constant[150]. Further, these parameters are often unknown for more complex compounds, such as the triple cation alloys investigated in this work.

3.2.1 TTM: mathematical description

Here, in the TTM a pair of coupled rate equations describe the interaction of the (hot) carrier temperature T_c with the phonon temperature T_p, and the coupling of the phonons to the lattice, at temperature T_L. Note that this approach is sometimes called the *two* temperature model in the literature: the name three temperature model highlights the independent temperatures of the three sub-systems. The most general presentation of this model assumes N phonon branches and N temperatures[151, 152] to which the influence of Auger heating was added:

$$C_e \frac{dT_c}{dt} = \nabla \left(k_e \nabla T_c \right) - \sum_{i=1}^{N} G_{ep,i} \left(T_c - T_{p,i} \right) + G_A \left(T_c + T_g \right) + \Xi(t) \tag{3.2}$$

$$C_{p,i} \frac{dT_{p,i}}{dt} = \nabla \left(k_e \nabla T_p \right) + G_{ep,i} \left(T_c - T_p \right) - G_{pp,i} \left(T_{p,i} - T_L \right), \tag{3.3}$$

Here C_e, C_p, k_e, k_p, $G_{ep,i}$, $G_{pp,i}$ are respectively the electron heat capacity, the phonon heat capacity, the electron thermal conductivity, the phonon thermal conductivity, the coupling constant of electron with the i-th phonon branch and the

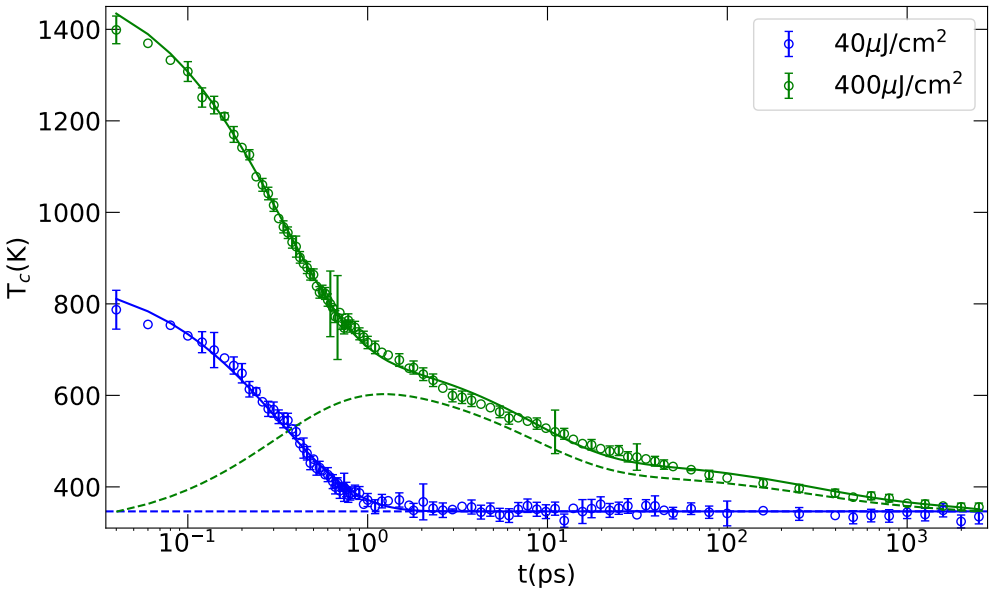

Figure 3.2: Cooling dynamic of a sample of $Cs_{0.05}(FA_{0.83}MA_{0.17})_{0.95}Pb(I_{0.83}Br_{0.17})_3$ at low and high fluence. Continuous lines are fits using models described in the text, dashed lines are the corresponding calculated phonon temperatures.

coupling constant of the i-th phonon branch with the lattice. $\Xi(t)$ is the heating caused by the laser pulse. The last term in Equation 3.4 represents Auger heating, where $T_g = 2E_g/3k_B$ and $G_A = k_A N^2(t)$ for Auger recombination rate k_A and carrier density $N(t)$[105, 153]. In this work only one optical branch will be considered, of the 36 possible modes [27], and its coupling with the lattice reservoir. It will be assumed that the coupling of electrons with acoustic phonons is negligible and that acoustic phonons are in equilibrium with the lattice, hence the expressions "lattice" and "acoustic phonons" will be used interchangeably. In the approach followed in this work heat transport (the spatial derivatives) is neglected and it is assumed that the laser only initialises the carrier population at $T_c = T_0$. Given all of that the equations proposed are as follows:

$$C_e \frac{dT_c}{dt} = -G_{ep}\left(T_c - T_p\right) + G_A\left(T_c + T_g\right) \tag{3.4}$$

$$C_p \frac{dT_p}{dt} = +G_{ep}\left(T_c - T_p\right) - G_{pp}\left(T_p - T_L\right). \tag{3.5}$$

The terms $\pm G_{ep}\left(T_c - T_p\right)$ correspond to coupling between hot electrons and hot phonons, while the coupling of hot phonons to the lattice is described by $G_{pp}\left(T_p - T_L\right)$. These equations are not solvable analytically, so a numerical so-

lution is, in general, necessary.

An example of the cooling curves the model attempts to describe is reported in Figure 3.2. The cooling curves for a sample of $Cs_{0.05}(FA_{0.83}MA_{0.17})_{0.95}Pb(I_{0.83}Br_{0.17})_3$ are reported for 40 and 400 $\mu J/cm^2$ fluence excitation. In the high fluence curve, the persistence of higher temperatures in the range 1-100 ps is a clear evidence of the appearance of an hot phonon bottleneck and consequent slow-down of the cooling dynamic. This sample will be reported in more detail in Chapter 5.5. The high-fluence curve was fitted using the model presented and an excellent match with the experimental data was obtained, yielding: $G_{ep}/C_e = 2.3$THz, $G_{pp}/C_p = 0.2$THz and $G_A(0)/C_e = 0.14$THz. In order to numerically fit the data it was required to provide an explicit form of $G_A(t)$. As the time-dependence is implicit in the carrier density $N(t)$, the carrier dynamics in the sample was fitted with a two-exponential decay and the resulting fitting curve was substituted into the expression for $G_A(t)$. The Auger heating term is thought to be important for perovskites[105], and its inclusion here was necessary to model the long-lived tail in T_c evident at high excitation fluences (e.g. at 400 μJcm^{-2} in the Figure). The dashed lines represent the calculated dynamic of the phonon temperature. However, for measurements at intermediate fluences ($< 100\,\mu Jcm^{-2}$) the Auger term was not needed to correctly reproduce the dynamics of the compositions investigated in this work. Therefore in the following chapters this term will often be ignored, and because of that a simplified version of the model will now be discussed.

Without the Auger term, and subject to the initial conditions $T_c(t=0) = T_0$ and $T_p(t=0) = T_L$, the rate equations are solvable analytically. A solution was found using the python symbolic calculation library SymPy, yielding

$$T_c(t) = T_L + A_+ (T_0 - T_L)\, e^{-t/\tau_+} + A_- (T_0 - T_L)\, e^{-t/\tau_-} \tag{3.6}$$

$$T_p(t) = T_L + B_+ (T_0 - T_L)\, e^{-t/\tau_+} + B_- (T_0 - T_L)\, e^{-t/\tau_-}. \tag{3.7}$$

After the pump pulse has rapidly heated the carriers to T_0, the hot carrier temperature recovers exponentially, with a fast time constant τ_+, and a slower decay given by τ_-. The decay rates $k_\pm = 1/\tau_\pm$ are:

$$\frac{1}{\tau_\pm} = \frac{G_{ep}+G_{pp}}{2C_p} + \frac{G_{ep}}{2C_e} \pm \frac{1}{2}\sqrt{\left(\frac{G_{ep}+G_{pp}}{C_p} - \frac{G_{ep}}{C_e}\right)^2 + \frac{4G_{ep}^2}{C_e C_p}}, \tag{3.8}$$

and the amplitudes of the terms in Equations 3.7 and 3.6 are $A_+ = (k_0 - k_-)/(k_+ - k_-)$, $A_- = (k_+ - k_0)/(k_+ - k_-)$, $B_+ = \left(\frac{k_-}{k_0} - 1\right) A_-$, $B_- = \left(\frac{k_+}{k_0} - 1\right) A_+$, with $k_0 = G_{ep}/C_e$. The dimensionless amplitudes $A_\pm$ control the relative weight of the

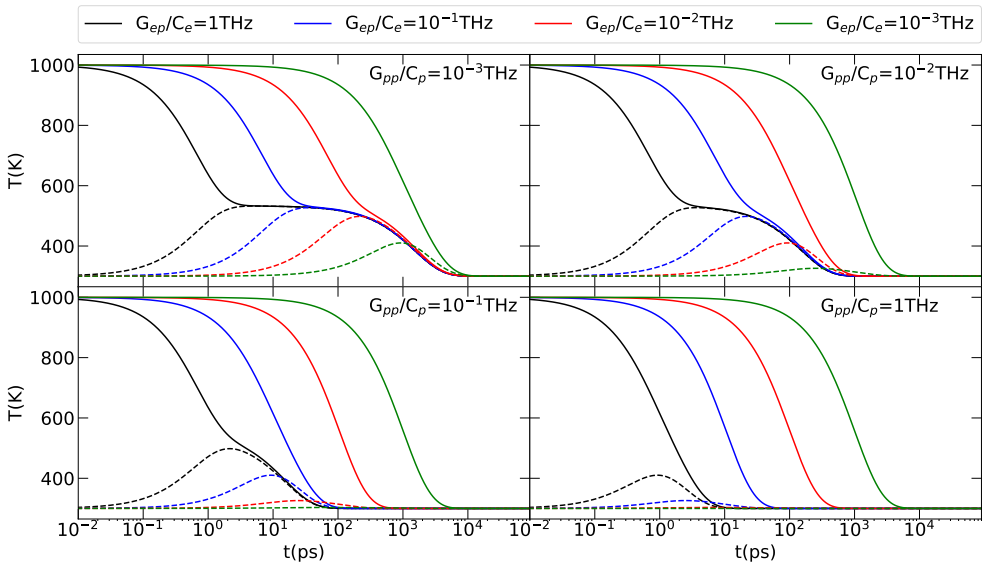

Figure 3.3: Simulation of electron (continuous lines) and phonon (dashed lines) temperatures. Black, blue, red and green correspond to G_{ep}/C_e= 10, 1, 10^{-1} and 10^{-2} THz respectively. The four plots correspond to G_{pp}/C_p= 10^{-3}, 10^{-2}, 10^{-1} and 1 THz. The ratio of C_e/C_p was kept at 0.5 to better enhance the hot phonon effect in the figure.

fast and slow components, and obey the expression $A_+ + A_- = 1$. Interestingly, the ratio of the two amplitudes is determined by the ratio of the electron and phonon heat capacities. This will be detailed in the subsequent paragraphs.

Physical insights into the TTM and its free parameters, which, from Equation 3.8, are G_{ep}/C_e, G_{ep}/C_p and G_{pp}/C_p, are now provided.

3.2.2 Three temperature model: physical description

The TTM assumes that the carrier temperature is coupled with the phonon temperature via a coupling constant, G_{ep}. When the carrier temperature T_c is high, the efficient carrier-LO phonon interaction transfers energy from carriers to the LO-phonon bath, raising its temperature, T_p. This process takes around 1 ps (Figure 3.2). The LO-phonon bath tries to reduce its temperature by LO-phonons decaying into lower energy acoustic and/or optical phonons, at a rate controlled by the coupling constant G_{pp}. In general the fast and slow decay times $\tau_\pm$ cannot be uniquely identified with carrier-phonon coupling and LO-phonon decay, as both terms enter into Equation 3.8. However now a detailed description of the underlying physical processes is given, in order to gain insights into their relative magnitude, and show that for certain values of the parameters the fast decay τ_+ corresponds to the carrier

cooling time, while τ_- is controlled by the hot phonon decay rate.

A good way to visualise the influence of the coupling rates on the cooling dynamic is to systematically vary the parameters, as presented in Figure 3.3. Each plot presents a simulated cooling curve for four different electron-phonon coupling rates, each plot for a different phonon-phonon coupling rate, all with a fixed C_e/C_p ratio of 0.5 to enhance the effect and better visualize it. The figure shows quite clearly how the coupling rate G_{ep}/C_e controls the quickness of the first cooling stage, while G_{pp}/C_p if small enough, induces the appearance of a second, slower, cooling stage (e.g. in the top left panel). Depending on the ratio of the two couplings the appearance of the second stage is more or less delayed, up to the point where it could completely disappear.

In general the phonon contribution to the heat capacity at room temperature is larger than the electronic contribution[148]. In this limit, the parameters G_{pp}/C_p and G_{ep}/C_p of the TTM are small compared to G_{ep}/C_e, and the carrier temperature decays at a rate $k_+ \simeq G_{ep}/C_e = k_0$ with a negligible slow component (as $A_- \simeq 0$). In this case the microscopic processes contributing to G_{ep} can be discussed with the following simple approach, which assumes that scattering from a single LO phonon mode cools electrons within a single, spherical band. The rate of change of the electron temperature can be approximated by $dT_e/dt = -k_0(T_e - T_p)$. Within this approximation it is possible to recover an expression for the coupling rate k_0 starting from the Fröhlich interaction.

3.2.3 Fröhlich cooling

In order to model the energy loss rate by the electron-phonon interaction the Fröhlich treatment of electron-LO phonon interaction has to be introduced. In polar semiconductors (such as GaAs or metal halide perovskites) the electron-LO phonon interaction is known to dominate the intraband energy loss mechanism [146, 147]. Electron-acoustic phonon scattering is thought to yield a negligible energy loss rate.

The Fröhlich electron-phonon interaction represents the interaction of an electron with the surrounding lattice. This interaction can be described by the Fröhlich Hamiltonian[2, 58]:

$$\mathcal{H}_F = \sum_q i\frac{C_F}{q}\left[c_q^\dagger e^{i(\vec{q}\cdot\vec{r}-\omega_{LO}t)} - c_q e^{-i(\vec{q}\cdot\vec{r}-\omega_{LO}t)}\right], \tag{3.9}$$

where q is the phonon momentum, $c_q^\dagger$ and c_q are the phonon creation and annihilation

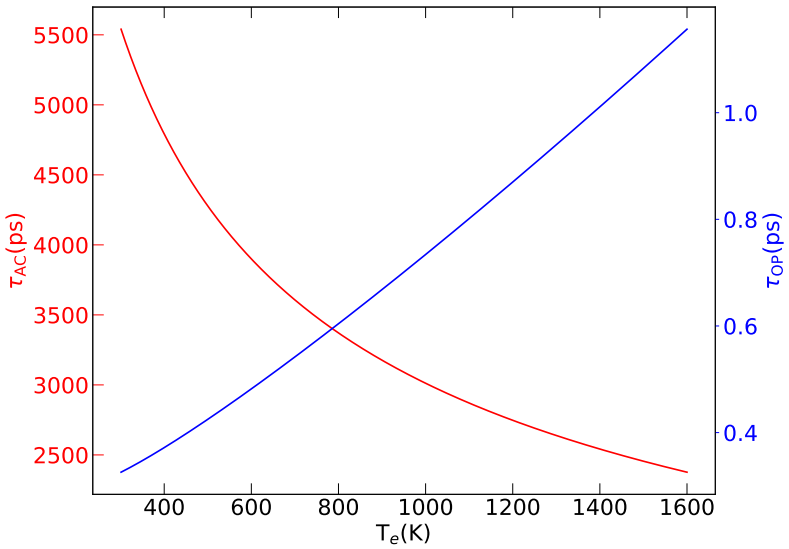

Figure 3.4: Calculations of optical (blue) and acoustic (red) scattering time as a function of carrier temperature for GaAs from Equations 3.15 and 3.17 respectively.

operators, and:

$$C_F = \frac{e}{(4\pi\varepsilon_0)^{1/2}} \left[\frac{2\pi\hbar\omega_{LO}}{NV} \left(\frac{1}{\varepsilon_\infty} - \frac{1}{\varepsilon_s} \right) \right]^{1/2} \tag{3.10}$$

$$= \left(\frac{\alpha}{NV} \right)^{1/2} \left(\frac{2\pi\hbar\omega_{LO}}{m^3} \right)^{3/4}. \tag{3.11}$$

Here, k_B is the Boltzmann constant, $\hbar\omega_{LO}$ is the LO phonon energy, ε_s and ε_∞ are the static and high frequency dielectric constants, m^* is the bare electron mass, N is the number of electrons and V is the total volume. Moreover α is defined as:

$$\alpha = \frac{e^2}{4\pi\varepsilon_0\hbar} \left(\frac{m^*}{2\hbar\omega_{LO}} \right)^{1/2} \left(\frac{1}{\varepsilon_\infty} - \frac{1}{\varepsilon_s} \right), \tag{3.12}$$

which is the dimensionless Fröhlich constant.

In order to describe the average cooling rate given by Fröhlich interaction it is necessary to start from an analytical description of the energy loss rate. The Fröhlich cooling rate is the net rate between the emission and absorption of phonons in collision events. From Seeger [147] such a description can be found by taking the average, over a Maxwell-Boltzmann distribution, of the energy loss occurred in such events:

$$-\left\langle \frac{d\varepsilon}{dt} \right\rangle_{coll} = \frac{2^{3/2}\alpha}{\pi^{1/2}\hbar} \left(k_B\Theta\right)^2 \left(\lambda z\right)^{1/2} K_0\left(\lambda z\right) \frac{\sinh\left[\left(1-\lambda\right)z\right]}{\sinh\left(z\right)}, \tag{3.13}$$

where ε is the carrier energy, $\lambda = T/T_e$, $z = \Theta/2T$ and Θ is defined as $k_B\Theta = \hbar\omega_{LO}$. T_e is the hot electron temperature, T the lattice temperature, K_0 the modified Bessel function of the second kind. From this, assuming that it is possible to describe the energy loss rate as:

$$-\left\langle \frac{d\varepsilon}{dt} \right\rangle_{coll} = \frac{3}{2}k_B\frac{(T_e - T)}{\tau} = \left[\langle\varepsilon(T_e)\rangle - \langle\varepsilon(T)\rangle\right]/\tau, \tag{3.14}$$

then it should be possible to recover an expression for the energy loss characteristic time:

$$\tau = \frac{3\pi^{1/2}\hbar}{4\alpha k_B}\frac{\sqrt{T_e}\,(T_e - T)}{\Theta^{5/2}K_0\,(\Theta/2T_e)}\frac{\sinh\,(\Theta/2T)}{\sinh\left[(T_e - T)\right]\Theta/2T_eT}. \tag{3.15}$$

In principle the same approach can be followed considering acoustic phonon scattering, yielding:

$$-\left\langle \frac{d\varepsilon}{dt} \right\rangle_{coll} = \frac{2mE_{AC}^2}{\pi^{3/2}\hbar\varrho}\left(\frac{2mk_BT_e}{\hbar^2}\right)^{3/2} 2\frac{T_e - T}{T_e}\frac{F_1(\eta)}{F_{1/2}(\eta)}, \tag{3.16}$$

where ρ is the mass density, E_{AC} is the deformation potential constant, $\eta = \xi/k_BT$ and $F_j(\eta) = \frac{1}{j!}\int_0^\infty \frac{x^j dx}{e^{x-\eta}+1}$[147]. Using the same definition for the energy loss rate (Equation 3.14), a formulation for the energy loss time for acoustic phonons can be found:

$$\tau = \frac{3}{8}\left(\frac{\pi}{2}\right)^{3/2}\frac{\hbar^4\varrho}{m^{5/2}E_{AC}^2}\frac{1}{\sqrt{k_BT_e}}\frac{F_{1/2}(\eta)}{F_1(\eta)}. \tag{3.17}$$

Both τ_{LO} and τ_{Ac}, calculated for GaAs, are plotted in Figure 3.4 as a function of the hot electron temperature. As can be easily seen the values for acoustic phonon scattering are substantially larger, which means, given the fact that the total rate is given by the sum of the single rates, that the acoustic phonon scattering time is negligible.

3.2.4 Electron-phonon and phonon-phonon interaction mechanisms

Using the results obtained in the previous section, it is possible to express the coupling rate k_0 as the Fröhlich coupling rate (from Equation 3.15):

$$k_0 = \frac{G_{ep}}{C_e} = \frac{4\alpha k_B}{3\pi^{\frac{1}{2}}\hbar}\frac{\Theta^{\frac{5}{2}}K_0(\Theta/2T_e)}{\sqrt{T_e}(T_e - T_p)}\frac{\sinh\left[(T_e - T_p)\Theta/2T_eT_p\right]}{\sinh\,(\Theta/2T_e)}. \tag{3.18}$$

In the TTM model is assumed that k_0 is a constant, rather than depending on the carrier temperature and the phonon temperature as described in Equation 3.18.

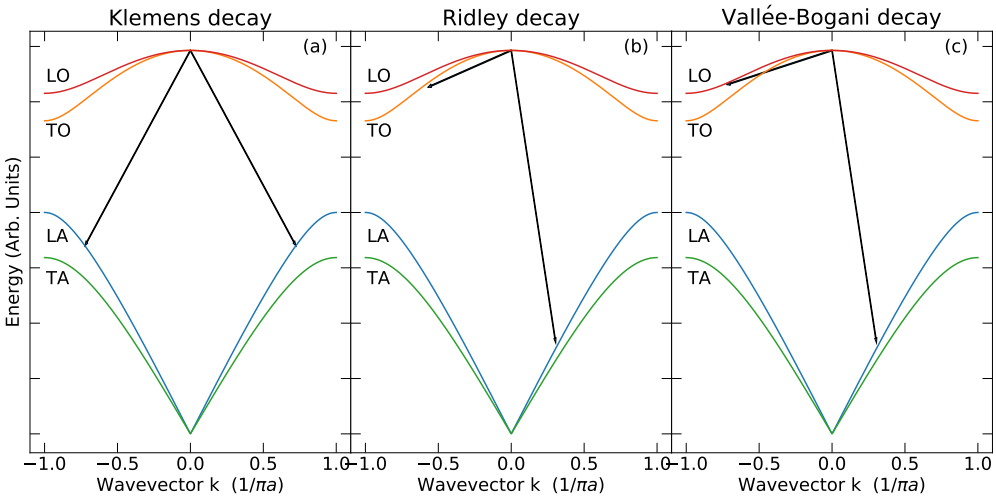

Figure 3.5: A schematic representation of the three main phonon-phonon decay channels: Klemens, Ridley, and Vallée-Bogani. For the sake of simplicity and clarity in the representation the arrows do not conserve energy and momentum.

However it can be argued, based on Equation 3.18 that τ_+ decreases (k_+ increases) when the phonon frequency increases, or when the Fröhlich constant is higher.

Turning now to consider the coupling between hot LO-phonons and the lattice: the magnitude of G_{pp} is expected to be smaller than G_{ep} because the phonon-phonon interaction is an anharmonic process. There are different ways in which a zone-centre LO phonon can decay and these are schematically represented in Figure 3.5. These decay mechanisms are: the Klemens channel, where an LO phonon decays into two acoustic phonons of opposite wavevectors[154] (Figure 3.5(a)); the Ridley channel, creating a transverse optical and an acoustic phonon[155](Figure 3.5(b)); and the Vallée-Bogani channel, where another LO phonon and an acoustic phonon are produced[156] (Figure 3.5(c)). Other channels as the Barman-Srivastava or four-phonon processes are not relevant as they are connected respectively to the wurzite structure and to higher temperatures[157, 158]. Therefore the phonon-phonon coupling rate can be expressed as:

$$\frac{G_{pp}}{C_p} = \frac{1}{\tau_K} + \frac{1}{\tau_R} + \frac{1}{\tau_{VB}} \tag{3.19}$$

where τ_K, τ_R and τ_{VB} are the Klemens, Ridley and Vallée-Bogani decay times. Explicit formulae for the various decay rates are reported in Barman and Srivastava [157].

The power of the TTM lies in the simple and quantitative picture of the

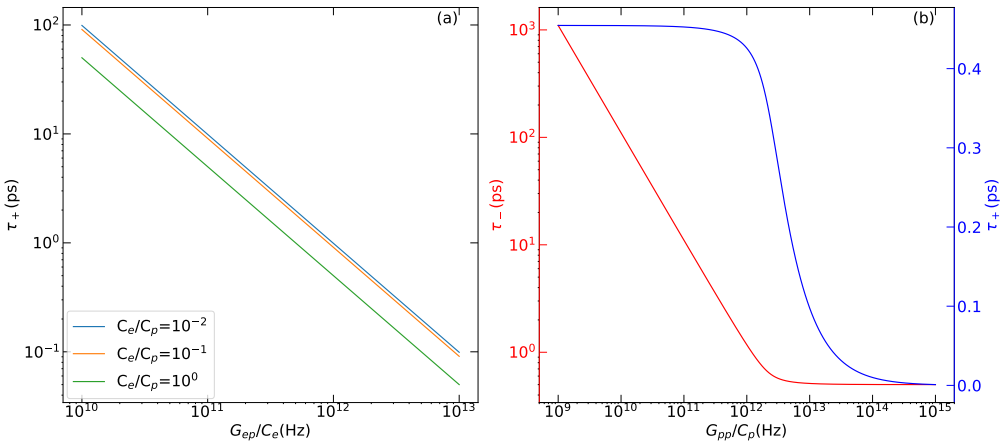

Figure 3.6: (a) Calculated τ_+ from TTM as a function of G_{ep}/C_e, for different values of C_p/C_e. (b) Dependence of τ_+ (right, blue, linear y axis) and τ_- (left, red, logarithmic y axis) on G_{pp}/C_p, for a fixed $C_p = 10C_e$ and $G_{ep}/C_e = 2\,\mathrm{THz}$.

various stages of cooling and in the connection to quantities that can be directly measured, concentrating all the microscopic parameters in few effective constants. Unfortunately, apart from a few reports for $MAPbI_3$[159, 160] accurate measurements of the heat capacity and of the coupling constants are lacking. Therefore, to estimate feasible values of the parameters, we first calculated how the decay time τ_+ varies with G_{ep}/C_e for realistic ratios of C_p and C_e (with $C_p > C_e$). The results are reported in Figure 3.6 (a) for $C_p/C_e = 1$, 10 and 100. The fast cooling time obtained by experiment is below 1 ps, which can be seen to require $k_0 = G_{ep}/C_e \geq 1\,\mathrm{THz}$.

A representative value of $k_0 = 2\,\mathrm{THz}$ and $C_p/C_e = 10$ was adopted in order to explore how changing the phonon-phonon coupling strength G_{pp} alters τ_+ and τ_-, as reported in Figure 3.6 (b). The fast component was almost unchanged when the phonon-phonon coupling strength was varied over many orders of magnitude: τ_+ decreases substantially only for $G_{pp}/C_p \geq k_0 = 2\,\mathrm{THz}$. In stark contrast, the slow component τ_- was dramatically affected by G_{pp}: an order of magnitude reduction in coupling constant yields an order of magnitude increase in decay time. It is therefore possible to conclude that the initial decay in carrier temperature is dominated by the Fröhlich interaction (G_{ep}/C_e), while the slower decay τ_- is linked to G_{pp}/C_p.

Finally, it is worth pointing out that from the ratio of the two amplitudes $A_\pm$ it should be possible to estimate the ratio of the two heat capacities. A calculation of the resulting amplitude ratio by varying the ratio C_e/C_p, keeping G_{ep}/C_e=1 THz constant, is reported in Figure 3.7 for different strengths of the phonon-phonon coupling. Interestingly as the ratio C_e/C_p gets smaller the amplitude A_+ becomes significantly larger than A_-, provided the phonon-phonon coupling is weak enough.

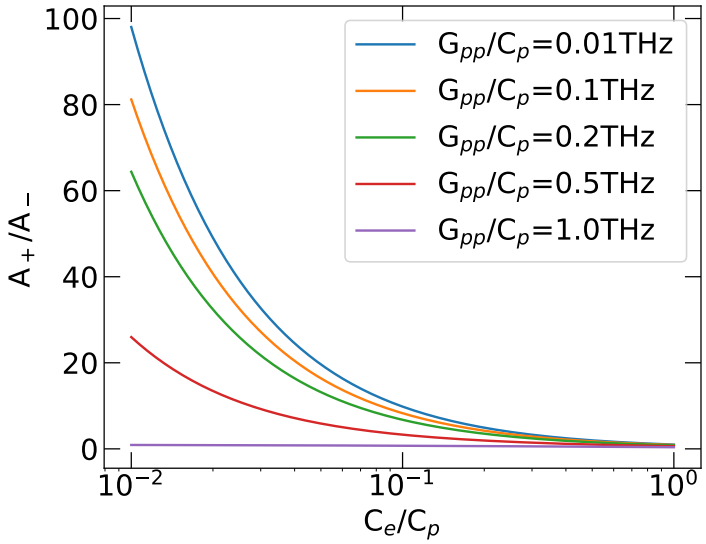

Figure 3.7: Calculated ratio A_+/A_- from TTM as a function of C_e/C_p, for different values of G_{pp}/C_p. All calculated for a fixed value of G_{ep}/C_e=1 THz

This means that for a smaller ratio the second stage of cooling will appear at higher temperatures, therefore increasing the carrier temperatures during the HPB regime and make it last longer. This could be important because it would allow carriers to be hotter and to remain it for longer, which could help their extraction in a device. As the phonon phonon coupling approaches the electron-phonon coupling the two amplitudes tend to be equal. The same happens when the two heat capacities get more similar. This is intuitively correct, because in both these cases the "asymmetry" between the two coupling rates is reduced. Using these results it should be possible to at least give an order of magnitude estimation of the ratio of the two heat capacities.

Thanks to the theoretical framework developed in this chapter it is possible to understand and quantitatively compare the experimental results that will be presented in the following chapters.

Chapter 4

Carrier dynamics and intraband cooling in inorganic Sn perovskites

In this chapter several lead and tin perovskites will be investigated to study how the composition affects the recombination dynamics and the hot carrier cooling. As explained in Chapter 1, harvesting hot carriers would open the possibility of a dramatic increase in solar cell efficiency. For this reason understanding and characterising how this process happens is of major importance. This chapter will focus on finding a promising candidate for photovoltaic (studying Br-substituted $Rb_{0.1}Cs_{0.9}SnI_3$) and on characterising the low fluence (Fröhlich dominated) hot carrier cooling dynamic. In the vast field of perovskite photovoltaics, one of the main obstacles between a possible real-world implementation is the presence of lead in many of the candidates. Lead is notoriously poisonous for humans, so there is a strong interest in researching lead-free compounds. In this context the fully inorganic $CsSnI_3$ (and the partially Rb-substituted $Rb_{0.1}Cs_{0.9}SnI_3$) have shown promising results in very few years of activity.

The first section will introduce Br-substituted $Rb_{0.1}Cs_{0.9}SnI_3$, and the influence of bromine on the photovoltaic properties will be studied. In the second section the hot carrier dynamics of a thin film of $Rb_{0.1}Cs_{0.9}SnI_3$, without any Br substitution, will be studied using optical pump terahertz probe (OPTP). The influence of the bandstructure on this phenomenon will be discussed. Finally the simple Fröhlich model of energy loss developed in section 3.2.3 will be applied to the case of $Rb_{0.1}Cs_{0.9}SnI_3$.

In this chapter I had to include figures presenting experimental and theo-

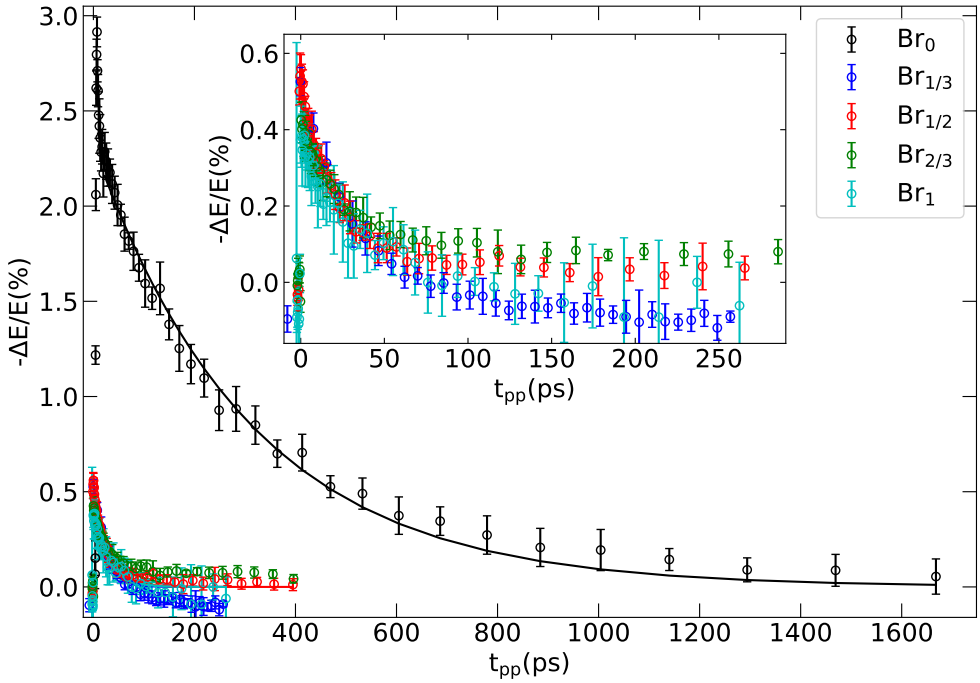

Figure 4.1: Recombination dynamics of Br-containing samples: Br_0 (black), $Br_{1/3}$ (blue), $Br_{1/2}$(red), $Br_{2/3}$(green) and Br_1 (cyan). All these were measured at a carrier density of 1×10^{19}cm^{-3} with a 600 nm pump. The inset shows a detail of samples without the pure $Rb_{0.1}Cs_{0.9}SnI_3$. From the inset is clear that there is not any substantial difference between the various bromine concentrations. All the fits correspond to a single-exponential decay.

retical results not obtained by myself, but necessary to explain and validate the other results. The results not obtained by myself are: the density functional theory (DFT) calculations, which have been performed by S.X. Tao and the PL measurements which have been measured by A. Crocker and E. Griffin, under the supervision of M. Staniforth. The samples were prepared by A. Wijesekara and R.A. Hatton. Section 4.2 has been previously published as M.Monti, *et. al.*, J. Phys. Chem. C, 2018, **122**(36), pp 20669-20675.

4.1 Quality of Br-substituted $CsSnI_3$

One of the major drawbacks of perovskites for solar cells is their susceptibility to degradation under ambient condition[161, 162]. One of the ways people tried to improve this behaviour is via Br-substitution of the halide [163]. This has two main effects: firstly it reduces the sample degradation, second it increases the bandgap[164].

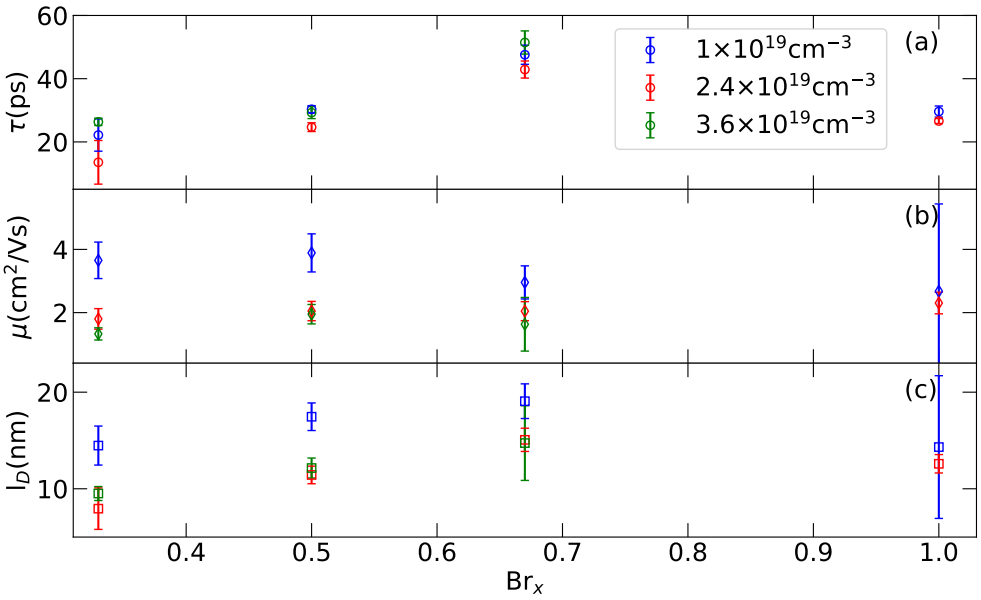

Figure 4.2: This figure reports the recombination time (a), mobility(b) and an estimated diffusion length (c), as a function of Bromine concentration, for three different carrier densities: 1.0×10^{19} (blue), 2.4×10^{19} (red) and $3.6\times10^{19}\text{cm}^{-3}$(green).

In order to investigate the effect of Br substitution on the basic photovoltaic properties, five samples were studied: $Cs_{0.8}Rb_{0.2}Sn(I_{1-x}Br_x)_3$, where x = 0, 1/3, 1/2, 2/3, 1. These samples will be referred from now on as Br_x, with x, correspondingly being 0, 1/3, 1/2, 2/3, 1.

4.1.1 Sample preparation

The Br_x samples were thin films prepared inside a nitrogen-filled glovebox by spin-coating on a quartz substrate, then sealed. The basic materials were mixed together

$Cs_{0.8}Rb_{0.2}Sn(I_{1-x}Br_x)_3$(x)	τ_{Rec}(ps)	$\mu(\text{cm}^2/\text{Vs})$	l_D(nm)
0	311±9	20±3	127±9
1/3	22±5	3.6±0.6	14±2
1/2	30±1.6	3.9±0.6	17±1.4
2/3	48±3	3.0±0.5	19±1.8
1	26±1.7	2.3±0.3	12±1

Table 4.1: In this table an example of the values for recombination time, mobility and diffusion length is reported. All the values correspond to a carrier density of $1.0\times10^{19}\text{cm}^{-3}$, except the sample $Cs_{0.8}Rb_{0.2}Br_3$, where the value at $2.4\times10^{19}\text{cm}^{-3}$ was used.

in the desired molar ratio. To deposit films, a few drops of a particular solution were dropped onto the substrate to cover the entire surface, followed by spinning at 4000rpm for 30 s. The substrate used was z-cut quartz, and samples were then encapsulated with either a top layer of poly(methyl methacrylate) or a second quartz substrate, which was sealed by an epoxy while inside the glovebox. The choice of substrate ensured excellent transparency across the UV, visible and terahertz region. An undoped single crystal of (100)-orientation was used for the measurements on GaAs.

4.1.2 Recombination dynamics

The carrier recombination time and mobility were measured using OPTP and the methodology described in section 2.1. Having the desire to maintain the conditions as similar as possible, the incident fluence was varied in order to have the same number of injected carriers in each sample. This was done for carrier densities 1.0×10^{19}, 2.4×10^{19} and 3.6×10^{19} cm^{-3}, with a 600 nm (2.06 eV) excitation. The recombination times were estimated using single-exponential decays in all cases. For how the carrier densities are computed the reader should refer to section 2.1.4. On top of that, these values were used to estimate the carrier diffusion length. In order to estimate the carrier diffusivity, D, the Einstein relation was used:

$$D = \frac{\mu k_B T_e}{q}, \tag{4.1}$$

where μ is the mobility, k_B is the Boltzmann constant and T_e is the electron plasma temperature. From this, considering the recombination time, τ_{Rec}[134], the diffusion length l_D is:

$$l_D = \sqrt{D\tau_{Rec}} = \sqrt{\frac{\mu k_B T_e}{q}\tau_{Rec}}. \tag{4.2}$$

In Figure 4.1 the recombination dynamics is reported for all the bromine concentrations, including 0% (main panel), and for the Br-containing samples only (inset). A comparison of all samples is also reported in Table 4.1. From this figure it is already clear that Br creates a dramatic difference in performance: $Rb_{0.1}Cs_{0.9}SnI_3$ clearly outperforms the other samples in both recombination time and electric field change (in this case directly proportional to the mobility, being all the curves measured at the same carrier density). In the inset it is possible to notice how all the Br-containing samples show a very similar recombination dynamics and photoinduced change (mobility). To distinguish between these curves, a more throughout study is needed. To do that the mobility and recombination time were extracted

from the recombination dynamics and used to estimate the carrier diffusion length. An example of the data (at N=1×10^{19}cm^{-3}) is reported in Table 4.1. The numbers are quite similar for all the samples with some bromine inside, and the Br_0 dramatically outperforms them with a recombination time of about 311 ps and a mobility that reaches a value of almost 20 cm^2/Vs, while all the Br-containing samples perform no better than 50 ps, and 4 cm^2/Vs. Given the better performances in both recombination time and mobility is no surprise $Rb_{0.1}Cs_{0.9}SnI_3$ outperforms the other compositions even in the carrier diffusion length (calculated from Equation 4.2). The value is estimated to be almost 130 nm in the Br_0 case, reaching the threshold represented by the average film thickness, while all the other compositions struggle to surpass 20 nm, a very low value for a photovoltaic material.

On top of that to check if there is any sort of difference or trend between the samples with incorporated bromine, these are plotted, excluding Br_0, in Figure 4.2. The three panels report the recombination time (a), mobility (b) and carrier diffusion length (c) as a function of Br concentration, with the exception of Br_0. The recombination time seems to increase with bromine concentration from 33% to 67%, while the Br_1 has a lower value. The numbers are consistent between different excitation densities, this suggest the influence of bimolecular and auger recombination processes is negligible at these carrier densities for these samples. The mobility values are all quite consistent with each other, and no visible trend can be observed varying the composition. It appears though, that the mobility obtained from the low carrier density measurement is slightly higher than the other two (at least for the samples with less bromine). This might be caused by a slight degradation caused by the laser pulse or by air slipping through the encapsulation (the experiments were performed from the lowest carrier density to the highest), or perhaps by an induced formation of excitons at higher carrier densities[141]. The diffusion length, which was calculated from τ_{Rec} and μ, carries the characteristics of both quantities: it slightly increases with Br concentration up to 67%, then decreases, and the slight fluence dependence found in the mobility.

From this brief study it was possible to characterise and understand the influence of Br-inclusion on the quantities that control the photovoltaic performance. Br influence appears to have a dramatically negative effect by lowering both the mobility and the recombination time. For this reason, in the remainder of the chapter, the composition with no bromine, *i.e.* $Rb_{0.1}Cs_{0.9}SnI_3$, will be investigated. However, the influence of bromine on the HCC dynamics of an organic-inorganic perovskite will be investigated in section 5.5.

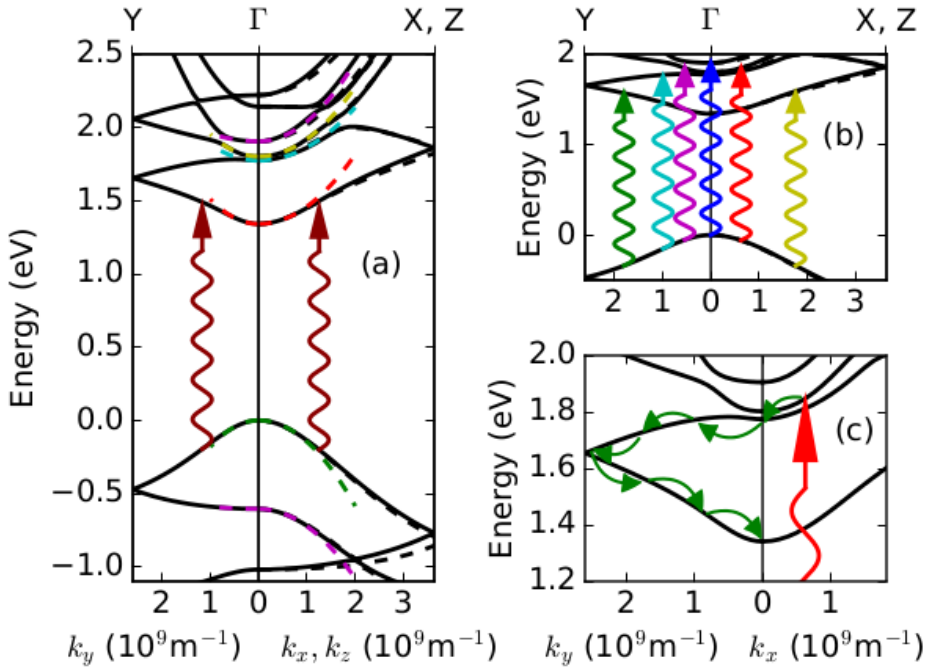

Figure 4.3: Bandstructure of $CsSnI_3$ calculated from the DFT 1/2 method. (a) Band dispersion along the y-direction (left, solid black line) and along x (right solid black lines) and z (right dashed black lines). Parabolic fits to the local minima are shown by the dashed coloured lines. The red lines show an interband absorption transition at 750 nm (1.65 eV). (b) Possible interband transitions at a pump wavelength of 650 nm (1.91 eV). (c) Possible relaxation path (green arrows) within the conduction bands after a 650 nm excitation into CB3. Reproduced from Monti *et al.* [48], calculation performed by S.X. Tao.

4.2 Intraband relaxation in $CsSnI_3$

In this section the hot carrier relaxation in $Rb_{0.1}Cs_{0.9}SnI_3$ is presented and discussed. The reason why $CsSnI_3$, a full inorganic tin perovskite, was chosen as a first case study, is because it represents a cleaner system to investigate. This is true for two reasons: the inorganic cation excludes the effects of organic cation reorientation[92], and tin perovskites have a lower Auger rate than their lead counterparts[135]. In lead perovskites the Auger effect can have a substantial influence on carrier cooling dynamics [105], and it becomes an additional phenomenon that has to be taken into account. Partial Rb substitution was chosen because it improves PV performance[165] without affecting the bandstructure. One of the main characteristics of $CsSnI_3$ is the orthorhombic structure at room temperature (B-γ

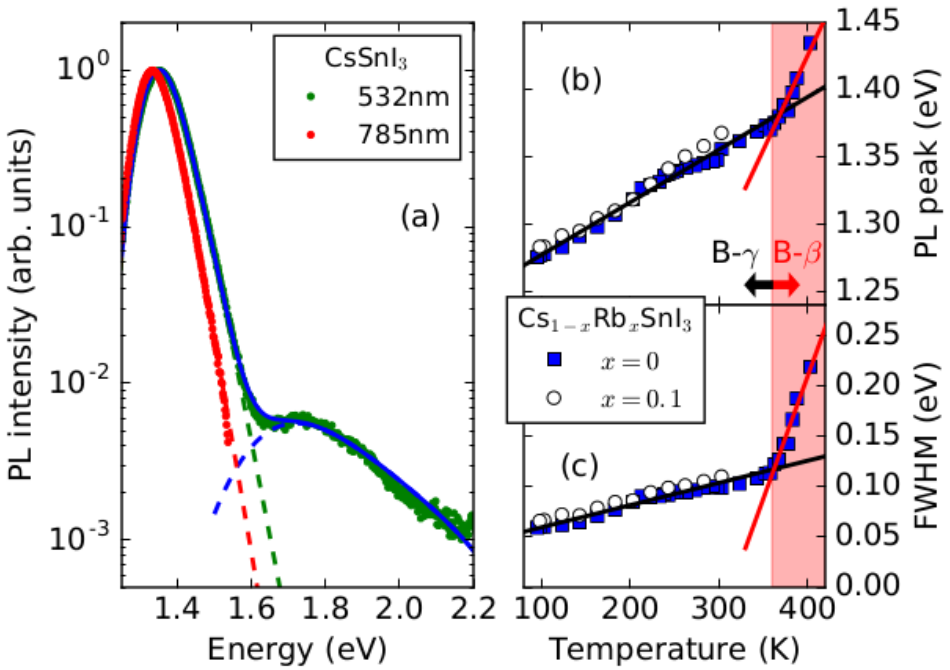

Figure 4.4: Photoluminescence of $CsSnI_3$ thin film encapsulated in glass. (a) PL intensity for $CsSnI_3$ at different pump wavelengths: 532 nm (2.33 eV, green dots) and 785 nm (1.6 eV, red dots). Dashed lines are fit performed as described in the text. (b) PL peak for x=0 (squares) and x=0.1 (circles). Straight lines are fits to the x=0 data for the B-γ phase (black line below 360K) and the B-β phase (red line, 360-405K). (c) FWHM of Pl spectrum, labelled as in (b). Reproduced from Monti *et al.* [48], measurements performed by A. Crocker, E. Griffin and M. Staniforth.

phase), as opposite to the slightly tetragonal structure of MAPI [27]. This characteristic makes the bandstructure more anisotropic; this, along with the readily accessible multiple bands, ought to have an influence on the carrier relaxation. This is investigated in the remain of the section. The samples used for this section are prepared in the same way as in the previous section.

4.2.1 Anisotropic multi-band structure

To identify the relevant excitation wavelengths the bandstructure of pure $CsSnI_3$ was calculated using the DFT 1/2 method. The result of this calculations for the orthorombic B-β phase are reported in Figure 4.3. As previously reported [166], the VB is a result of Sn 5s and I 5p orbitals, while the CB are result of Sn 5p. The similarities between x and z direction yield a comparable dispersion for X and Z

directions, while the dispersion toward Y is significantly different and results in a lower energy at the BZ boundary. This is because of b≫ a, c, where a,b, and c are the lattice parameters. The value obtained for the band gap is consistent with the experimentally measured value. The addition of x=0.25 Rb slightly changed the band gap but didn't affect the overall structure [48].

In order to confirm these theoretical predictions the PL intensity spectrum was measured. PL represents a good tool to probe the energy distribution of electron and holes during recombination. The PL spectrum (at 785 nm excitation) reported in Figure 4.4 shows a strong peak at the band gap (in good agreement with the DFT predictions). The things become more interesting if the sample is excited with 532 nm; in this case, alongside with the band gap excitation, a second PL peak at higher energy can be observed. This second peak is consistent with a interband transition between the second CB and the first VB, according to the DFT calculations.

4.2.2 Relaxation times measured by OPTP

Since the PL results indicate that the carriers are still hot when they undergo radiative recombination, a nonthermal population of carriers is still present while carriers recombine. To provide experimental insights into the intraband dynamics, OPTP was performed in a wide range of wavelengths across the peak of the solar spectrum. The reason why OPTP can be used to track carrier intraband relaxation is extensively explained in section 2.1.5. The absorption depth throughout the experiment was comparable to the film thickness, so physical phenomena that complicate the dynamics, such as carrier diffusion and photon recycling[167], which also happen on a much longer timescale, can be ignored. The recombination dynamics at the fluence used was observed to be monoexponential with a lifetime of about 300 ps.

In Figure 4.5 the onset of photoconductivity is reported for both $Rb_{0.1}Cs_{0.9}SnI_3$ (b, right) and GaAs (a, left) for various excitation wavelengths. The time it takes to reach the maximum increases with the excitation energy for both samples; although the change in GaAs is more pronounced. For $Rb_{0.1}Cs_{0.9}SnI_3$ the variations is small, but for GaAs the total time needed to reach the maximum of photoconductivity changes from 300 fs at 780 nm up to 5 ps at 600 nm.

To quantitatively compare the photoconductivity dynamics, fit results, performed following the procedure described in section 2.1.5, are presented in Figure 4.6. The fit yielded about 150 fs for the rise time of GaAs (blue squares in Figure 4.6) at the longest excitation wavelength. This time increases marginally between the average of 150 fs for $\lambda > 750$ nm up to about 300 fs at 680 nm, due to the extra

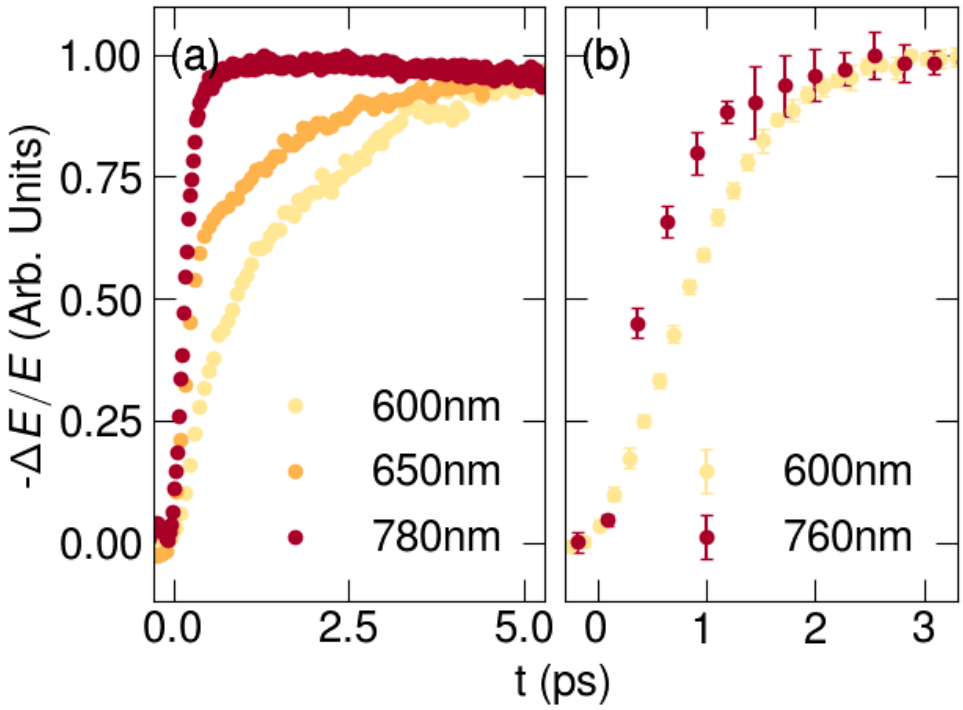

Figure 4.5: OPTP onset for (a) GaAs, (b) $Rb_{0.1}Cs_{0.9}SnI_3$. It is clear how for GaAs the time needed by the photoconductivity to reach its maximum increases from about 1 ps at 800 nm to 5 ps at 600 nm. In contrast the photoconductivity of $Rb_{0.1}Cs_{0.9}SnI_3$ takes about 3 ps to reach its maximum at all wavelengths. Reproduced from Monti *et al.* [48]

time required by the carriers to cool down to the Γ point. Increasing the energy even further ($\lambda < 650$ nm) the time increases more dramatically up to over 1.5 ps as electrons are injected at an energy high enough to undergo intervalley transfer to the L- and X-valleys, at energy higher than 1.71 and 1.9 eV respectively. The photoconductivity dynamics onset of $Rb_{0.1}Cs_{0.9}SnI_3$, reported in Figure 4.5, show similar rise times to GaAs, but with a less substantial wavelength dependence. In $Rb_{0.1}Cs_{0.9}SnI_3$ the electron and hole masses are comparable in CB and VB, so the total contribution of the dynamics of the photoconductivity is due to both carriers population dynamics. The rise time was observed to be independent of the pump fluence in the range 20-200 $\mu J/cm^2$ and for different Rb concentration.

These differences of $Rb_{0.1}Cs_{0.9}SnI_3$, photoconductivity rise dynamic are confirmed by the fit outcome (reported in Figure 4.6, red circles). At lower excess energies (longer wavelengths) the photoconductivity rises to a maximum within 1 ps, with an average τ=0.45±0.08 ps over the range between 760 and 700 nm. For

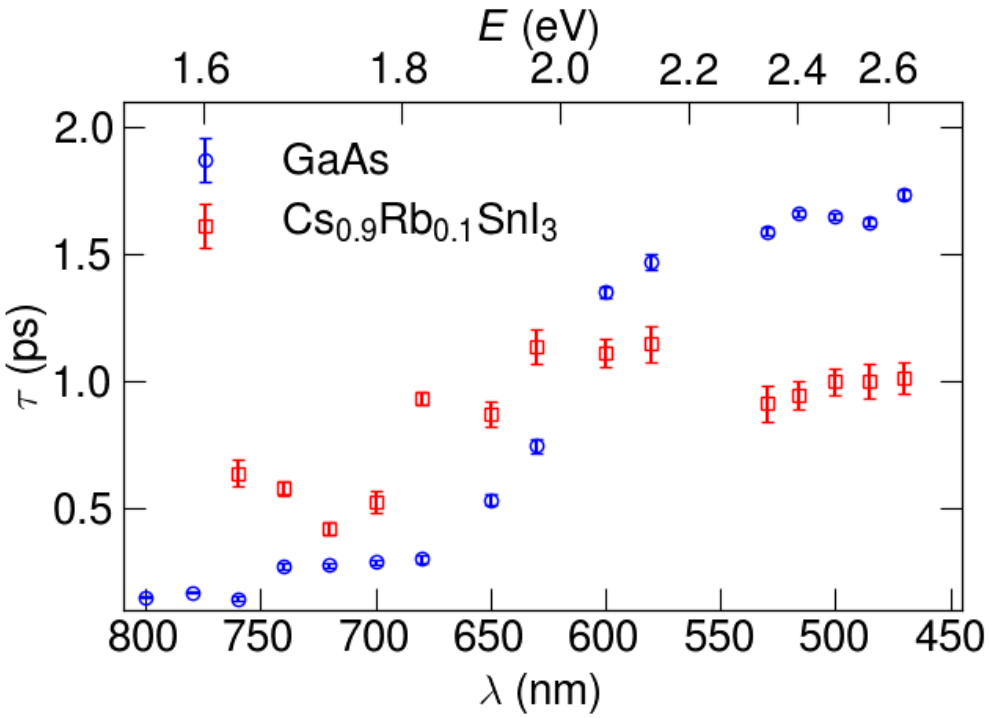

Figure 4.6: Result from fit comparing (a) GaAs (blue circles) with $Rb_{0.1}Cs_{0.9}SnI_3$ (red squares). The tin-based perovskite shows an energy relaxation time which is comparable to the GaAs one and with a complex energy dependence.Reproduced from Monti *et al.* [48]

this range of energies excitation is allowed from VB1 to CB1 only, as clear from Figure 4.3. With a pump of 650 nm (1.91 eV) carriers can be excited from VB1 to a high mass state in CB1, but also into CB2, CB3 and CB4. This shows up in a slower average rise time of τ=0.9±0.3 ps. At energies higher than 1.95 eV even the transition from VB2 to CB1 becomes allowed and the rise time settles around 1 ps. While this is faster than for GaAs, $CsSnI_3$ does not have side valleys, and hence a different mechanism is at work. In order to better understand the low-injected energy part an attempt will be made to model the energy relaxation time.

4.2.3 Model of the energy relaxation time

In polar semiconductors such as GaAs or metal halide perovskites, the dominant mechanism of intraband cooling is the Fröhlich interaction[146, 147]. Therefore in the following discussion the energy loss time caused by electron-LO phonon interaction calculated in section 3.2.3 will be used in an attempt to describe the observed

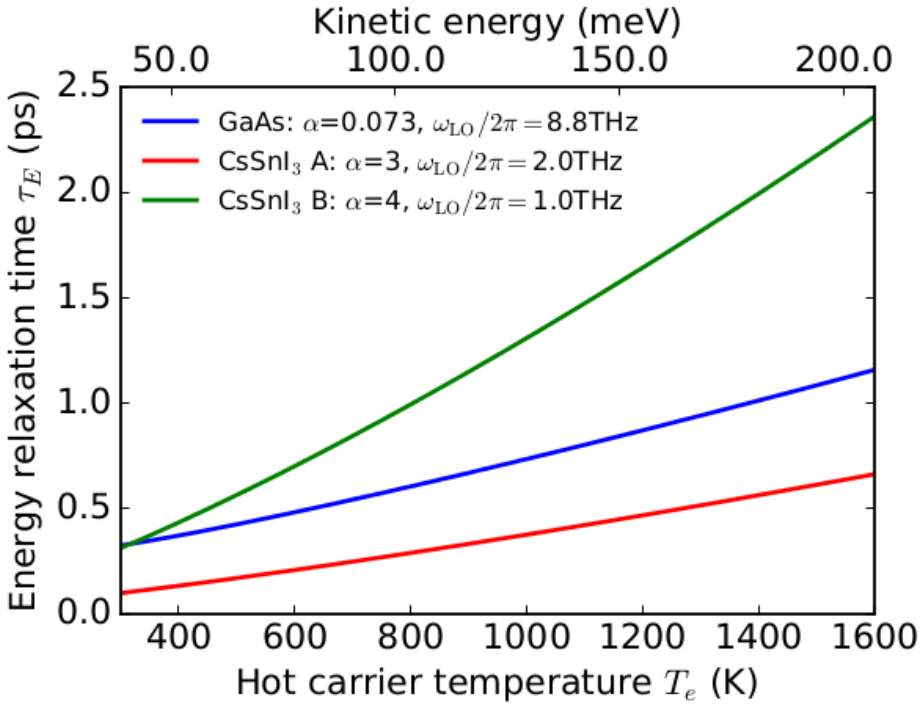

Figure 4.7: Energy relaxation time τ_E calculated for hot carriers at a lattice temperature T=300 K and for parameters representative of GaAs (blue curve) and $CsSnI_3$ (green and red curves). Reproduced from Monti *et al.* [48]

results in both GaAs and $Rb_{0.1}Cs_{0.9}SnI_3$. The energy loss time is expressed as follows:

$$\tau = \frac{3\pi^{1/2}\hbar}{4\alpha k_B} \frac{\sqrt{T_e}\,(T_e - T)}{\Theta^{5/2} K_0\,(\Theta/2T_e)} \frac{\sinh\,(\Theta/2T)}{\sinh\,[(T_e - T)]\,\Theta/2T_e T}, \tag{4.3}$$

where Θ is defined as $k_B\Theta = \hbar\omega_{LO}$. T_e is the hot electron temperature, T the lattice temperature, K_0 the modified Bessel function of the second kind and α is the Fröhlich constant, already defined in section 3.2.3. Using Equation 4.3 it should be possible to calculate the energy relaxation time for GaAs and $CsSnI_3$ and compare it to the experimental values obtained with OPTP. As already explained, the values used for GaAs are relatively well-known. On the contrary there are very few accurate experimental data on $CsSnI_3$, especially on dielectric constants and phonon frequencies. This is caused by the large p-type doping typically found for B-γ $CsSnI_3$, which has hindered the experimental determination of the phonon mode frequencies from Raman and FTIR and the determination of ε_s. To obviate this lack of data, theoretical values from first-principles calculations were used. From different works[168–170] two parameters sets have been extracted: $\alpha \simeq 3.0$ for

$m^* = 0.25m_e$ and $\omega_{LO}/2\pi = 2$THz (parameter set A), or $\alpha \simeq 4$ for $m^* = 0.25m_e$ and $\omega_{LO}/2\pi = 1$THz (parameter set B). The energy relaxation rate as a function of the hot carrier temperature, calculated for $CsSnI_3$ and GaAs, are reported in Figure 4.7. On top of the carrier temperature, the energy, calculated via $\varepsilon_k = \frac{3}{2}k_B T_e$ is also reported. The above formalism, which was derived for a single, spherical band, can only be applied for low energy values, where multiple bands (for $CsSnI_3$) or multiple valleys (for GaAs) can be ignored. The calculated value for GaAs at low energy is around 300 fs, which can be compared with the experimental value at low excitation energy of 155 fs. The electron-LO phonon rate thus makes up for half the total cooling rate. The remainder is probably accounted by the electron-acoustic phonon scattering as suggested by recent first principles treatments of electron cooling in GaAs [171]. This is in stark contrast to the calculations reported in section 3.2.3. This leads to the conclusion that the simple model of phonon scattering displayed here is incapable of correctly describing the phenomenon, even in a simple system like GaAs. For this reason the description provided can be considered semi-quantitative.

From Figure 4.7 it can be seen as the two parameter sets give widely different values for the cooling rate. In detail, parameter set B seems to widely overestimate the cooling time by estimating a τ=1.5 ps at 150 meV of excess energy (corresponding to 760 nm pump) against an experimental value of 0.55 ps. The outcome of parameter set A seems more consistent, by providing an estimated value of 0.45 ps for the cooling time. This seems a reasonable agreement given the uncertainties in α and ω_{LO} and the simplified assumptions of the model.

4.3 Concluding remarks

This chapter first investigated the influence of Br substitution on the photovoltaic potential of $Rb_{0.1}Cs_{0.9}SnI_3$, by calculation of mobility and recombination time and estimating the carrier diffusion length. Br was found to be detrimental for the photovoltaic performance.

Afterwards, the chapter investigated the Fröhlich-dominated cooling dynamics of the inorganic perovskite semiconductor $Rb_{0.1}Cs_{0.9}SnI_3$. The energy relaxation times were found to be longer than the inorganic semiconductor GaAs in the range where intervalley scattering is not dominant. An abrupt change was observed in the value of the energy relaxation time in the perovskite sample at an excess energy compatible with injection into a second interband transition, the longer measured time was linked to the anisotropy observed in the bandstructure. Finally a model was developed based on a simple Fröhlich interaction energy loss mechanism.

The good semi-quantitative agreement between the intraband energy relaxation time in the Fröhlich description and the experimental τ suggests that the electron-phonon interaction may control the energetic relaxation of hot carriers in metal halide perovskites. Despite the lower LO phonon energy in the halide perovskites than in GaAs, which would increase the energy relaxation time by Equation 4.3, the electron cooling times can be comparable as a result of an enhanced electron-phonon interaction strength (α). It is critical to note that the calculated results are valid only in the low-excess energy limit, where bands can be approximated as parabolic, and in the single band case only. More realistic models of energy relaxation need to include acoustic phonon scattering, excitonic effects, the inherent anisotropy of the bandstructure, the phonon dispersion, and α.

Chapter 5

Influence of composition on hot carrier cooling in triple-cation metal halide perovskites

In this chapter the objective will be to tackle one of the questions posed at the beginning of this thesis: how does changing the Sn/Pb ratio affect the hot carrier cooling (HCC) time in metal halide perovskites (MHPs)? To answer this question, the approach consisted in measuring the hot carrier dynamics of a set of five mixed lead-tin perovskite semiconductors.

The samples chosen for this study are a set of triple-cation mixed lead-tin iodine compounds: $Cs_{0.05}(FA_{0.83}MA_{0.17})_{0.95}Pb_xSn_{1-x}I_3$, with x=0, 0.25, 0.5, 0.75, 1. The choice of a triple cation perovskite was made in order to improve the sample response thanks to their reasonable mobility, enhance their stability with time and, finally, make the findings directly relevant to the current state-of-the-art for perovskite solar cell materials[172]. No significant differences have been found between the two most common organic cations (MA, FA) for what regards the HCC dynamics[86] and a small added cation substitution is known to not change the bandstructure significantly[48].

The study reported in this chapter focuses on the high fluence regime where effects such as the hot phonon bottleneck (HPB) are known to occur[86, 88]. A final problem, simple, although crucial, is also addressed: how do transient absorption spectroscopy (TAS) and optical pump terahertz probe (OPTP) spectroscopy compare? Traditionally, the way the HCC dynamic has been measured is through the broadening of the ground state bleach in transient absorption (see section 2.2.3 for a detailed description), or, alternatively, through the broadening of time-resolved

PL measurements[99]. Very recently, however, different research works (including this thesis's Chapter 4, which formed the basis of an article [48]) have started using terahertz spectroscopy to investigate the same process[102, 106, 107]. However, in these experiments, the long cooling times observed with the optical techniques are absent. This sparks the question whether these techniques are equivalent (it can be anticipated that they are not) and if not, how do the numbers compare between them.

The chapter starts with basic sample characteristics from absorbance and photoluminescence spectroscopy, which were used to determine the band gap and absorbed number of carriers used in the following sections, as well as to assess the sample quality. The second section presents the results obtained through OPTP spectroscopy: mobility and hot carrier cooling time, the latter following the same approach as section 4.2.2. The third section uses the three temperature model (TTM), introduced in section 3.2, to quantitatively compare the different samples and understand their different cooling dynamic. Finally, a sample with full lead and added Br is introduced and briefly studied as a preliminary investigation of the influence of Br substitution on hot carriers.

The PL and absorbance data presented in this chapter were acquired by E. Butler-Caddle. The samples were prepared by K.D.G.I. Jayawardena, R.M.I. Bandara and S.R.P. Silva following a procedure outlined in Bandara *et al.* [51].

5.1 Characterisation

Photoluminescence (PL) and absorbance spectra are important basic quantities which provide useful information on a material emission and absorption, which are of great importance to understand the potential those materials might have in the PV context. In this work, absorption and PL are relevant in allowing the correct number of absorbed carriers and the band gap to be measured, which in turns allows for accurate measurements of the mobility and of the excess energy. In this work the PL linewidth and Stokes shift will also be presented and compared with previous reports of similar materials in order to assess the sample quality.

5.1.1 Photoluminescence and Absorption

To extract the energy gap from the PL spectrum, the peak was fitted with a Gaussian curve. For the absorption, instead of the most commonly used Tauc method[173, 174], which doesn't take into account the exciton contribution (difficult to estimate for room temperature absorption data) the method outlined in Parrott *et al.* [175]

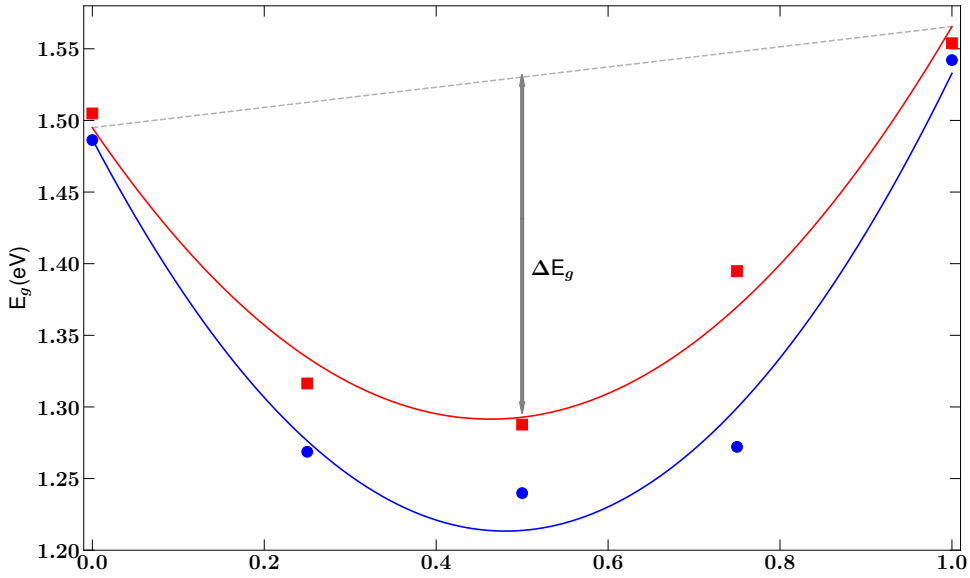

Figure 5.1: Band gap values, versus lead concentration. They are measured from absorbance (red squares) and PL (blue circles). The continuous lines are fits following Equation 5.1. The dotted line represents the gap change in absence of bowing. The grey arrow is a visual representation of the definition of ΔE_g. Both band gap data sets show a strong bowing, with a minimum at 50%.

was applied: the band gap was assumed to correspond to the energy of the maximum gradient of the absorption coefficient.

5.1.2 Energy gaps and Stokes shift

The obtained band gap values, from both PL and absorbance, are reported in Table 5.1 and plotted in Figure 5.1 (a) in blue and red respectively. From the figure, a strong bowing effect is evident in both data sets as the 50-50 alloy has a much

Pb_x	$E_{g,PL}$ (eV)	$E_{g,A}$ (eV)	ΔE_S(meV)	FWHM(meV)
0	1.4863±0.0008	1.50	19	129
0.25	1.2687±0.0002	1.32	48	141
0.5	1.2399±0.0006	1.29	48	107
0.75	1.2721±0.0005	1.39	123	136
1	1.5421±0.0003	1.55	18	88

Table 5.1: Here are reported the values obtained for the band gap for both PL and absorbance, as well as the Stokes shift and the PL linewidth, for the various compositions.

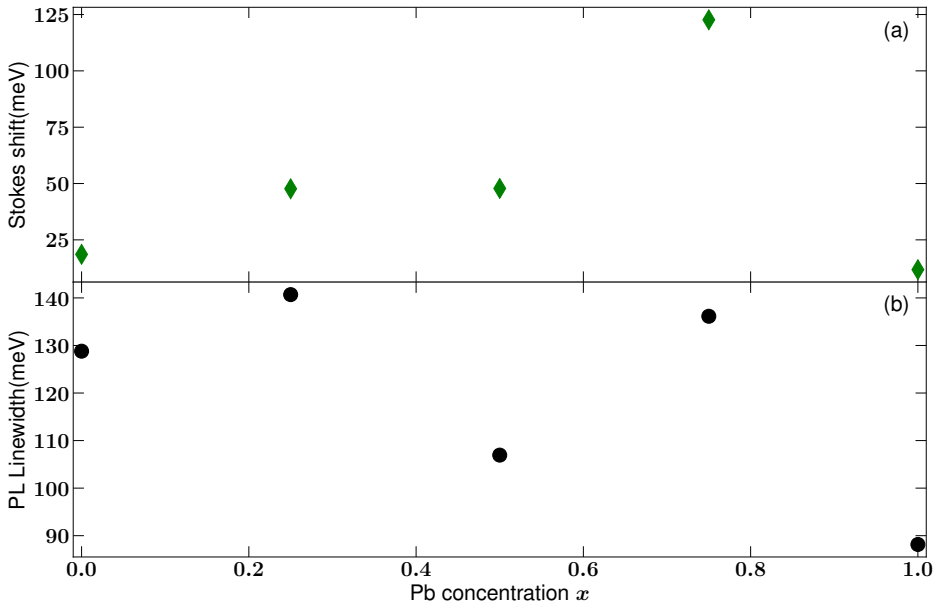

Figure 5.2: On the top (a) the Stokes shift (defined in Equation 5.2) is plotted versus the concentration of lead. The shift is relatively small for the full Sn then it increases significantly, up to $Pb_{0.75}$, which more than doubles any other value, after which drops to a minimum for Pb_1. On the bottom (b) the PL linewidth, measured as FWHM.

lower band gap than the unalloyed compounds. Some degree of bowing is expected for most semiconductor alloys[176], however the reason why such a strong effect happens in MHPs is still under debate[177–179]. To quantify the strength of the bowing one can rely on the difference between the hypothetical band gap line in absence of the effect and the actual band gap of the 50-50 alloy, ΔE_g, which is visually represented in Figure 5.1. This value can be shown to be $\Delta E_g = b/4$, where b is the bowing parameter, defined as[180]:

$$E_g(x) = E_{g,1}x + E_{g,2}(1-x) - bx(1-x), \tag{5.1}$$

where $E_{g,i}$ are the band gaps of the unalloyed compounds and x is the alloy composition (in this case the Pb fraction will be considered). For $b = 0$ Equation 5.1 becomes the well-known Vegard's law[176, 181]. Therefore, to obtain an estimation of the bowing parameter, Equation 5.1 was used to fit the values reported in Figure 5.1, where the fit outcome corresponds to the continuous lines. The values obtained for the b parameter are: $b = 0.95 \pm 0.10$ eV for the absorbance data and $b = 1.20 \pm 0.12$ eV for the PL data.

Alloying the metal site composition is known to produce some degree of bowing in metal-halide perovskites[177], and, particularly, a previous study on $FAPb_xSn_{1-x}I_3$ had shown a significant gap bowing effect, with bowing parameter $b = 0.8$ at room temperature[175]. This bowing effect seems to be absent when the A-site cation[182] or the halide[163] are alloyed. Here the different A-site cation may account for the larger b as the crystal structure, in particular the metal-halide bond lengths and angles, will be subtly different.

From the different band gaps obtained from PL and absorption it is possible to calculate the Stokes shift as the difference between the absorption gap and the PL gap:

$$\Delta E_S = E_{g,A} - E_{g,PL}. \tag{5.2}$$

The Stokes shift is a known phenomenon that happens in semiconductors: it consist in a difference between the absorption and emission energies[4]. Generally when semiconductors absorb photons at the absorption edge, they re-emit those photons at a lower energy. The energy difference originates from vibrational or thermal relaxation losses that happen after excitation. A possible cause is the presence of a many sub-bandgap state originated from a very disordered material. Anti-Stokes shift (emission at higher energy than absorption) is also possible, but it is not common. The values obtained are reported in Table 5.1 and plotted in Figure 5.2 (a). When increasing the Pb concentration, the Stokes shift increases, up to the maximum value of $Pb_{0.75}$ of over 100 meV before the full lead value drops back to a value similar to the full tin. This behaviour is consistent with what has been previously observed in a similar compound[175]. Finally, in Figure 5.2 (b) the PL linewidth is reported. The linewidth was estimated as the full width half maximum (FWHM) of the PL peak. It is readily observed that the only composition to have a spectrum narrower than 100 meV is the x=1.0: all the other samples show values higher than this threshold. This is related to the better film quality of the full lead compound. These values are consistent with previous studies on MHPs. Overall, the PL and absorption results demonstrate the successful formation of perovskite alloys with controllable Pb/Sn ratio.

5.2 Cooling times and mobility measured with optical pump-terahertz probe spectroscopy

As already explained in Chapters 2 and 4, OPTP is a valuable tool to study carrier recombination dynamics and mobility[130, 134, 136]. In Chapter 4 the possible

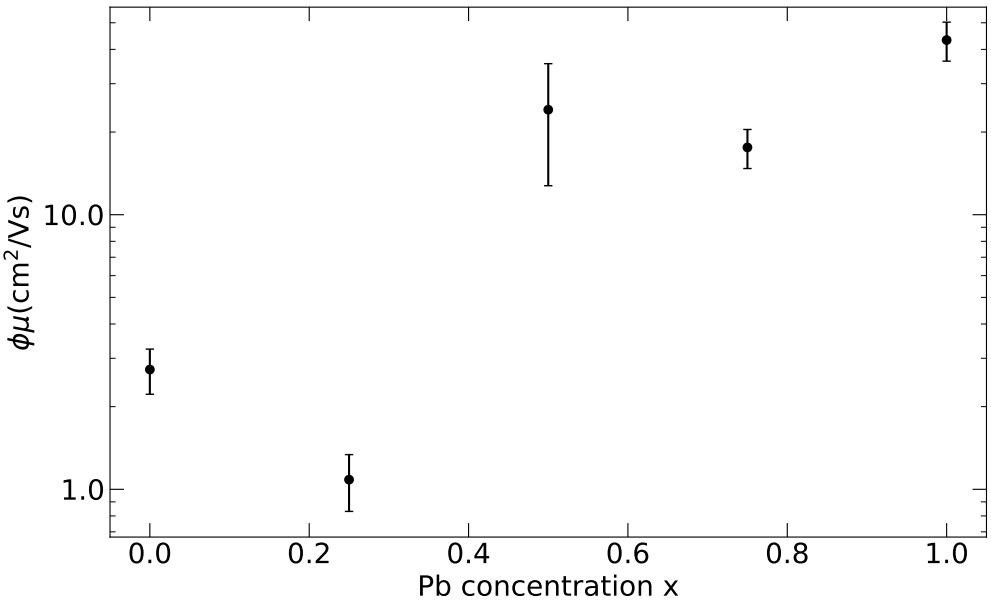

Figure 5.3: $\phi\mu$ values are reported versus lead concentration. The mobility has a minimum for 25% Sn, and shows similar values for samples with $x \geq 0.5$.

application of the technique to study hot carrier relaxation was introduced and used to study HCC in $CsSnI_3$. In this section the aim is to report both the mobility and the cooling time for different lead and tin concentrations.

5.2.1 Mobility

Mobility is an important quantity for the characterization of photovoltaic materials, as the carriers ought to be able to travel to the extraction layer in order to produce a current. Using terahertz spectroscopy, the product of the total mobility, μ (sum of electron and hole mobility), and the yield of free charges, ϕ, can be estimated using the standard method outlined in Chapter 2 (see also, for example, Milot *et al.* [136]). The mobility of the five tin-lead samples is reported in Figure 5.3. For samples with $x \geq 0.5$ the mobility is relatively high ($\phi\mu > 20\,\mathrm{cm}^2/\mathrm{Vs}$) in comparison to $x < 0.5$, where $\phi\mu < 4\,\mathrm{cm}^2/\mathrm{Vs}$. Broadly speaking, these values are consistent with accepted values for perovskite semiconductors[30] The mobility is $\mu = e(\tau_e/m_e^* + \tau_h/m_h^*)$, where the momentum scattering rates, $1/\tau_{e,h}$ for electrons and holes respectively, have additive contributions from different scattering mechanisms. These include inelastic mechanisms such as carrier-LO phonon scattering and carrier-acoustic phonon scattering, and elastic process like carrier-impurity scattering, interface roughness scattering and carrier-carrier scattering. Thus the large variation in $\phi\mu$ with x may in part be due to variations in extrinsic contributions to

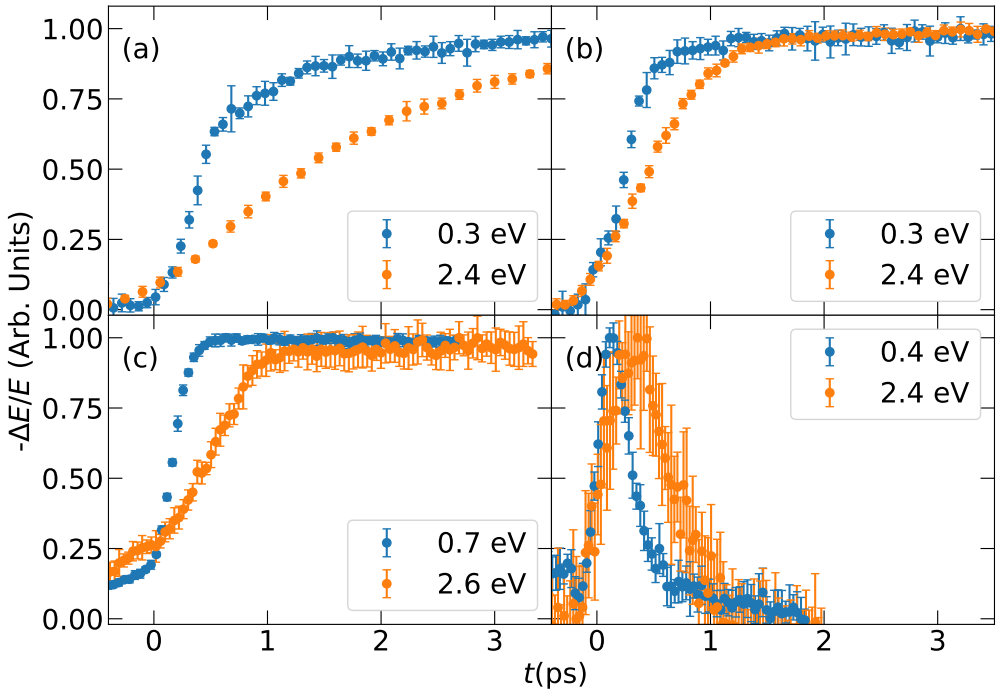

Figure 5.4: Here the onset of photoconductivity (expressed as a relative change in the electric field as extensively explained in Chapter 2) are reported for 4 samples. These are GaAs (a), 100%Pb (b), 50%Pb (c), and 0%Pb (d). For each sample data for two different excess energies are reported (respectively "low" (blue) and "high" (orange)). All samples show differences between the two excitation energies.

the mobility, such as interface roughness scattering and carrier-impurity scattering, which will depend on the grain size, crystallinity, and defect concentration. These extrinsic contributions are elastic and therefore do not influence the cooling time τ, which is controlled by inelastic LO-phonon and acoustic phonon scattering, both intrinsic to a given material. As evident from the order of magnitude change in $\phi\mu$ with x, $\phi\mu$ is highly sensitive to the exact film morphology and quality. This behaviour is consistent with previous studies on perovskite compositions[183].

5.2.2 Carrier cooling

As already extensively discussed in Chapter 2 and Chapter 4, the rise in the photoconductivity onset in OPTP can be used to track the carrier intraband cooling. Following this approach, the rise in the relative change of the transmitted field was measured for the five samples and GaAs and is reported, for $x = 1$, 0.5, 0 and GaAs, for two excess energies, in Figure 5.4. The curves for low and high excess energies are shown. As previously reported [48], GaAs (a) is relatively quick (few

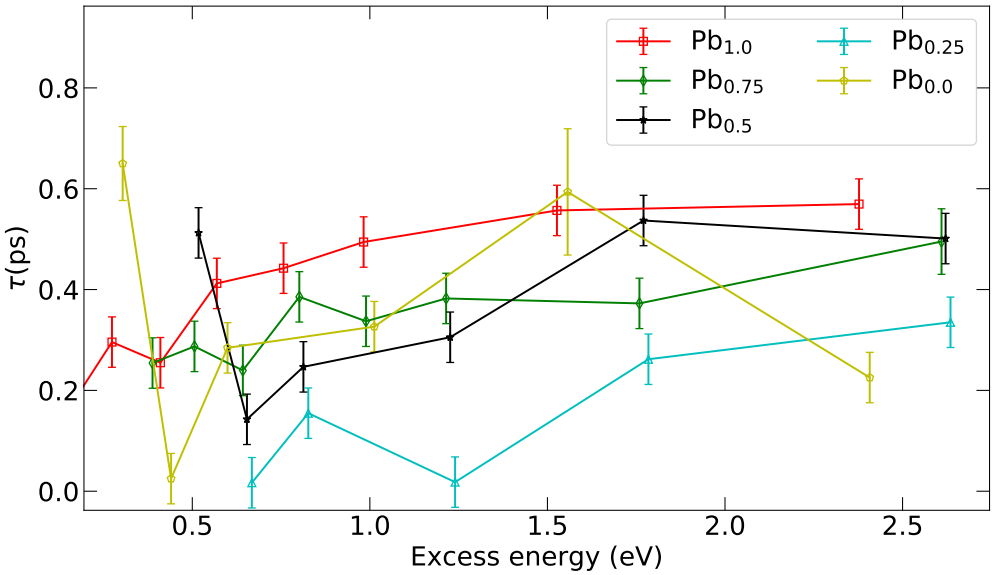

Figure 5.5: In this plot the carrier cooling times for the different samples are reported as a function of excess energy. The value seem to get systematically longer at higher energies, with the possible exception of Pb_0, where values are more scattered around, but they are also intrinsically more noisy given the low signal to noise and the fast transient that follows the rise. The lines are only a guide to the eye.

hundreds of fs) to reach the maximum at low excess energy, while at high excess energy the dynamic becomes substantially slower due to intervalley scattering. The three concentrations, 100%, 50%, 0% Pb ((b), (c), (d) respectively) reported are all much faster than GaAs, at all excess energies. The full Sn sample had a very quick transient recombination dynamic, probably caused by a high number of defects and low film quality. The rises of the samples with x=0, 0.25 have been fitted with a three level model, as described in Chapter 2. In the case of GaAs and x = 1, 0.75, 0.5 the simplified model with long recombination was assumed.

The fit outcome is reported in Figure 5.5, which shows that the HCC time gets significantly longer at higher excess energies. However, all times are well below the 1 ps cooling times reported for $CsSnI_3$ in Chapter 4. Moreover, the sample with x=1 is consistently the slowest (or one of the slowest) of the group at each excess energy, at the same time the x = 0.25 is consistently the fastest. In Figure 5.5, as well as in Figure 5.6, the error bars were estimated as the error provided by the fitting routine in Python; in case the value was smaller than the pump beam duration of 50 fs the uncertainty was rounded up to that value. To further study the concentration dependence, the cooling time as a function of the composition for similar excess energies is plotted in Figure 5.6. The observed times are consistent with previously

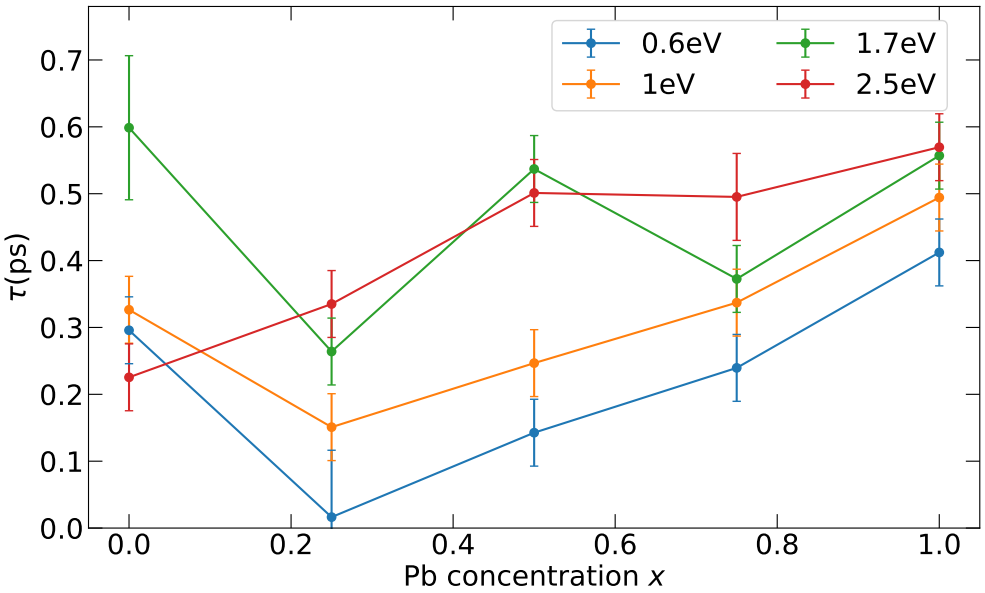

Figure 5.6: The figure reports the hot carrier cooling time as a function of concentration for few given values of excess energies. The lines are only a guide to the eye. The values at low excess energy show a systematic trend: as soon as some lead is introduced in the system the value drops and then slowly rises with the lead concentration, till it reaches a maximum at Pb_1. The high excess energy value, 1.7 eV, shows instead a much less clear pattern: the $Pb_{0.25}$ is still the minimum value, but the other samples have a less clear hierarchical structure.

measured organic-inorganic lead perovskites with similar techniques[100, 102, 106] and, as observed before, increase with increasing excess energy. Two regimes can be identified at low or high excess energy. For the low excess energy case the cooling times are longer for the full lead sample, and steadily shorten with increasing Sn concentration, up to a minimum, which happens at 75% Sn, before rising again for the full Sn sample. This is consistent with similar studies performed with different techniques[115]. In the 0.6 eV excess energy case the value measured for x=0.25 is effectively shorter than our time resolution, so it can only be concluded the value is around 100 fs or shorter. In the high excess energy regime the values are more scattered and no obvious trend is identified. This could be caused by a complicated bandstructure, as reported before for $CsSnI_3$ (Chapter 4), although without precise bandstructure calculations for these specific sample compositions it is difficult to precisely quantify this influence.

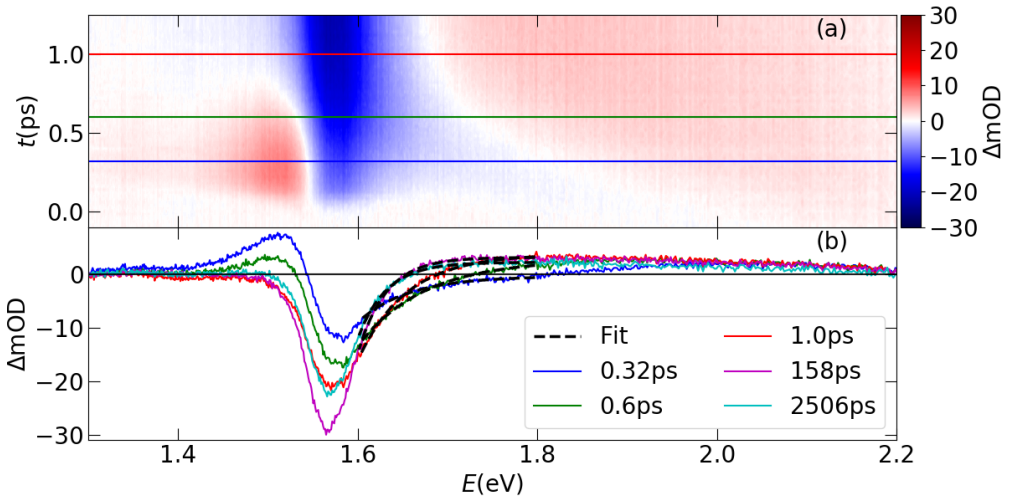

Figure 5.7: In panel (a) a contour plot of the transient change in absorption is reported for the full lead sample at 70 μJ/cm^2. The x axis is the probe energy (in eV) and the y axis is pump-probe time delay, in ps. The absorption is reported only for the first 1.2 ps for clarity. Three prominent features are observed in the spectrum: a quick and narrow photoinduced absorption region at the band gap, a strong absorption bleach just above the band gap and a broad photoinduced absorption at higher energies. The origin of these features is discussed in more detail in the text. In panel (b) a few transient absorption spectra are reported at different pump-probe delays. The black dashed lines correspond to fits used to extract the carrier temperature. Part of these spectra correspond to time slices in panel (b) and are indicated there with matching colours.

5.3 Transient absorption spectroscopy

A 400 nm pump (3.1 eV), white light probe spectroscopy technique was used to extract the carrier temperature dynamic in the different samples. The methodology for the analysis of the TAS data is extensively reported in Chapter 2. The pump energy corresponds to excess energies in the 1.6-1.8 eV range (depending on the alloy concentration, due to gap bowing), and a wide range of fluences (40-400 μJ/cm^2). The high fluence and high excess energy are required to access the hot phonon regime[99]. An example of TAS spectra, measured on x=1, is reported in Figure 5.7 (a) where a contour plot of the change in absorption is reported: the x-axis is the probe energy, while the y-axis is the pump-probe time delay t. The colour represents the intensity of the pump-induced change in absorption expressed in mOD. Only the first 1.2 ps are reported for clarity. The coloured lines represent slices at different pump-probe delays, as reported in Figure 5.7 (b).

Shortly after $t = 0$, three prominent features appear: a strong bleach at

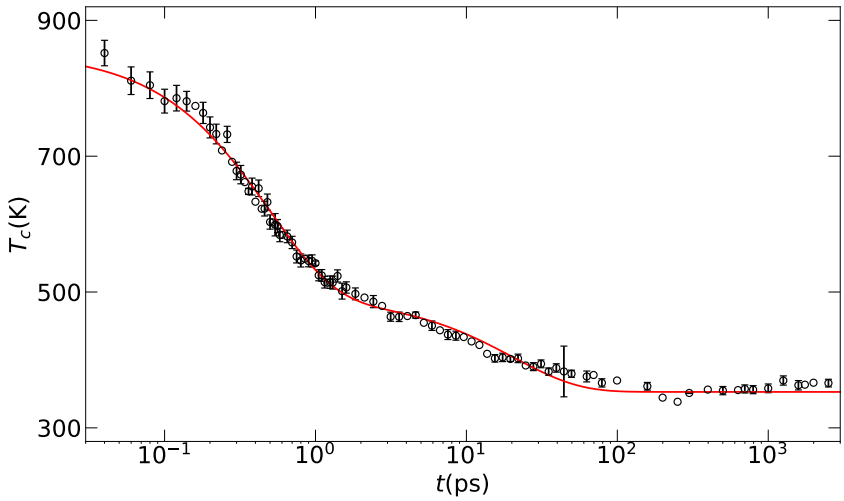

Figure 5.8: Carrier temperature T_c reported as a function of the pump-probe delay, t. The x-axis is logarithmic for clarity. The red line is a fit described in detail in the text.

1.6 eV just above the band gap (1.542 eV), a short-lived positive absorption feature at the bandgap and a weak, broad photoinduced absorption (PIA) at high energies. The negative ΔmOD is readily identifiable as a ground state bleach (GSB)[86, 88], corresponding to the accumulation of carriers near the band extrema. The quick PIA has been alternatively interpreted in different works as arising from excitons,[68] band-gap renormalization[88] and polaron formation.[56] The broad PIA region is generally observed [86, 88] and was attributed to a photoinduced change of the refractive index[88], or to an effect caused by band-gap renormalization[86]. The band-edge PIA quickly disappears within 1 ps, while the broad PIA remains, along with the bleach, even 2.5 ns after photoexcitation. In Figure 5.7 (b) spectra at t =158 ps and at t =2506 ps are also presented. The amplitude of the GSB grows slowly to a maximum around 158 ps delay, which may indicate carrier cooling towards the band edge on this timescale, or the diffusion of carriers away from the photoexcited surface.

Following an established methodology[86, 88, 145], thoroughly described in Chapter 2, the carrier temperature T_c was extracted from the high energy tail of the GSB at different pump-probe delay times.

The function $\Delta\alpha = A_0 e^{-E/k_B T_c} + \Delta\alpha_0$ was used, where A_0 is the equilibrium absorption coefficient and $\Delta\alpha_0$ is an offset added to take into account the influence of the broad PIA at higher energies. Although it has been suggested that the cooling dynamics of electron and holes could be different[144], for simplicity here we assume

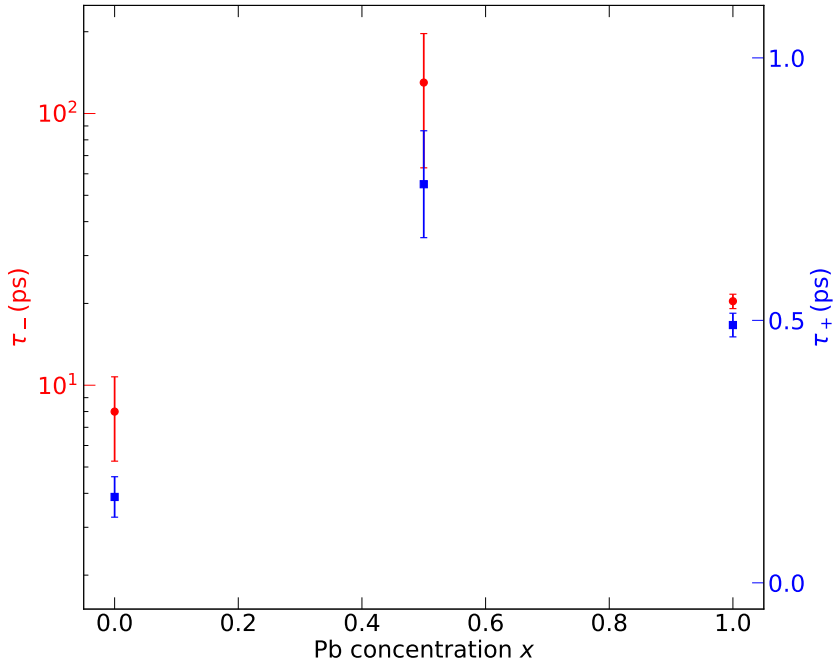

Figure 5.9: Two fit parameters τ_+ and τ_- for different concentration x. The short one (τ_+) represents the first quick step in the cooling process, while the long one (τ_-) represents the second, slower step of cooling (note the logarithmic y axis). Both times reach a maximum for the 50:50 mixture.

that $T_c = T_e = T_h$ on the basis that the excess energy is evenly distributed between electron and holes.

The extracted carrier cooling dynamic is reported in Figure 5.8 in the main panel. The red line is a fit using the TTM model described in Chapter 3 in its simplified version and an excellent agreement with the experimental T_c dynamic was obtained. The fit yielded $\tau_+ = 0.49 \pm 0.02\,\text{ps}$ and $\tau_- = 20 \pm 1.3\,\text{ps}$, while $A_\pm = 0.72$ and 0.28 respectively. It is then possible to identify the fast component as determined by the Fröhlich interaction, while the slow one as dominated by the HPB and therefore limited by the phonon-phonon decay rate. The fit was then performed on three compositions: x=0, 0,5, 1, which are reported in Figure 5.9. The short time constant τ_+ is longer for the 50:50 alloy, which is consistent with the results obtained by OPTP at a similar excess energy. The same is true for the longer time constant τ_-, but the difference is much greater, at least an order of magnitude, than the "pure" compounds.

In the next section all these experimental results will be compared together, finally answering the original question whether the results on OPTP and TAS can be compared, and an interpretation of the difference provided by the varying com-

position based on the TTM will be provided.

5.4 Discussion

In light of the results obtained in the course of this chapter it is possible to draw two succinct observations: (1) OPTP and TAS are not equivalent, and (2) the Pb-Sn ratio has a strong influence on the carrier cooling dynamic, but not in the same way in all regimes.

5.4.1 Comparison between OPTP and TAS

The cooling time measured by OPTP is in good quantitative agreement with the fast cooling time obtained from TAS when compared at similar excess energies. For instance for $x = 1$ and an excess energy 1.7 eV, TAS determined $\tau_+ = 0.35 \pm 0.04$ ps, while OPTP determined $\tau = 0.39 \pm 0.04$ ps at a similar fluence. Changing the fluence did not alter the Fröhlich cooling time obtained from either technique.

Individually the two experimental methods employed have advantages and disadvantages. In the OPTP experiment, when carriers have relaxed in energy too close to the band edge, the mobility will not differ significantly from the Γ point value. For this reason, OPTP does not provide information about τ_-, and just tracks τ_+. OPTP, therefore, provides a straightforward tool to measure the initial, rapid carrier cooling process (the Fröhlich stage), without the modelling assumptions of TAS. However, TAS probes the carrier's energy distribution close to the band gap, and hence has the advantage of being more sensitive to the cooling dynamics at lower carrier temperatures (later times) than OPTP. Together, they enable a complete picture of carrier cooling and mobility.

5.4.2 Influence of composition on the cooling dynamic

As said, the Pb/Sn ratio affects the different stages of cooling differently. This is not a surprise as the two stages correspond to two different regimes dominated by different mechanisms. In the first regime, dominated by the Fröhlich interaction, the carriers cool rapidly thanks to the efficient electron-LO phonon coupling. This stage is described by τ_+ in the TTM model and τ in the terahertz measurements, which are, as proven, effectively the same quantity. The TTM assumes the couplings are constant values. However, if the second cooling stage is ignored the electron-phonon

coupling can be estimated using an approximated formula, derived in Chapter 3:

$$k_0 = \frac{G_{ep}}{C_e} = \frac{4\alpha k_B}{3\pi^{\frac{1}{2}}\hbar}\frac{\Theta^{\frac{5}{2}}K_0(\Theta/2T_e)}{\sqrt{T_e}(T_e - T_p)}\frac{\sinh\left[(T_e - T_p)\Theta/2T_eT_p\right]}{\sinh\left(\Theta/2T_e\right)}. \tag{5.3}$$

Where $\Theta = \hbar\omega_{LO}/k_B$ for an LO phonon with angular frequency ω_{LO}; K_0 is the modified Bessel function of the second kind; and the strength of the electron-LO phonon interaction is given by $\alpha = \frac{e^2}{4\pi\varepsilon_0\hbar}\left(\frac{m^*}{2\hbar\omega_{LO}}\right)^{1/2}\left(\frac{1}{\varepsilon_\infty} - \frac{1}{\varepsilon_s}\right)$, where ε_s and ε_∞ are the static and high frequency dielectric constants and m^* is the bare electron mass.

Regarding the second stage of cooling, in Chapter 3 it was argued that the phonon-phonon coupling could be expressed as a sum of the rates of the optical-to-acoustic phonon channels:

$$\frac{G_{pp}}{C_p} = \frac{1}{\tau_K} + \frac{1}{\tau_R} + \frac{1}{\tau_{VB}}, \tag{5.4}$$

where τ_K, τ_R and τ_{VB} are the Klemens, Ridley and Vallée-Bogani decay times.

From the simulations presented in Chapter 3 it is moreover possible to argue that, provided that G_{pp}/C_p is smaller than G_{ep}/C_e (*i.e.* the phonon-phonon coupling is weaker than the electron-phonon coupling), τ_+ is controlled primarily by G_{ep}/C_e, while τ_- is primarily controlled by G_{pp}/C_p.

Considering first the influence of composition on the first cooling stage, the results from OPTP at lower excess energy (0.6 eV and 1.0 eV), where carriers were directly injected closer to the band edge, are the most interesting, since the influence of a possibly complicated bandstructure is minimal. As reported in Figure 5.5, the cooling time is longest for the full lead sample ($\tau = 0.4$ ps), and steadily shortens with increasing Sn concentration (lower x) to a minimum at $x = 0.25$. For the full tin sample the cooling time increased marginally to $\tau = 300$ fs. These differences can be assigned to a modification of the carriers' effective mass or to changes in the LO phonon modes. Indeed, as Equation 5.3 indicates, the decay rate k_0 in the Fröhlich regime is a function of ω_{LO} and m^*. The phonon modes for $x = 0$ will be higher in frequency in general than for $x = 1$, since Sn is lighter than Pb: this trend can be seen for instance in the Debye temperatures for $MASnI_3$ (230 K) and $MAPbI_3$ (175 K).[184] A larger phonon frequency increases k_0, consistent with the lower τ and τ_+ observed in experiment for smaller x. Additionally, the prominent band bowing for the alloys implies changes to the effective mass, which will modify α and thereby k_0. This may account for the apparent minimum in τ at $x = 0.25$ rather than at $x = 0$. In particular it will be intriguing to establish whether the

non-linear behaviour of the bandgap of the alloy (evident in Figure 5.1) is driven by crystallographic changes that also create bowing in the phonon frequencies.

Examining instead the high excess energy regime (e.g. 1.7 eV or 2.5 eV) the Fröhlich cooling time does not appear to vary substantially with x for the $x = 0.5 - 1.0$ samples, as can be seen in both OPTP (Figure 5.5) and TAS (Figure 5.9) results. At higher excess energies the approximations in Equation 5.3 are not valid, and the cooling rate will depend on details of the electronic bandstructure (e.g. the influence of non-parabolic bands or different bands).

At high excess energies the HPB can be accessed, and the influence of x on the slow component (τ_-) is reported in Figure 5.9. τ_- is substantially larger than τ_+ for all compositions studied. Note that the short recombination time of the full Sn-based perovskite (~10 ps) means that the value $\tau_-(x = 0) = 8$ ps is probably an underestimate. Remarkably, the slowest cooling dynamic occurs for the mixed lead-tin compound: $\tau_- = 120$ ps is an order of magnitude larger than for $x = 0$ and $x = 1$.

An interpretation of the slow hot carrier cooling in the HPB regime (increased τ_-) can be given using the TTM. With reference to the simulations performed in section 3.2.4, an order of magnitude reduction in G_{pp}/C_p is required to account for the larger τ_- observed. One explanation is that the phonon-phonon interaction is suppressed in the mixed compound in comparison to the "pure" compounds. In the HPB picture, the relevant hot LO-phonons are at low frequencies (in the THz range), such as the I-Pb-I bend and Pb-I stretch modes.[29] The phonon bandgap, defined as the difference in the maximum acoustic phonon energy and minimum optical phonon energy, is expected to increase when atoms with a significant mass difference are coupled[82], as for the mixed Pb-Sn alloys studied here, leading to a suppressed Klemens decay rate and a lower G_{pp}/C_p (see Equation 5.4). As an alternative mechanism to account for the enhanced τ_-, changes in C_p may also contribute, in particular as the Debye temperatures vary. Slow carrier cooling has been reported recently for a mixed lead-tin compound ($FAPb_xSn_{1-x}I_3$),[115] using TAS, with slow components as long as 500 ps reported (although extrapolated outside the 100 ps experimental time window). In this work the temperature dynamic was measured with the same transient absorption framework applied here, however, the experiment was performed at a fixed, small, excess energy. The short times they observed are consistent with the OPTP results reported here at low excess energy: there is a minimum at a mixed composition, and a maximum for the full lead. The long time they observed is consistent with the observations reported here, the differences (no HPB effect for the full lead sample, even higher value for the mixed lead-tin) could be

ascribed to different experimental conditions (excess energy, injected carrier density) or on the fitting procedure (as said the time-window in that work was limited to 100 ps). It is important to underline, however, how this work, did not try extensively to connect the observed differences to the underlying microscopic physics, and their fitting model remains strictly empirical.

Finally, by comparing the results of OPTP with the results of TAS we can conclude that the hot carriers in the hot phonon bottleneck regime have a mobility comparable to the cold carriers. For instance, the temperatures deduced from TAS allow one to identify that for $t > 1$ ps the perovskite was in the HPB regime. Under the same experimental conditions (same excitation fluence, excess energy and time delay), the photoconductivity reported by OPTP has already reached a plateau (Figure 5.4), indicating that the hot carrier distribution is as mobile as the cold carriers.

5.5 Influence of Br addition to the hot carrier dynamic

This final section will build on the results obtained in the previous sections and will introduce a second alloy: $Cs_{0.05}(FA_{0.83}MA_{0.17})_{0.95}Pb(I_{0.83}Br_{0.17})_3$. This is one of the best performing MHP semiconductors to date, both in terms of efficiency and stability[172] and therefore is a very interesting sample to study in its own right. In the context of HCC, this sample acquires interest as it is formed by alloying the halide. The effect of changing the halide composition on HCC has not been studied in detail, however, one could expect, following the discussion for the mixed lead-tin samples, its influence to be relevant since it goes to affect the same LO-phonon modes responsible for the Fröhlich cooling and the appearance of a hot phonon bottleneck.

5.5.1 Temperature dynamic

The sample was studied using TAS, in very similar conditions to the other samples. The time-energy contour plot is reported in Figure 5.10, for a high fluence case, where it looks very similar to the one reported in Figure 5.7 if not for the slightly higher band gap (around 1.6 eV). The slight shift in the band gap is caused by the incorporation of Br, which is known to blueshift the band gap, as already discussed briefly at the beginning of Chapter 4 in the study of Br-incorporated $CsSnI_3$ samples[164]. Two other differences are the apparent absence of the broad PIA at higher energies, which is still present, however appears less pronounced due to the scale, and the faster recombination dynamic, which causes the 2506 ps spectrum to

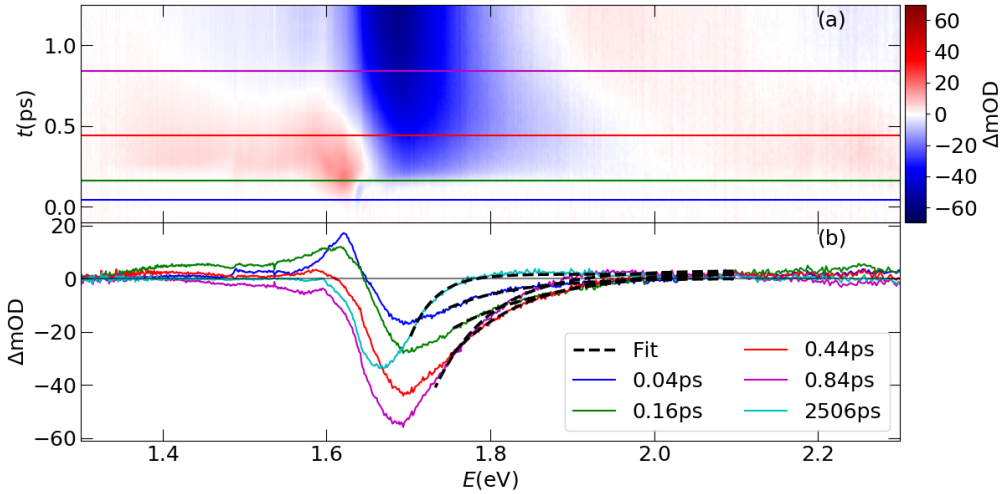

Figure 5.10: In panel (a) a contour plot of the transient change in absorption is reported for $Cs_{0.05}(FA_{0.83}MA_{0.17})_{0.95}Pb(I_{0.83}Br_{0.17})_3$ at 400 μJ/cm^2. The x axis is the probe energy (in eV) and the y axis is pump-probe time delay, in ps. The absorption is reported for the first 1.2 ps for clarity. Three prominent features are observed in the spectrum: a quick and narrow photoinduced absorption region at the band gap, a strong absorption bleach just above the band gap and a broad photoinduced absorption at higher energies, which is harder to see in the plot due to the scale. The origin of these features is discussed with more detail in the text. In panel (b) few transient absorption spectra are reported at different pump-probe delays. The dashed black lines correspond to fits used to extract the carrier temperature. Part of these spectra correspond to time slices in panel (b) and are indicated there with matching colours.

have a smaller, redshifted peak. The reduction of the peak is obvious as there are less carriers injected, so there is less induced transmission change. The redshift is more subtle: it is caused by the progressive recombination of carriers which free previously occupied states at the band edge, reducing the GSB effect. Following the same methodology the carrier temperature versus time was extracted and it is reported in Figure 5.11 for two excitation densities: 40 and 400μJ/cm^2. This is the same figure that was also briefly reported in Chapter 3 to illustrate the TTM performance. In more detail, the figure reports the temperature dynamic in two fluence cases; increasing the fluence ten-fold has, not only induced the appearance of a slow-down of cooling (evident in the 1-100 ps range), but also an increase of the initial temperature. The continuous lines are fits using the TTM model, and the dashed lines are the corresponding phonon temperatures, calculated from the same model. The small gap between the carrier and the phonon temperature in the figure is ascribed to the Auger heating effect. The reported fit at high fluence

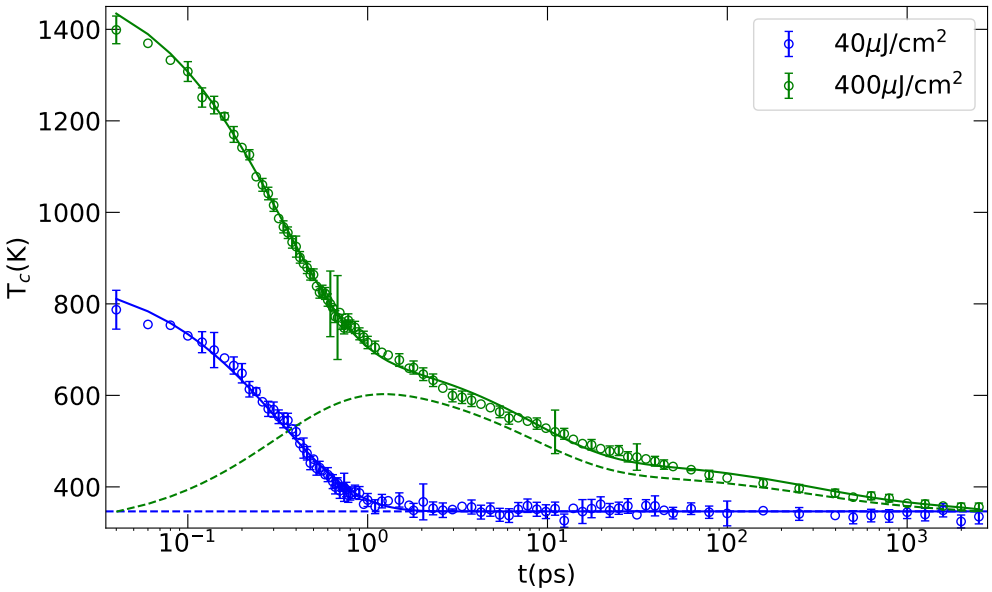

Figure 5.11: Cooling dynamic of $Cs_{0.05}(FA_{0.83}MA_{0.17})_{0.95}Pb(I_{0.83}Br_{0.17})_3$ at low and high fluence. Continuous lines are fits using models described in the text, dashed lines are the corresponding calculated phonon temperatures.

was obtained using the full model including a time-dependent Auger heating effect (time-dependent because the carrier density is not constant over the whole 3 ns range at this fluence). This was required to model the slow tail in the cooling evident at t>100 ps. The time-dependent Auger term was modelled as the square of a bi-exponential carrier recombination: $G_A(t) = k_3 N^2(t) = G_A(0)(Ae^{-t/\tau_1} + Be^{-t/\tau_2})^2$, where $N(t)$ is the carrier density, τ_1 and τ_2 are two recombination times and A and B are the weights of the two exponential terms. The resulting numbers are reported in Table 5.2, along with all the other samples. These values are consistent with the values estimated for the full lead sample without Br.

5.5.2 Fröhlich cooling stage

As already discussed extensively, the first, fast, cooling stage is dominated by the Fröhlich interaction, and the easiest way to study it is to rely on OPTP spectroscopy. The photoconductivity onset of two different samples, obtained from this analysis, are reported in Figure 5.12: the first few ps of electric field change are reported for the same composition prepared with different anti-solvents. Changing the anti-solvent, used to promote crystal formation, from chlorobenzene (CB) to tolulene did not alter the cooling time τ, although the exact solvent is more important for Sn-containing perovskites[51]. The Pb-containing perovskites, when

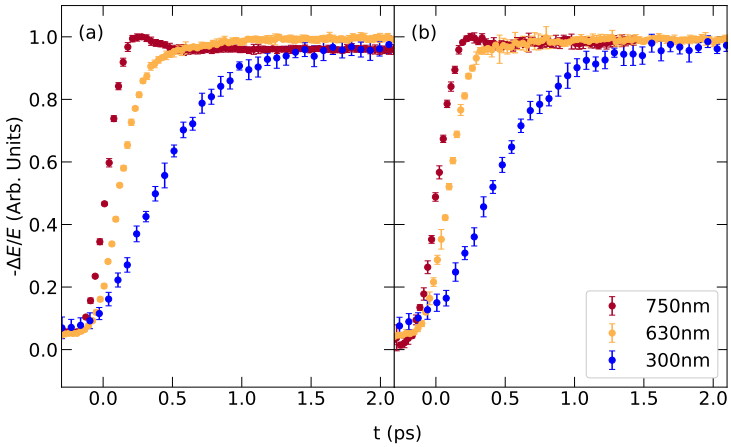

Figure 5.12: In this figure the photoconductivity onset of $Cs_{0.05}(FA_{0.83}MA_{0.17})_{0.95}Pb(I_{0.83}Br_{0.17})_3$ with chlorobenzene (a) and toulene (b) as anti-solvent is reported at different wavelength excitations. The trend in the two cases is similar with shorter wavelength excitation yielding slower cooling.

compared to GaAs or $CsSnI_3$ (extensively studied in the previous chapter), show a more featureless pump wavelength dependence of τ, compatible with the full lead sample studied in the previous sections. Multiple samples consistently exhibited the same rise times. Similarly to the full lead sample without bromine the rise time is faster than $Rb_{0.1}Cs_{0.9}SnI_3$ (shown in the previous chapter) and comparable with GaAs before side-valleys become accessible. To quantitatively compare the different samples the same analysis described in the previous section was applied. The outcome for $Cs_{0.05}(FA_{0.83}MA_{0.17})_{0.95}Pb(I_{0.83}Br_{0.17})_3$ is plotted in Figure 5.13 along with data for the full-Pb sample without bromine. The rise times start from below the instrumental time resolution under resonant excitation at the bandgap (not reported here), before slowly, but steadily, increasing with energy. For instance, $\tau \simeq 100\,\text{fs}$ at 2.0 eV excitation (0.4 eV excess energy), which increases to $\tau \simeq 450\,\text{fs}$ at 3.2 eV (1.6 eV excess energy), before plateauing. The rise times remain overall much shorter than anything measured for $Rb_{0.1}Cs_{0.9}SnI_3$ (Chapter 4), indicating an extremely efficient hot-carrier cooling rate for both Pb based materials. From the same figure another interesting fact can be noted: the sample without added Br shows a systematically slower carrier cooling time than the counterpart with Br. In the same figure it is possible to see how no major difference arises from the uses of the two different anti-solvents.

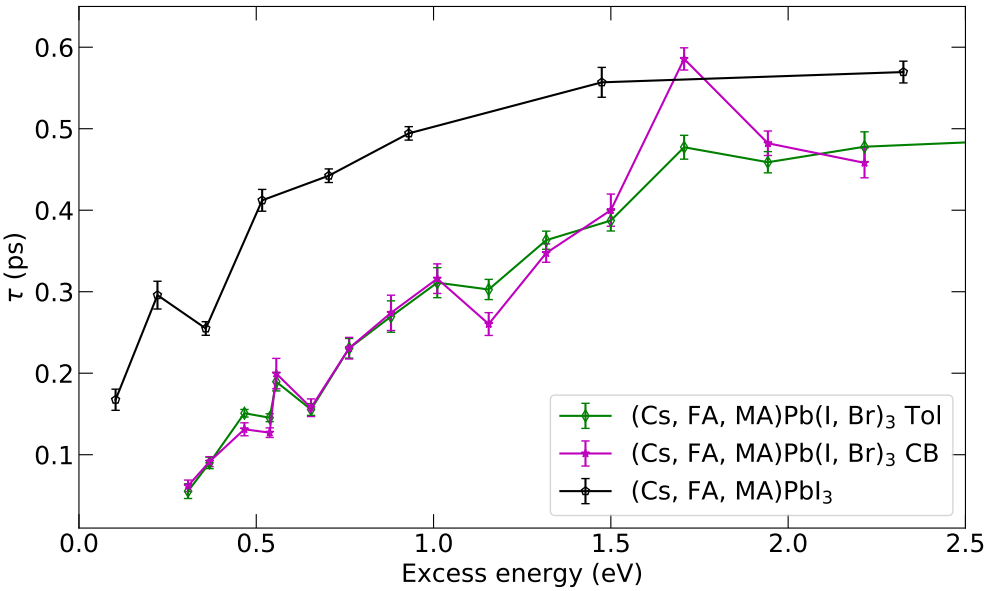

Figure 5.13: In this figure the cooling time for different samples is reported. $Cs_{0.05}(FA_{0.83}MA_{0.17})_{0.95}PbI_3$ (black pentagons), and two samples of $Cs_{0.05}(FA_{0.83}MA_{0.17})_{0.95}Pb(I_{0.83}Br_{0.17})_3$ with different solvents used: toluene (green diamonds) and cholorobenzene (magenta stars). The two samples with added Br seem quite consistent with each other, and both are faster than the sample with pure iodine. The lines are a guide to the eye.

5.5.3 Final comparison

For the pure Pb compound the partial substitution of I by Br induces a faster Fröhlich cooling time, as can be seen in Figure 5.13. Br substitution is known to blue-shift the frequencies of the optical phonons associated with the metal halide octahedra.[29] The enhanced phonon frequency may increase the electron-phonon cooling rate, for the same reasons as outlined for Sn substitution.

Regarding the HPB regime, the coupling parameters are reported in Table 5.2 along with all the other samples investigated. G_{ep}/C_e is consistent among the various samples, although the Br-substituted one appears to have a stronger coupling than

x	G_{ep}/C_e (THz)	G_{ep}/C_p (THz)	G_{pp}/C_p (THz)	$G_A(0)$ (THz)
0	3.3	2.7	0.2	/
0.5	1.1	0.6	0.01	/
1	1.49	0.53	0.067	/
1, with Br	2.3	0.8	0.2	0.14

Table 5.2: Here are reported the coupling rates for all the samples measured.

the lead counterpart, which is consistent with the faster τ_+. G_{ep}/C_p is consistently a factor 2 or 3 smaller than G_{ep}/C_e, consistent with the simulations performed in section 3.2 which predicted a similar ratio for the two constants given the relative high temperature at which the HPB is triggered. The only exception is $x = 0$, which, however, has a fast recombination dynamic, so the signal to noise is substantially worse at times later than few ps, which may have influenced the value. Regarding G_{pp}/C_p all the values are consistently lower than, or equal to 0.2 THz, and, as expected, the smallest values belongs to the 50% concentration. The full lead sample, the next smaller, has a value that is almost 7 times larger, which is consistent with the difference in τ_- in Figure 5.9. Surprisingly the Br-added sample has a stronger coupling, comparable with the Sn one (which, as said, due to the fast recombination is probably an upper limit), however, it should be noted that these values have been obtained at a stronger carrier density and with a model capable of discerning the Auger component, so the values are not necessarily comparable directly.

All these observations suggest that a small Br substitution does not change the phonon bandstructure enough to enhance the HPB effect. Considering the results on the lead-tin compounds, and a previous study on the metal composition influence on HCC[115], probably the Br concentration is not enough to achieve a substantial effect. Future studies will have to investigate this.

5.6 Final remarks

This chapter attempted to provide a broad study of the influence of alloying on HCC. Firstly a systematic study of the HCC dynamic while changing the Pb-Sn concentration was presented: the quality of the alloyed samples was assessed and the carrier cooling times were studied with OPTP and TAS, and analysed with the TTM introduced in Chapter 3. This yielded a low-excess energy cooling time that gets faster with mixed compositions, and two high-excess energy times ($\tau_\pm$) that get both longer for mixed compositions. The HPB-dominated time τ_- becomes an order of magnitude larger than those of the "pure" counterparts. This was linked to a widening of the phonon band gap caused by the modification of the phonon modes associated with the Pb-I bonds with the alloying of lighter Sn. Finally one of the best performing perovskite materials [172], consisting of $Cs_{0.05}(FA_{0.83}MA_{0.17})_{0.95}Pb(I_{0.83}Br_{0.17})_3$ was studied. The aim was to verify if any differences arose from the halide alloying. The Fröhlich-dominated time seems substantially faster for the Br-added sample, probably because of an enhancement of the phonon frequency caused by the Br incorporation[29]. No substantial differences were found regarding the HPB-

dominated stage, although more work is needed with additional compositions, to verify if this is the case.

This chapter confirms the idea that the HCC is a complex subject, where multiple phenomena coexist and influence each other yielding a very wide parameter space, that this work only started to explore, as discussed further in the conclusions chapter.

Chapter 6

Carrier cooling and mass change in InSb

In this chapter, cyclotron spectroscopy measurements on InSb are presented. This technique was applied to investigate the effective mass of carriers at different energies in the conduction band, either because of injection at high energies or because of a high quasi-Fermi level. The reason why InSb was chosen for this study is its simplicity as a case study: its physical and chemical properties are well-known and the low band gap energy allows high injection energies to be readily accessible. On top of that the fact that InSb is a strongly nonparabolic material allows a simplified analytical treatment of how this influences the conductivity and how could that affect the effective mass of carriers high in the band. At last, InSb is an interesting material *per se*: with an extremely high room temperature mobility it is a promising candidate for numerous applications, which include high-speed transistors [185], infrared detectors [186] and quantum wells [187] as explained below.

In this chapter the first section will give a brief introduction to narrow-gap semiconductors. The second section will introduce the analytical description of the deviations from the parabolic approximations in the conduction band (CB) of InSb, and will include this into the framework of the Boltzmann transport equation in order to recover an expression for the frequency-dependent conductivity. The third section will present the cyclotron spectroscopy results of InSb and $Al_{0.05}In_{0.95}Sb$, along with the cyclotron resonances measured at different pump-probe delays during the onset of photoconductivity and the cyclotron spectroscopy at different injected number of carriers.

All the experiments performed in this chapter have been acquired by myself and C. Xia in the laboratory of Prof. M.B. Johnston at the University of Oxford.

Samples were prepared by Dr. M. Ashwin from the University of Warwick. The InSb sample was a 6.5μm undoped layer of InSb, grown by molecular beam epitaxy (MBE) on semi-insulating GaAs. The $Al_{0.05}In_{0.95}Sb$ sample was grown with the same method on the same substrate and had a thickness of 3μm. The experimental set-up is described in section 2.1.6. The experiment was performed with a 5kHz repetition rate laser, which generated THz radiation by focusing the 800 nm beam onto a ZnTe crystal. Detection was also performed with a ZnTe crystal. The same 800 nm beam was used as a pump, resulting in 1.3 eV of excess energy. Most of the results performed in this chapter, unless otherwise specified, occurred at a incident pump power of 3mW (named "high fluence") or 0.3mW (named "low fluence"). the transmission spectra were measured at a pump-probe delay of 200 ps.

6.1 Narrow-gap semiconductors

Narrow-gap semiconductors, in particular indium antimonide and its compounds, are a class of materials that have raised new interest in recent years because of their peculiar properties [188], like a very low effective mass, and consequently high mobility, and low energy gap. In the search for new materials with functionality beyond that of silicon the antimonide compounds stand out thanks to their high room-temperature mobility [185, 188]. The most interesting applications so far involve: high-speed transistors [185], infrared detectors [186] and quantum wells [187, 189]. InSb is also a promising material in the field of spintronics thanks to a large spin-orbit coupling and enhanced g-factor in InSb quantum wells[187, 190]. Especially in the context of quantum well technology, InSb has been used in conjunction with Al-doped InSb ($Al_{0.05}In_{0.95}Sb$) as a barrier material. $Al_{0.05}In_{0.95}Sb$ is a narrow-gap semiconductor with a slightly larger band gap and less extreme properties than InSb. In this chapter $Al_{0.05}In_{0.95}Sb$ will often be used as comparison for InSb peculiarities. In addition to the interesting applications, the extremely low band gap of InSb (0.17 eV at room temperature) causes the bandstructure to deviate rapidly from the parabolic approximation, and this makes InSb an interesting material to test phenomena related to these characteristics such as the mass change at different injected carrier densities [191].

6.2 Nonparabolicity in InSb

The most famous feature of InSb is its extremely low band gap: 0.17 eV (0.24 eV) at 300 K (0 K). Two consequences of this fact are: the non-negligible thermal pop-

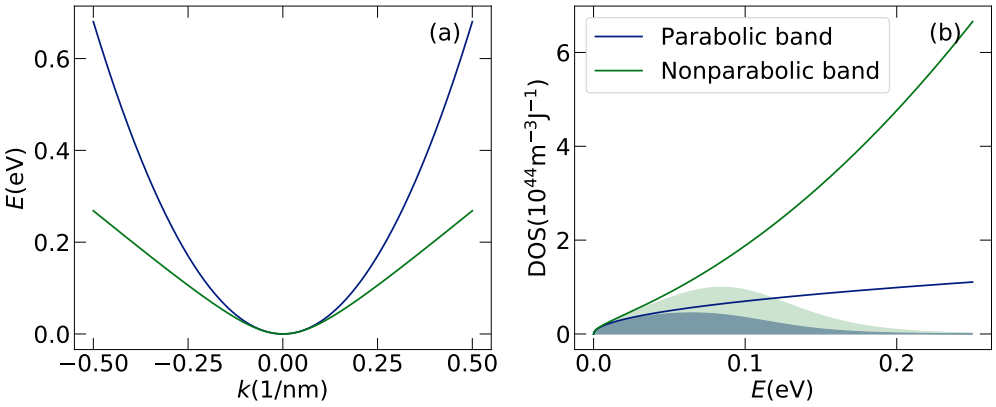

Figure 6.1: Panel (a) parabolic band dispersion (blue) vs nonparabolic dispersion (green). In (b) the DOS is reported for both a parabolic (blue) and nonparabolic (green) dispersion. The shaded area is the carrier energy distribution at a temperature of 300 K and a quasi-chemical potential of 100 meV.

ulation of carriers in InSb, and the high nonparabolicity of the bandstructure. All the measurements reported in this work were performed at a lattice temperature of 2 K, and hence the former can be ignored. In general, any bandstructure is nonparabolic: the description of a band as a parabola holds, strictly speaking, only around an extremum. By nonparabolic, however, it is meant that the bandstructure around a minimum quickly diverts from a parabolic approximation even at low energies. A complete description of how this happens will be provided in the remainder of this section. However, in brief, the non-parabolicity can be parametrised by a constant $\alpha \propto \frac{1}{E_g}$, and therefore the smaller the band gap the stronger the effect. Since InSb has a very low band gap, the effect is significantly stronger than in most semiconductors. For this reason InSb provides a benchmark for the study of nonparabolicity[191, 192]. In this section the basics of the effects of nonparabolicity are reviewed, in the simplified assumption of an homogeneous, isotropic material, ignoring spin-orbit terms and multi-band effects. A compete description can be found in Zawadzki [191].

6.2.1 Nonparabolic bandstructure

The nonparabolicity can be modelled with $k \cdot p$ perturbation theory, following Kane's method[192]. The band energy can be given by finding ε from:

$$\frac{\hbar^2 k^2}{2m_0^*} = \sum_{l=1} \alpha_l \varepsilon^l, \tag{6.1}$$

where k is the wavevector, m_0^* is the effective mass at the Γ-point, ε is the energy and the first two α_l coefficients for InSb are $\alpha_1 = 1$ and $\alpha_2 = \alpha = \frac{1}{E_g}\left(1 - \frac{m_0^*}{m_e}\right)^2$. This description allows us to truncate the precision of the calculations at the preferred order, which in this case will be the second, in such a way Equation 6.1 can rewritten as:

$$\frac{\hbar^2 k^2}{2m_0^*} \simeq \varepsilon\left(1 + \alpha\varepsilon\right). \tag{6.2}$$

From this formula it is possible to calculate an expression for the CB of InSb:

$$\varepsilon_c(k) = -\frac{1}{2\alpha} + \frac{1}{2\alpha}\sqrt{1 + 2\alpha\frac{\hbar^2 k^2}{m_0^*}}. \tag{6.3}$$

The difference between Equation 6.3 and a normal parabolic dispersion is reported in Figure 6.1 (a) where the nonparabolic dispersion has a less pronounced dependence on the wavevector k, and it tends to a linear dispersion at higher wavevectors. Starting from Equation 6.3, most relevant quantities such as the density of states (DOS), $g(\varepsilon)$, or the energy dependent effective mass, $m^*(\varepsilon)$, can be computed (see appendix A):

$$g(\varepsilon) = \frac{1}{2\pi^2}\left(\frac{2m_0^*}{\hbar^2}\right)^{3/2}(2\alpha\varepsilon + 1)\sqrt{\alpha\varepsilon^2 + \varepsilon}, \tag{6.4}$$

$$m^* = m_0^*\sqrt{1 + 4\varepsilon\alpha} \simeq m_0^*(1 + 2\varepsilon\alpha). \tag{6.5}$$

As an example the DOS is reported in Figure 6.1 (b) for both parabolic and non-parabolic dispersion. It can be seen as for very low energies the DOS diverges dramatically from the parabolic case, and is also substantially larger at very low energies. The shaded area in the same figure represent the DOS multiplied by the Fermi-Dirac (FD) distribution at 300 K and 100 meV chemical potential, yielding the carrier distribution in energy. The finite temperature helps highlighting the difference in the state occupation caused by the two different band dispersions.

Once an analytical description of the CB is given, it can be used to describe its influence on the frequency-dependent conductivity. This is possible through the framework of the Boltzmann transport equation, and is be the topic of the rest of this section.

6.2.2 Boltzmann transport equation: influence of nonparabolicity on photoconductivity

To include nonparabolicity into the frequency-dependent conductivity it is necessary to use the Boltzmann transport equation, as previously applied for GaAs and InAs

to interpret the conductivity at high chemical potential[193]. The basics of including nonparabolicity into the D.C. conductivity were calculated by Zawadzki [191] in case of an *anisotropic* band dispersion. Following a similar approach, the remainder of this section provides an explicit derivation of how the nonparabolicity influences the frequency-dependent conductivity of an *isotropic* material.

The Boltzmann Transport equation can be expressed as[193]:

$$\sigma(\boldsymbol{q},\omega) = \frac{e^2}{4\pi^3}\int_{\boldsymbol{k}} \frac{\tau(\hat{e}\cdot\boldsymbol{v})^2}{1-i\tau(\omega-\boldsymbol{q}\cdot\boldsymbol{v})}\left(-\frac{\partial f_0}{\partial\varepsilon}\right)_{\mu} d\boldsymbol{k}, \tag{6.6}$$

where τ is the momentum scattering time, $\hat{e}$ is the polarization vector, e is the elementary charge, $\boldsymbol{v}$ is the electron velocity, ω and $\boldsymbol{q}$ are the angular frequency and the wavevector of the probe light, and f_0 is the Fermi-Dirac distribution, whose derivative is calculated at the quasi-chemical potential μ. The integral is extended in the whole of k-space. Including nonparabolicity into the framework of the Boltzmann transport equation can be done by incorporating Equation 6.3 into the expression for the velocity ($v = \frac{1}{\hbar}\frac{\partial\varepsilon_c}{\partial k}$). A detailed calculation is given in appendix A. The resulting frequency-dependent conductivity can be expressed as follows (ignoring the dependence from q as per the long-wavelength approximation discussed in more detail the appendix):

$$\sigma(\omega) = \frac{e^2}{3\pi^2}\frac{\sqrt{2m_0^*}}{\hbar^3}\int_0^{\infty}\frac{\tau}{1-i\omega\tau}\varepsilon^{3/2}\frac{(1+\varepsilon\alpha)^{3/2}}{\sqrt{1+4\alpha\varepsilon+4\alpha^2\varepsilon^2}}\left(-\frac{\partial f_0}{\partial\varepsilon}\right)_{\mu} d\varepsilon \tag{6.7}$$

In the limit of T$\rightarrow$0 K, the derivative of the FD tends to a delta function ($\delta(\varepsilon-\varepsilon_F)$), which means the integral is evaluated only at the Fermi surface:

$$\sigma(\omega) = \frac{e^2}{3\pi^2}\frac{\sqrt{2m_0^*}}{\hbar^3}\frac{\tau(\varepsilon_F)}{1-i\omega\tau(\varepsilon_F)}\varepsilon_F^{3/2}\frac{(1+\varepsilon_F\alpha)^{3/2}}{\sqrt{1+4\alpha\varepsilon_F+4\alpha^2\varepsilon_F^2}}. \tag{6.8}$$

Equation 6.8 has a similar form, to the standard Drude conductivity (see section 2.1.3) as all of the variables are evaluated for a fixed energy surface, and are hence constants. Defining:

$$N^* = \frac{1}{3\pi^2}\left(\frac{2m_0^*}{\hbar^2}\right)^{3/2}\varepsilon_F^{3/2}(1+\alpha\varepsilon_F)^{3/2}, \tag{6.9}$$

as a new definition of the carrier density, using the calculated expression for the effective mass (Equation 6.5) and neglecting the term $\alpha^2\varepsilon_F^2$ in Equation 6.8 (which

is higher order in $\alpha\varepsilon$), then Equation 6.8 can be rewritten as:

$$\sigma(\omega) = \frac{N^*(\varepsilon_F)e^2}{m^*(\varepsilon_F)} \frac{\tau(\varepsilon_F)}{1 - i\omega\tau(\varepsilon_F)}, \tag{6.10}$$

which is a Drude-shaped frequency dependent conductivity. It is therefore possible to conclude that the nonparabolicity would not affect the frequency dependence of the observed spectrum. It has to be said, however, that this is true only, strictly speaking, in the limit of $T \to 0$. At finite temperatures this is generally not correct as the energy dependence of m^* and τ have to be considered in Equation 6.7. This result is especially important as if the conductivity is Drude-like in absence of a magnetic field, it is safe to assume that this is the case for the magnetoconductivity, therefore allowing the standard THz cyclotron spectroscopy framework to be applied [127]. Finally, it is important to notice that Equation 6.9, in the limit $\alpha\varepsilon \to 0$ reduces to the well-known expression for the carrier density of a Fermi gas [2].

Thanks to the formalism developed in this section it is possible now to interpret the results that will follow: using THz cyclotron spectroscopy the effective mass of InSb will be measured in different conditions. The measured values of the effective mass will differ widely from the expected value at the Γ-point, and this simple approach will aid the interpretation of the results.

6.3 Carrier cooling in InSb

In this section the focus will be on how the energy band relaxation of hot carriers is reflected in the THz photoconductivity rise time, and in the change of mass during said rise observed with cyclotron spectroscopy. After that an exploratory experiment is reported, which was aimed at verifying if THz spectroscopy is capable of observing the change of effective mass at different injected carrier density. All experiments reported in this chapter were performed in a helium cryostat at a temperature of 2 K, hence $\mu \to \varepsilon_F$.

6.3.1 Effective mass at low fluence

In order to measure the effective mass of InSb, cyclotron spectroscopy was performed. This was done at relatively low fluence to reduce the influence of nonparabolicity. Figure 6.2 reports the results. Transmission spectra were acquired at different magnetic fields, between 0.1 and 1T with 0.1T steps, to ensure the resonances were well within the bandwidth of the experiment (0.2-2 THz). Figure 6.2 (a) reports the various time domain traces acquired within this range, these cor-

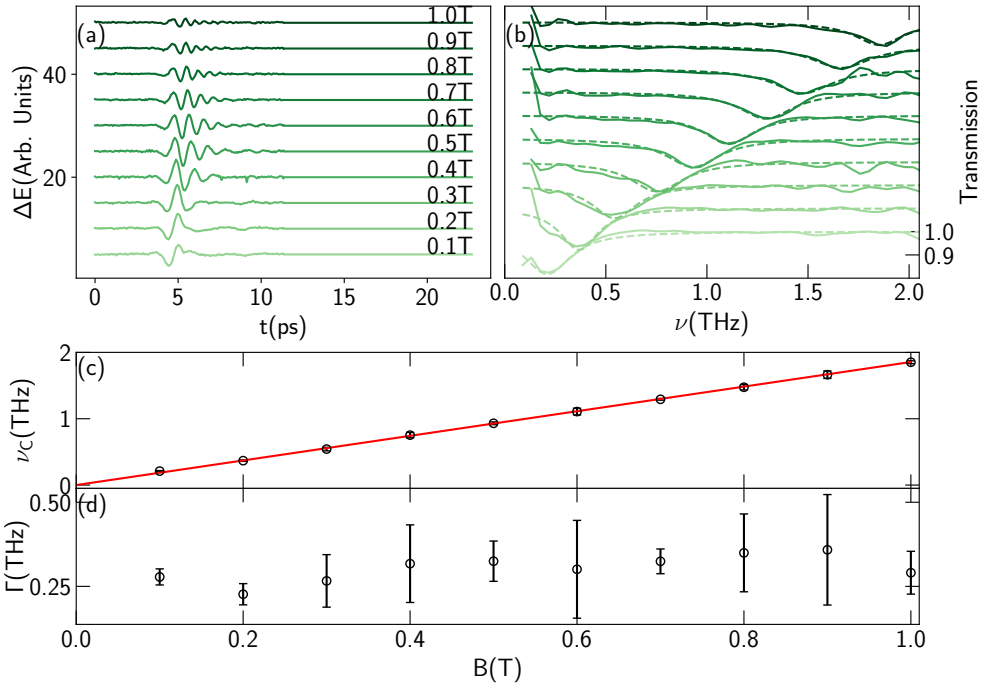

Figure 6.2: Panel (a) is the change in electric field induced by the pump under magnetic field. The oscillations induced by the cyclotron resonance are clearly visible. All the pulses have been shifted for clarity. (b) Transmission spectra (solid lines) clearly showing the cyclotron dip. The spectra correspond to different magnetic fields from 0.1 to 1T, they have been shifted upwards for clarity. The dotted lines represent fits with Lorentz functions. (c) cyclotron frequency versus magnetic field. These are the central frequency of the Lorentz fit. The red line is a fit of the cyclotron frequency. The corresponding obtained effective mass is m^*/m_0=0.01513±0.00005. The ν_0 parameter (Equation 6.12) was fixed to 0. Panel (d) reports the linewidths, these are the Γ linewidths of the Lorentz fits in Equation 6.11.

respond to the difference between the transmitted THz pulses with and without photoexcitation with the presence of a magnetic field: $\Delta E = E_{on}(B) - E_{off}(B)$. As no thermal carriers were present at the 2 K at which the experiment was performed, this is equivalent to $E(B) - E(0)$. Panel (b) reports the transmission spectra as the green continuous lines. Both have been offset vertically for clarity. Both the time domain traces and the transmission spectra show clear signs of a resonance: as an oscillation in the time trace and a dip in the frequency domain. The dotted lines on the transmission spectra represent fits performed with a Lorentzian function:

$$L(\nu) = \frac{1}{2}\frac{A\Gamma}{(\nu - \nu_C)^2 + (\frac{\Gamma}{2})^2}. \tag{6.11}$$

From which the cyclotron frequency was extracted as the central frequency ν_C, and Γ was used as a measure of the linewidth. It should be noted that with the definition above Γ corresponds to the full width at half maximum (FWHM). Both these quantities are reported in Figure 6.2 (c) and (d) respectively, against the magnetic field. The uncertainties in the central frequency have been estimated using the uncertainty provided by the lmfit package[194], which is based on the scipy.optimize.leastsq() method, which is part of the standard Scipy distribution. The cyclotron frequencies (black circles) appear to be well fitted by a straight line passing through the origin (red line):

$$\nu_C = aB + \nu_0, \tag{6.12}$$

where B is the magnetic field, a and ν_0 are the line's coefficients, and ν_0 has been fixed to 0. The effective mass is readily obtained from:

$$m^* = \frac{e}{2\pi a}. \tag{6.13}$$

The uncertainties in the central frequency have been considered in the fit of the parameter a and propagated into the effective mass. The effective mass obtained by the fit is: m^*/m_0=0.01513±0.00005 which is slightly higher than the well known Γ-point value of 0.014 for bulk InSb [191]. This slightly higher value is explainable either by the formation of a polaron [195] or by the influence of nonparabolicity [191]. Once these two effects have been noted the value obtained is consistent with the expected value. In panel (c) the linewidths seem to be quite small (all around 0.3 THz) and basically constant with the magnetic field.

As a comparison to the experiments performed on InSb the effective mass of $Al_{0.05}In_{0.95}Sb$ is also reported. The same analysis applied to InSb is reported for $Al_{0.05}In_{0.95}Sb$ in Figure 6.3. Panel (a) reports the various time domain traces acquired between 0.5 and 1 T, while (b) reports the transmission spectra as green continuous lines. Both have been shifted upwards for clarity. The same analysis performed on InSb was applied. The central frequencies and the linewidths are reported in Figure 6.2 (c) and (d) respectively, against the magnetic field. The cyclotron frequencies (back circles) appear to be well fitted by a straight line passing through the origin. The linewidths at lower magnetic field are substantially higher, this is likely caused by the fact that at these magnetic fields the dip is very close to the lower edge of the bandwidth, so it is more complex to estimate a linewidth accurately. The effective mass obtained by the fit is: m^*/m_0=0.0231±0.0006, with ν_0 fixed to 0. The effective mass of $Al_{0.05}In_{0.95}Sb$ is higher than InSb, which is

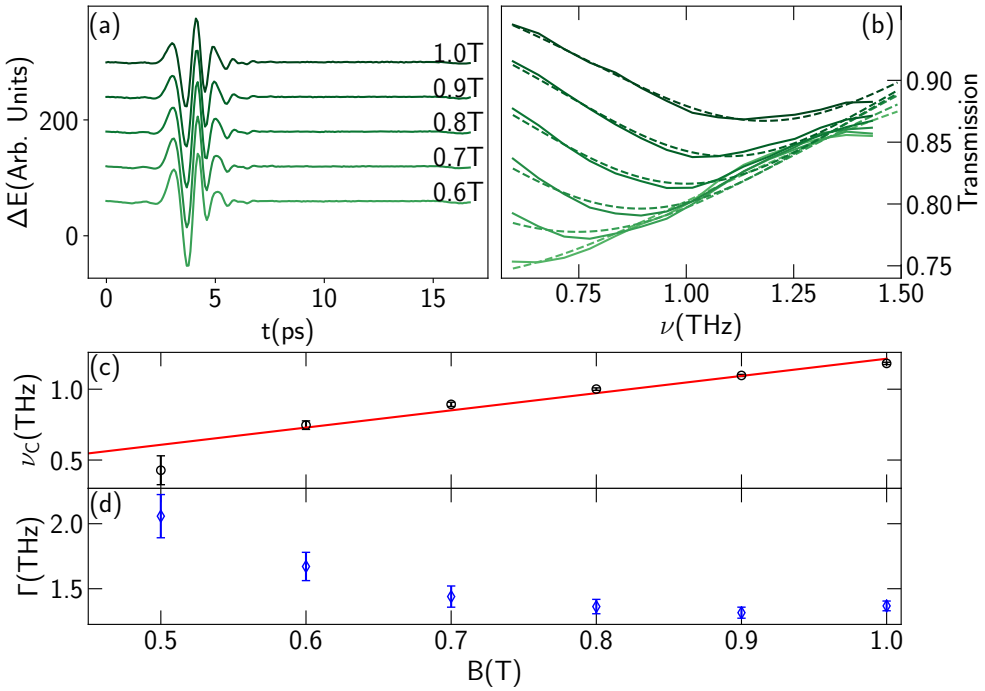

Figure 6.3: (Panel (a) reports the change in electric field induced by the pump under magnetic field. The oscillations induced by the cyclotron resonance are clearly visible. All the pulses have been shifted for clarity. (b) Transmission spectra (solid lines) clearly showing the cyclotron dip. The spectra correspond to different magnetic fields from 0.6 to 1T, they have been shifted upwards for clarity. The dotted lines represent fits with Lorentz functions. (c) cyclotron frequency versus magnetic field. These are the central frequency of the Lorentz fit. The red line is a fit of the cyclotron frequency. The corresponding obtained effective mass is m^*/m_0=0.0231±0.0006. The ν_0 parameter was fixed to 0. Panel (d) reports the linewidths, these are the Γ linwediths of the Lorentz fits in Equation 6.11.

expected given the larger bandgap of the alloy, and it is consistent with previous reports [187].

6.3.2 Mass change during rise of photoconductivity

Following the approach introduced in the previous chapters, the aim is now to study the carrier cooling of electrons in a semiconductor with an interesting, but relatively simple, bandstructure. The approach was to track carriers while they cooled down inside the band. Performing the experiment at 2 K allows the process to slow down due to the bigger difference in temperatures and the reduced scattering with phonon modes. As the rise of the photoconductivity onset became slower, this allowed spectra to be acquired during the rise, which is almost impossible in perovskites,

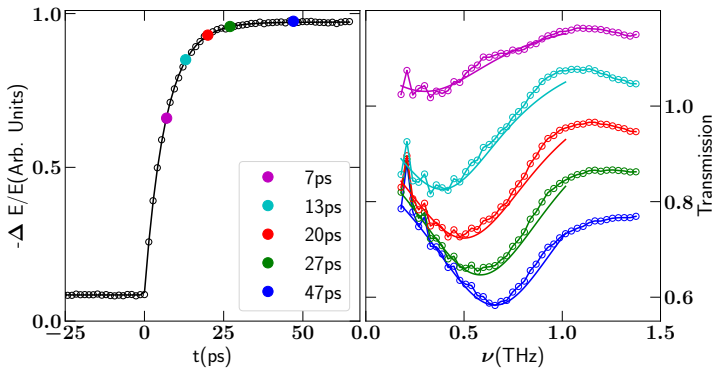

Figure 6.4: (a) plot of the onset of the pump-induced change in electric field (black circles) and exponential rise fit (black line). The coloured circles represent the time delays at which the transmission spectra in (b) were measured.(b) transmission spectra at different time delays after photoexcitation (coloured circles)along with Lorentzian fits of the cyclotron dips (coloured lines). The spectra were mesaured at a magnetic field of B=0.4 T.

since the rise takes around 1 ps at room temperature. The transmitted relative change in the peak of electric field is reported in Figure 6.4(a). The data (black circles) are plotted alongside the fit of the rise time, similar to the one reported for perovskites. This fit yielded τ=6.65±0.03 ps, which is, incidentally, much longer than the characteristic time of the THz pulse (around 300 fs). On top of this, the plot reports also the various time delays at which the spectrum was measured, in different colours, corresponding to the colours of the transmission spectra reported in Figure 6.4(b). Note also that the photoconductivity happens to be nonzero even at times before the pump pulse (*i.e.* $t < 0$). This was interpreted as carriers remaining from the previous photoexcitation pulse, about 200 μs before. During the course of the experiment care was taken to check that this wasn't affecting the measurements, which remained stable during the course of the day. In fact the choice of defining the transmission as $T = \frac{E_{on}(B)}{E_{off}(B)}$ ensures that the cyclotron resonances in the spectrum come only from the photoexcited carriers. In Figure 6.4(b) the transmission spectra are reported (circles) along with the fits of the dip in the transmission (using a Lorentzian model, Equation 6.11). From these fits it is possible to extract the effective mass value from the theory developed previously, via:

$$m^* = \frac{eB}{2\pi\nu_C}. \tag{6.14}$$

The values obtained from this analysis are then reported in Figure 6.5 for the different time delays. In the plot the theoretical value at the Γ point is also reported (red

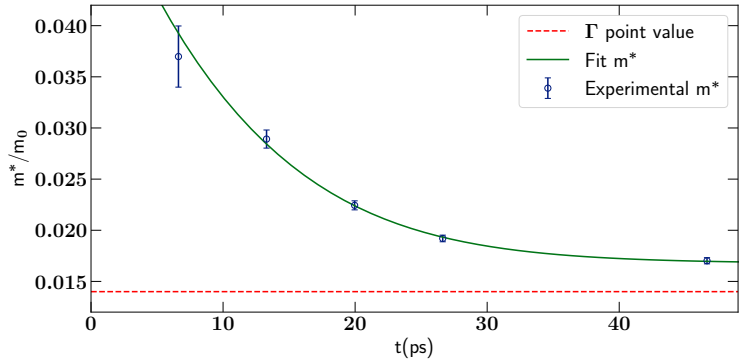

Figure 6.5: In this figure the effective mass obtained from the fits (blue circles) is plotted against the time after photoexcitation. The red dotted line represent the theoretical value at the Γ point. As it can be noticed the effective mass is always larger than this value and tends towards it during the rise time, however without reaching it in the considered time window. The green line is a fit with a model described in the text.

dotted line). From this plot seems clear that the effective mass is systematically larger than the band edge value and that it tends toward this value as time goes by, reaching it only in the limit of long times.

In order to describe this process it was attempted to fit the data in Figure 6.5 with the expression of the effective mass Equation 6.5. In this case the energy at which the measurement is performed is not fixed but changes with time, therefore it was modelled as follows. The excess energy injected was the pump energy 1.55 eV (800 nm) minus the band gap energy 0.24 eV (5.16 μm), and, given much lighter mass of electrons ($0.014m_0$), in respect to heavy holes ($0.43m_0$) it was assumed the energy was given mostly to electrons (it was assumed 90%): $\varepsilon_0 = 1.55 - 0.24 = 1.31 \cdot 0.9 = 1.2\,\text{eV}$. This excess energy is such that electrons have an energy that allows to access the X-valley and the L-valley. The possible sources of photoconductivity are: electrons in the Γ-valley, electrons in the side valleys and heavy holes. The L- and X-valleys have effective masses of $2.45m_0$ and $3.9m_0$ respectively [196], and, therefore, with a similar argument as for GaAs, their contribution to the total photoconductivity will be marginal as most of the photoconductivity signal will come from electrons in the Γ-valley rather than the side valleys. Moreover, electrons in the X- and L-valley could have a cyclotron resonance, but well outside the experimental range: an effective mass of $1m_0$, under a magnetic field of 0.4 T yields a CR of ∼9 GHz. With a similar reasoning, as the hole mobility is ten times lower than the electron mobility, it is possible to assume that most of the photoconductivity signal arises from electrons and that most of the cyclotron resonance signal during the rise

comes from electron in the Γ-valley.

To describe the change of energy with time it was assumed the electrons were losing energy in an exponential fashion:

$$\varepsilon(t) = \varepsilon_0 e^{-t/\tau_m} + \varepsilon_F, \tag{6.15}$$

where τ_m is the energy loss time, ε_F is the long time limit quasi-Fermi level at the injected carrier density, and ε_0 is the initial injected energy for electrons. Therefore, the change of mass with time can be expressed as:

$$m^*(t) = m_0^* \sqrt{1 + 4\alpha \left(\varepsilon_0 e^{-t/\tau_m} + \varepsilon_F\right)}. \tag{6.16}$$

The result of the fit (with both ε_0 and m_0^* kept constant) is reported in Figure 6.5 (continuous line). The curve seems to reproduce the results well and the output results are: α=3.2±0.5 eV^{-1}, ε_F=0.034±0.005 eV and τ_m=7.7±0.5 ps. These values are interesting for the following reasons. First the nonparabolicity constant is in relatively good agreement with the reported value of 4.1 eV^{-1}[191], given the simple model applied. The estimated Fermi level at this injection level is estimated to be relatively small, but enough to keep the effective mass higher than the Γ-point value, consistent with the measurement performed at a similar carrier density that will be presented in the next section. It is interesting to notice that from Equation 6.9 it is possible to estimate the number of injected carriers from the Fermi level, which is $7\times10^{16}cm^{-3}$. Finally, the energy relaxation time τ_m is compatible with the rise time measured from Figure 6.4, which supports the assumption that the rise in $\Delta E/E$ directly tracks the reduction in mass of the electrons.

6.4 Carrier density influences the effective mass

6.4.1 Effective mass at high fluence

Since the effective mass value obtained at low injection was higher then expected, attempts were made to investigate the possible causes. Differences in the carrier density are known to affect the measured effective mass [191] (given the strong material nonparabolicity) and so a second cyclotron spectroscopy experiment was performed with 10× higher incident power. The results are reported in Figure 6.6. The analysis was virtually identical to the one performed on the low fluence case. Unfortunately one of the effects of an higher fluence is an increase in the linewidth, which in turn washed out the dips at the higher end of the bandwidth in a way

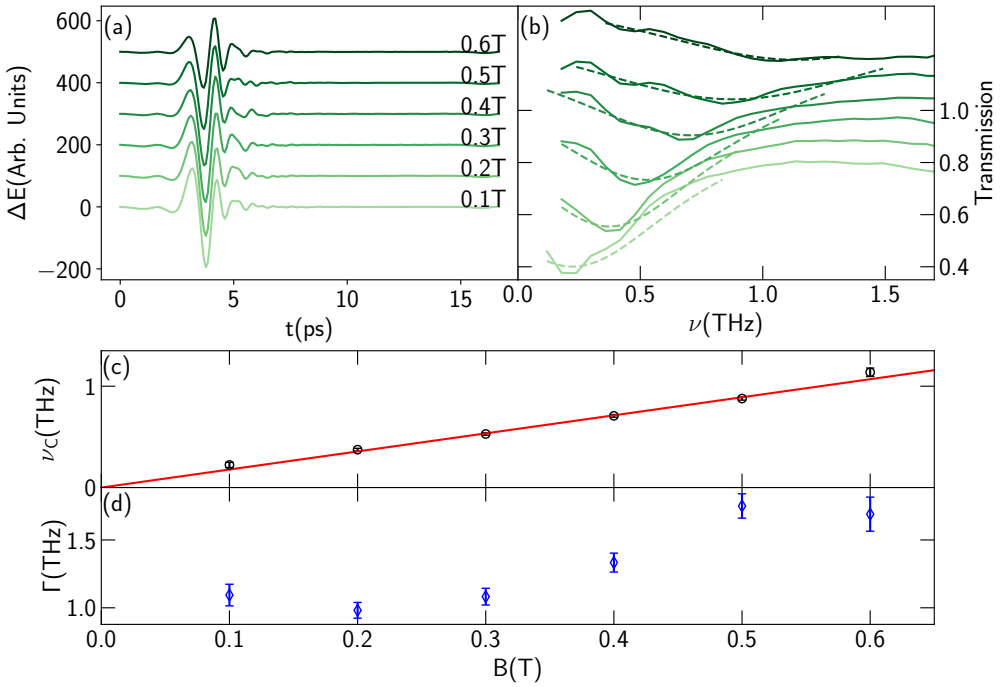

Figure 6.6: Panel (a) reports the time-domain change of electric field for different magnetic fields. Panel (b) reports the transmission spectra (solid lines) and corresponding Lorentz fits (dotted lines) for magnetic fields between 0.1 and 0.6T. Both time- and frequency-domain traces have been shifted upwards for clarity. The spectra at this fluence are more spread out and harder to detect at the edge of the bandwidth. Panel (c) reports the cyclotron frequencies versus the magnetic fields (black circles). The red line is a linear fit. The obtained effective mass is: m^*/m_0=0.01534±0.0003. The ν_0 parameter (Equation 6.12) was fixed to 0. Panel (d) reports the linewidth of the Lorentz fit. As can be seen these are wider than the low fluence case (Figure 6.2) and increasing with the magnetic field.

that made it impossible to use any magnetic field higher than 0.6 T. In panel (a) the time-domain traces are reported. The oscillations caused by the resonance are clearly visible, but they are shorter-lived than the corresponding data in Figure 6.2 (a). In panel (b) the spectra are reported (continuous lines) along with the Lorentzian fits (dotted lines). It is important to notice that in this case the range of the fit was limited around the main dip observed, to mitigate the effect of the more noisy data. It is possible to see how the transmission is lower than the low fluence cases (because more carriers have been excited) and the dips look broader and more spread out. In panel (c) the cyclotron frequencies are reported vs the magnetic field (black circles) along with a linear fit (red line)which well describes the data. the values obtained from this is: m^*/m_0=0.0154±0.0003. This value is very similar

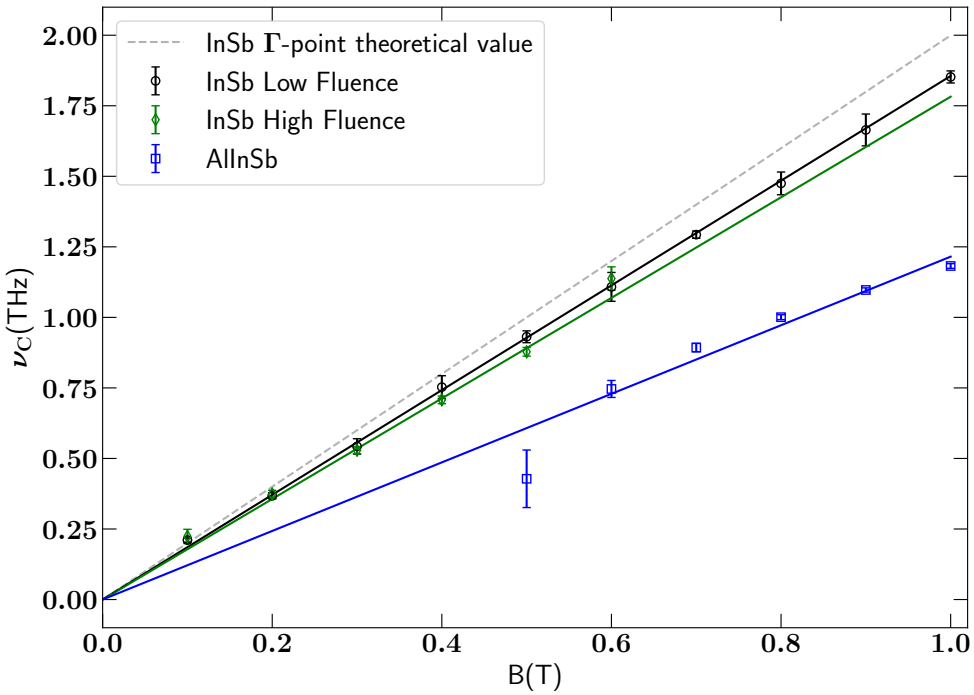

Figure 6.7: The figure reports the different cyclotron plots for InSb at low and high fluence (black circles and green diamonds respectively) and for $Al_{0.05}In_{0.95}Sb$ (Blue squares). The grey dotted line represents the expected Γ-point value of m^*/m_0=0.014.

to the low-fluence case, too close, in fact, to claim that the two are substantially different. However from the expression of the effective mass in Equation 6.5, one should expect, for a ten-fold increase in carrier density, a two or three-fold increase in the effective mass. A possible explanation for this apparent discrepancy is given at the end of the chapter. Panel (d) reports the linewidths against the magnetic field: as anticipated they look much broader than the low fluence case (five times bigger in the most extreme case) and slightly increasing with the field. This is possible in the case of short-range scattering potentials, where the linewidth goes as the square root of the magnetic field [197]. In Figure 6.7 the two sets of cyclotron frequencies (low and high fluence with black circles and green diamonds respectively), along with their corresponding fit lines, are reported and compared to $Al_{0.05}In_{0.95}Sb$ and with the expected value at the Γ-point (grey dotted line).

6.4.2 Effective mass at different fluences

Given the inconclusive results of the previous paragraphs and to establish a proof-of-principle that the effects of nonparabolicity can be measured by fluence-tuning

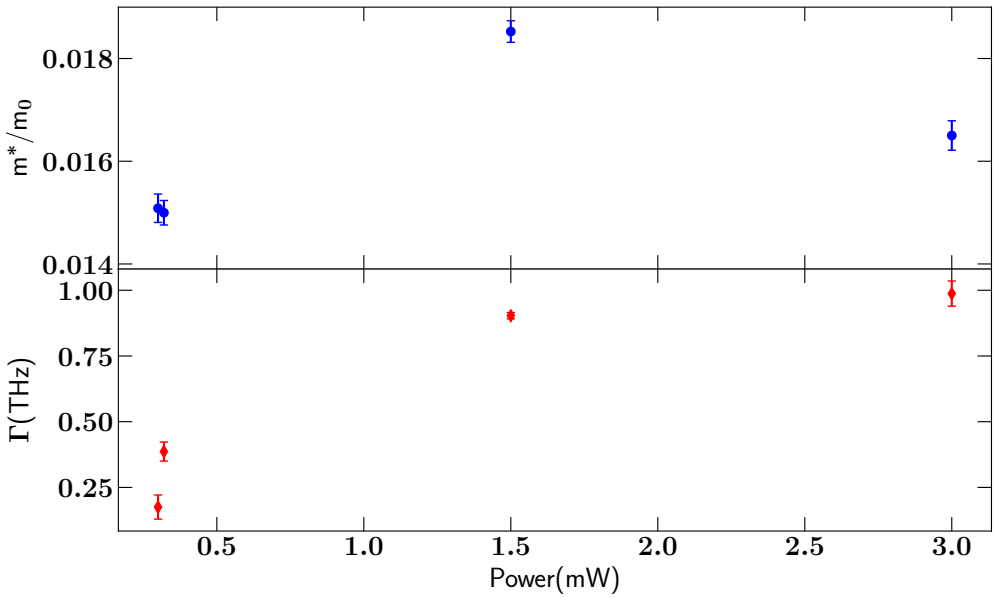

Figure 6.8: This plot reports the effective mass for InSb as obtained from transmission spectra at 0.4T by varying the incident power. (a) reports the effective mass where the two higher fluence points correspond to masses higer than the lower fluence points. (b) reports the linewidth at different fluences which get significantly bigger for higher fluence.

of cyclotron spectra, a few spectra were taken at 0.4 T at few different fluences to check if any clear trend appeared, all at the same time delay of 200 ps. These are reported in Figure 6.8. These spectra were acquired by fixing the magnetic field and changing the incident power. The 3mW value is not the same dataset as in Figure 6.6, and they all correspond to a single magnetic field. In panel (a) the effective mass is reported against fluence and appears to be small at 0.3mW of incident power, which significantly increases for the data at 1.5 and 3 mW incident power. Although the value at 3 mW seems to be lower than the 1.5mW one, but still higher than the low-fluence case. It is impossible to discern if this is a trend or an accident with the current set of data. The effective mass is known to increase with the carrier density in a non-linear fashion[191]. However the change observed seems to be smaller than what would be expected (if present at all) from previous studies [191]. The linewidth (panel (b)) instead increases substantially with increasing power. These results represent a proof-of-principle result that measuring the effect of nonparabolicity on the effective mass using cyclotron THz spectroscopy is likely possible. However the difference in the effective mass is not so striking and a more precise measurements are required. In the measurements performed during the rise,

however, the effect was much more pronounced. These contradictions are discussed in the final section.

6.5 Final discussion

This chapter was dedicated to the study of hot carriers in InSb and how the effective mass changes with time. A simple description of nonparabolicity and how it influences the conductivity was given. These results were then used to interpret the change in effective mass measured with cyclotron spectroscopy during the onset of photoconductivity, and the change in effective mass with a different position of the Fermi level. The measurements of the mass change during the rise of the photoconductivity is in reasonable agreement with the simple nonparabolic description of the bandstructure. The fluence-dependent measurements, instead, provided a proof-of-principle that the fluence-tuning of the effective mass is likely possible. However the results remain preliminary, as the difference observed is very small (Figure 6.7), or sometimes contradictory(Figure 6.8). Carrier-density tuning of the effective mass is something that is known to happen in InSb[191], but it was not possible to observe it to such a degree in the experiments performed in this thesis. A possible explanation for this discrepancies could be due to an error in the amount of injected carriers, specifically it could be due to diffusion through the bulk of the semiconductor. InSb, notoriously, has a very high mobility[188], which, assuming a simple Einstein relation for diffusion: $D = \frac{\mu_e k_B T}{e}$[2] (where D is the diffusivity, μ_e is the electron mobility, k_B is the Boltzmann constant and T the temperature), yield a very high diffusivity. Since most of the CR experiments performed in this chapter were taken around 200 ps after injection, diffusion through the bulk may have reduced the actual carrier density. To test if the values are reasonable the theoretical effective mass for a given injected carrier density was calculated. The result is reported in Figure 6.9. The figure shows how for a relatively low carrier density, as the one used in these experiment (from the rise time fit it was estimated to be around $7{\cdot}10^{16}\mathrm{cm}^{-3}$), the effective mass is still only slightly heavier than the Γ point value, in fact it is consistent that the change between the two fluences was relatively small. This calculation is very similar to the one performed by Zawadzki [191], however there are some important differences: in that work the effective mass was calculated to change as $m^* = m_0^*(1 + 2\alpha\varepsilon)$, which is a more approximated version than the expression calculated in Equation 6.5. This is crucial as the results of Figure 6.8 seem to suggest that the change of effective mass with the carrier density are not pronounced at the injection level typical of OPTP experiments (around

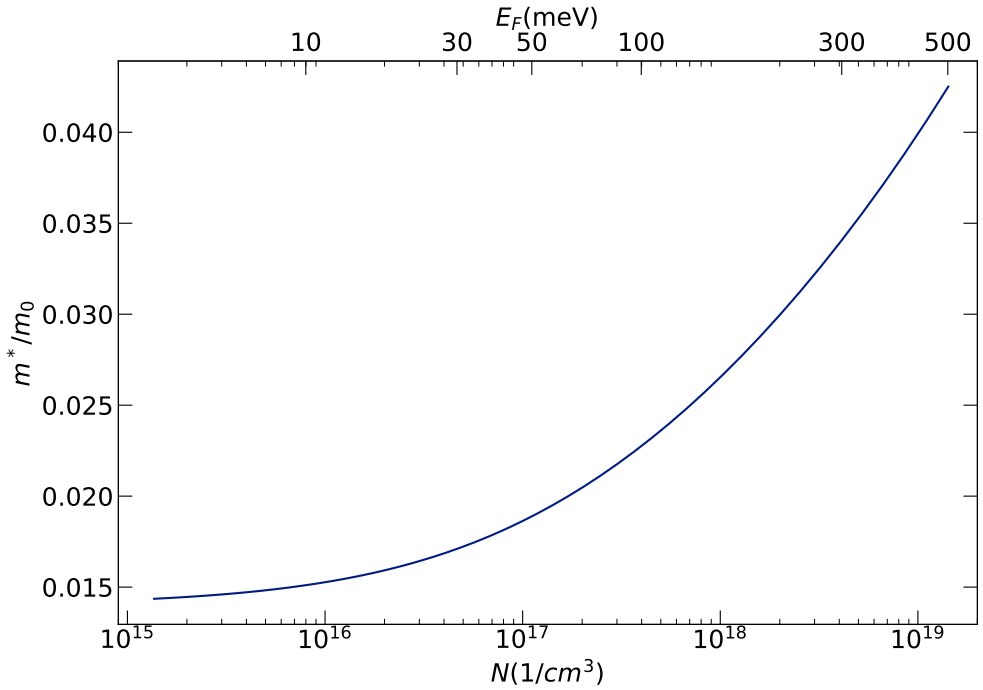

Figure 6.9: Calculated effective mass for a given injected carrier density using the theory developed at the beginning. This was calculated assuming a nonparabolicity constant of 4.1 eV^{-1}, and calculating the injected carrier density from Equation 6.9.

10^{16}cm^{-3} for these experiments). Although the role of diffusion can not be ruled out altogether.

It has to be said, however, that this work consisted in a preliminary study, providing a proof-of-principle that THz cyclotron spectroscopy is indeed capable of studying the effective mass in InSb, and a more detailed study is needed. A way the results could be improved, especially in light of the results in Figure 6.9, is by 1) choosing a wider range of fluences in the higher end and by 2) performing accurate measurements with magnetic field sweeps at each chosen fluence. This way a study similar to the one in section 6.4 could be done more effectively.

In the end, it can be concluded that THz cyclotron spectroscopy is indeed capable of measuring the effective mass of InSb and its compounds, and it is sensitive enough to measure changes in the effective mass induced by the peculiar bandstructure in InSb.

Chapter 7

Conclusion

This thesis has reported advances in the study of the hot carrier (HC) dynamics in metal halide perovskites (MHP) and III-V semiconductors. The work was motivated by the potential that MHP have shown as hot carrier solar cell (HCSC) absorbers, and the general outstanding photovoltaic properties they have shown.

Chapter 1 provided the relevant background information for the understanding of the relevant concepts discussed later, as well as outlining the motivation for the work.

Chapter 2 provided a description of the experimental methods used in this thesis: optical pump terahertz probe spectroscopy (OPTP), transient absorption spectroscopy (TA), and THz cyclotron spectroscopy (TCS) were described and the information that they allow to extract outlined.

Chapter 3 presented a new phenomenological model to describe the hot carrier cooling (HCC) phenomenon. Firstly the physical basis of the hot phonon bottleneck (HPB) mechanism was introduced, along with the influence of Auger processes in the heating of hot carriers. After that, the proposed three-temperature model (TTM) was outlined, first in its full form including Auger heating, then in its simplified form. The physical meaning behind the coupling rates was described by showing their influence on the overall temperature dynamic. The interpretations of the two main regimes as dominated by the Fröhlich interaction (the first regime) and by phonon-phonon interaction (the second) were then presented along with simplified models to link the experimental parameters to the underlying fundamental processes.

Chapter 4 presented a study of HCC in Sn-based perovskites. First the quality of Br-substitution on the PV performance was assessed by estimating the diffusion length from the mobility and recombination time measured with OPTP. After

that, the complex anisotropic multi-band bandstructure of $CsSnI_3$ was established by a combination of DFT calculations and PL spectroscopy. These observations were used to interpret the energy-dependence of the HCC time, which showed an abrupt change at the energy corresponding to a second band transition. This represented a marked difference with the GaAs case, which showed strong influence of inter-valley scattering. The HCC time at low injection energies was then modelled with the Fröhlich model developed in the previous chapter and found consistent semi-quantitative results for both GaAs and $CsSnI_3$ suggesting the common assumption of polar scattering dominating the first stage of HCC is correct. The influence of the bandstructure was the primary cause for a long Fröhlich cooling time, which could explain some of the observations in the literature regarding Sn-based perovskites.

Chapter 5 presented a systematic study of a $Cs_{0.05}(FA_{0.83}MA_{0.17})_{0.95}Pb_xSn_{1-x}I_3$ sample series with x=0, 0.25, 0.5, 0.75 and 1. The chapter briefly presented basic characterisations as PL spectroscopy and absorbance to identify the band gap and fraction of absorbed carriers at each wavelength important to estimate the excess energy and the mobility respectively. Once the static spectroscopy techniques established the successful formation of mixed lead-tin compositions, OPTP was used to measure the mobility and the intraband carrier cooling time at different excess energies. The mobility was higher and relatively constant for the samples with $x \geq 0.5$ and minimum for the sample with x=0.25. The carrier cooling time was found to be minimum for x=0.25 in all cases, and to be generally smaller for mixed compounds at low excess energies, but more scattered for higher excess energies, were the complex bandstructure might play a role. TA was then performed on the sample with x=0, 0.5, 1.0, and the full temperature dynamics was extracted, showing the common two-regimes HPB cooling curves. The two techniques were then compared showing that at similar fluences and excess energies OPTP is only sensitive to the first stage of cooling, dominated by the Fröhlich interaction, while TA, although more complex to model and interpret, is capable to describe the whole temperature dynamics, solving some discrepancies in the literature, and also suggesting that the mobility of the carriers in the HPB regime is very similar to the mobility of cold carriers. By comparing the samples it was observed that the mixed lead-tin sample showed a longer cooling time in the HPB-dominated regime, which was attributed to a suppression of the phonon-phonon coupling compared to the "pure" compounds. The alloying directly affects the lowest LO phonon modes, as they correspond to the cage modes and the Pb-I bonds, which are modified by the metal substitution with Sn. Finally a sample with substituted bromine was studied, showing a more pronounced Auger effect

(although at higher carrier density) and a electron-phonon and phonon-phonon coupling rates showing a stronger electron-phonon coupling and a phonon-phonon coupling similar to the full lead sample without bromine. This chapter's results strongly suggest that some inconsistencies in the literature might be caused by a wrong interpretation of the results: the two cooling regimes are affected differently by experimental parameters as the compositions, excess energy and carrier density, as such if techniques that are sensitive only to one stage are used this could induce misinterpretations.

The last chapter presented a different approach on the study of HCC on a much simpler and better-studied sample, InSb. The approach consistent in studying cyclotron resonances in the THz to measure the effective mass in different conditions of carrier density and band energy. The effective mass of InSb and $Al_{0.05}In_{0.95}Sb$ were measured and found to be consistent with previous reports. Cyclotron resonances were then measured during the rise of the change in electric field and the resulting effective mass showed a marked time dependence, attributed to its dependence on the band energy at which the electrons were at that time delay. The results were then successfully modelled with a simple nonparabolic description of band curvature. Measurements of the effective mass at higher fluence resulted in an effective mass only marginally higher than the low fluence case, this could be explained by the fact that the range of carrier density used is still too low to produce a significant difference, or by a reduction of carrier density caused by diffusion, which is expected to be quite fast given the high mobility.

7.1 Outlook and Future work

The work reported here tried to provide a systematic study of the HCC in MHP, probably opening more questions than it answered. As discussed in chapter 5 the parameter space defined by the HC phenomenon is really wide. In light of the observations regarding the technique outcome in chapter 5 it would be interesting to observe the full cooling dynamic of an inorganic tin perovskite or samples that have not been investigated this way in the past, checking whether the some of the conclusions reached in the last years of work hold. The work in chapter 5 also established a strong influence of the metal on the phonon-phonon interaction, it could be interesting to give a more complete study on the influence of the halide, by studying systematically I-Br mixed compounds, in the same way it was done in the metal case. Recently interest in HCC in mixed-halide perovskites has shown to be relevant [113].

The work done here focused on an intermediate regime of energies, where the HPB dominates, however it should be interesting to repeat similar studies (changing the composition and excess energy, for example) carefully tuning the fluence, to observe the emergence of different regimes, like the Auger-dominated one, or the polaronic effects emerging at lower carrier densities which in this work have been neglected for simplicity.

Few steps could be done towards the realization of practical hot carrier solar cells (HCSC), which would start from the design and realization of suitable energy selective contacts compatible with MHP. In this respect ultrafast spectroscopy techniques could be useful in studying the charge transfer of such structures.

Aside from the HC dynamics, the role of ultrafast spectroscopy in the field of MHP is not exhausted yet. The valuable information provided by both OPTP and TAS will be of paramount importance in future research. The mechanism behind the low defect sensitivity in perovskites is not fully understood and will require more work to be completely studied, same goes for the mechanisms behind degradation. The consequences the polaronic nature of charges has in solar cell devices is not clear yet, and ultrafast techniques would be helpful in studying the physics of polaron formation, their mobility and transport properties. Studying the spin-orbit coupling physics and the effective mass of MHP using terahertz cyclotron spectroscopy could provide interesting informations. Great interest could have the study of more exotic structures as quasi-2D perovskites and double perovskites as well as perovskite nanocrystals. Finally great interest is rising in understanding the mechanisms of charge transfer between perovskite films and extraction layers or between interfaces, for example 2D/3D perovskite structure have reached great stability, however the role of the interface in controlling the stability is still an open question[198].

The work in chapter 6 was preliminary and as such could easily be extended by performing more accurate measurements, with more magnetic field points, and on a bigger range of fluences, especially in the higher end. InSb and related materials have shown promising properties both in the field of spintronics and in the realization of nanostructures, as quantum wells[199, 200] and nanowires[201, 202]. Especially THz measurements could allow a more in-depth study of the properties of such heterostructures, by studying the momentum scattering time (and consequently the mobility) or by performing cyclotron measurements aimed at accurately measuring the g-factor, the strong spin-orbit coupling of InSb or the width of the Landau levels.

Appendix A

Calculation of Boltzmann conductivity and other quantities for a nonparabolic band

A.1 Effective mass change with energy

This shows the calculations to recover the expression for the effective mass in eq. 6.5. Knowing that:

$$\varepsilon_c(k) = -\frac{1}{2\alpha} + \frac{1}{2\alpha}\sqrt{1 + 2\alpha\frac{\hbar^2 k^2}{m_0^*}}, \tag{A.1}$$

then the effective mass can be calculated as:

$$\frac{1}{m^*} = \frac{1}{\hbar^2 k}\frac{d\varepsilon}{dk}. \tag{A.2}$$

Therefore:

$$m^* = \frac{\hbar k}{\frac{1}{\hbar}\frac{d\varepsilon}{dk}}. \tag{A.3}$$

Since:

$$\frac{d\varepsilon_c}{dk} = \frac{1}{2\alpha} \frac{\frac{2\hbar^2}{m_0^*} 2\alpha k}{\sqrt{1 + 2\alpha \frac{\hbar^2 k^2}{m_0^*}}} \tag{A.4}$$

$$= \frac{\frac{2\hbar^2 k}{m_0^*}}{\sqrt{1 + 2\alpha \frac{\hbar^2 k^2}{m_0^*}}}. \tag{A.5}$$

Then:

$$m^* = \sqrt{1 + 4\varepsilon\alpha}. \tag{A.6}$$

A.2 Density of states

Here a calculation of the expression for the density of states (DOS), given in eq. 6.4, is provided. Starting from the definition of nonparabolicity in eq. 6.2:

$$\frac{\hbar^2 k^2}{2m_0^*} \simeq \varepsilon \left(1 + \alpha\varepsilon\right), \tag{A.7}$$

it can be solved for k:

$$k = \sqrt{\frac{2m_0^*}{\hbar^2} \left(\alpha\varepsilon^2 + \varepsilon\right)}. \tag{A.8}$$

The volume of occupied states is:

$$\Omega(\varepsilon) = \frac{4\pi}{3} k^3 = \frac{4\pi}{3} \left[\frac{2m_0^*}{\hbar^2} \left(\alpha\varepsilon^2 + \varepsilon\right)\right]^{3/2}. \tag{A.9}$$

Therefore the density of states is:

$$D(\varepsilon) = \frac{d\Omega(\varepsilon)}{d\varepsilon} = 2\pi \left(\frac{2m_0^*}{\hbar^2}\right)^{3/2} \left(\alpha\varepsilon^2 + \varepsilon\right)^{1/2} \left(2\alpha\varepsilon + 1\right), \tag{A.10}$$

and including the pre-factor $\frac{g_s}{V_k} = \frac{1}{4\pi^2}$, which includes the spin degeneracy[2] the final expression is:

$$g(\varepsilon) = \frac{1}{2\pi} \left(\frac{2m_0^*}{\hbar^2}\right)^{3/2} \left(\alpha\varepsilon^2 + \varepsilon\right)^{1/2} \left(2\alpha\varepsilon + 1\right). \tag{A.11}$$

A.3 Boltzmann conductivity

The Boltzmann conductivity equation in case of a generic metal or semiconductor can be expressed as:

$$\sigma(\boldsymbol{q},\omega) = \frac{e^2}{4\pi^3}\int_{\boldsymbol{k}} \frac{\tau(\hat{e}\cdot\boldsymbol{v})^2}{1-i\tau(\omega-\boldsymbol{q}\cdot\boldsymbol{v})}\left(-\frac{\partial f_0}{\partial\varepsilon}\right)_{\mu} d\boldsymbol{k}, \tag{A.12}$$

where τ is the momentum scattering time, $\hat{e}$ is the polarization vector, $\boldsymbol{v}$ is the electron velocity, ω is the angular frequency, $\boldsymbol{q}$ is the wavevector and f_0 is the Fermi-Dirac distribution, whose derivative is calculated at the quasi-chemical potential μ. The integral is extended across the whole k-space. From this, assuming the limit of long wavelengths (correct, for most THz applications):

$$\sigma(\omega) = \frac{e^2}{4\pi^3}\int_{\boldsymbol{k}} \frac{\tau(\hat{e}\cdot\boldsymbol{v})^2}{1-i\tau\omega}\left(-\frac{\partial f_0}{\partial\varepsilon}\right)_{\mu} d\boldsymbol{k}, \tag{A.13}$$

which is the form that has been used in the past to implement conductivity models starting from an energy dependent τ [193]. The long-wavelength approximation can be justified by the following argument: for a THz beam of frequency ν ∼1 THz, the absolute value of the wavevector is $q = \frac{2\pi}{\lambda}$, with λ ∼300 μm. From eq A.16 the velocity can be estimated to be around $\sim 7\cdot10^5$, then the product of the wavevector times the velocity is much smaller than the light frequency:$q\cdot v \sim 1\cdot10^{10}$ Hz$\ll$ 1 THz.

Assuming a polarization along x:

$$\sigma(\omega) = \frac{e^2}{4\pi^3}\int_{\boldsymbol{k}} \frac{\tau v_x^2}{1-i\tau\omega}\left(-\frac{\partial f_0}{\partial\varepsilon}\right)_{\mu} d\boldsymbol{k}. \tag{A.14}$$

In this formula the bandstructure is implicitly inserted in v_x^2. Knowing that:

$$v = \frac{1}{\hbar}\frac{\partial\varepsilon_c}{\partial k}, \tag{A.15}$$

an expression for v^2 is readily found from:

$$v = \frac{\hbar k/m_0^*}{\sqrt{1+2\alpha\frac{\hbar^2k^2}{m_0^*}}}, \tag{A.16}$$

$$v^2 = \frac{\hbar^2k^2/m_0^{*2}}{1+2\alpha\frac{\hbar^2k^2}{m_0^*}}. \tag{A.17}$$

with m_0^* the effective mass at the Γ point and α the nonparabolicity constant. Using these expressions and changing variables to the spherical coordinate system:

$$\sigma(\omega) = \frac{e^2}{4\pi^3}\int_0^\infty k^2 dk \int_0^\pi \sin\theta d\theta \int_0^{2\pi} d\phi \frac{\tau v^2 \sin^2\theta\cos^2\phi}{1-i\omega\tau}\left(-\frac{\partial f_0}{\partial\varepsilon}\right)_\mu, \tag{A.18}$$

$$= \frac{e^2}{4\pi^3}\pi\frac{4}{3}\int_0^\infty k^2 dk \frac{\tau v^2}{1-i\omega\tau}\left(-\frac{\partial f_0}{\partial\varepsilon}\right)_\mu, \tag{A.19}$$

$$= \frac{e^2}{3\pi^2}\int_0^\infty k^2 dk \frac{\tau}{1-i\omega\tau}\frac{\hbar^2k^2/m_0^{*2}}{1+2\alpha\frac{\hbar^2k^2}{m_0^*}}\left(-\frac{\partial f_0}{\partial\varepsilon}\right)_\mu, \tag{A.20}$$

where v_x was expressed in terms of $v_x = v\sin\theta\cos\phi$ and the integrals over θ and ϕ are equal to $\frac{4}{3}\pi$. Changing variable and expressing k in terms of energy:

$$\varepsilon + \alpha\varepsilon^2 = \frac{\hbar^2k^2}{2m_0^*}, \tag{A.21}$$

from which the previous equation simplifies to:

$$\sigma(\omega) = \frac{e^2}{3\pi^2}\int_0^\infty \frac{\tau}{1-i\omega\tau}\frac{\left[\frac{2m_0^*}{\hbar^2}\left(\varepsilon+\varepsilon^2\alpha\right)\right]^{3/2}}{\sqrt{1+4\alpha\varepsilon+4\alpha^2\varepsilon^2}}\left(-\frac{\partial f_0}{\partial\varepsilon}\right)_\mu\frac{d\varepsilon}{\hbar^2}, \tag{A.22}$$

$$= \frac{e^2}{3\pi^2}\frac{\sqrt{2m_0^*}}{\hbar^3}\int_0^\infty \frac{\tau}{1-i\omega\tau}\varepsilon^{3/2}\frac{(1+\varepsilon\alpha)^{3/2}}{\sqrt{1+4\alpha\varepsilon+4\alpha^2\varepsilon^2}}\left(-\frac{\partial f_0}{\partial\varepsilon}\right)_\mu d\varepsilon. \tag{A.23}$$

In the limit of T→0 K, the derivative of f_0 tends to a delta function, which means the integral is evaluated only at the Fermi surface:

$$\sigma(\omega) = \frac{e^2}{3\pi^2}\frac{\sqrt{2m_0^*}}{\hbar^3}\frac{\tau(\varepsilon_F)}{1-i\omega\tau(\varepsilon_F)}\varepsilon_F^{3/2}\frac{(1+\varepsilon_F\alpha)^{3/2}}{\sqrt{1+4\alpha\varepsilon_F+4\alpha^2\varepsilon_F^2}}. \tag{A.24}$$

Now defining:

$$N^* = \frac{1}{6\pi^2}\left(\frac{2m_0^*}{\hbar^6}\right)^{3/2}\varepsilon_F^{3/2}(1+\alpha\varepsilon_F)^{3/2}, \tag{A.25}$$

and recalling the expression for the effective mass A.6, and neglecting the term $\alpha^2\varepsilon_F^2$ in eq. A.24 (which is higher order in $\alpha\varepsilon$), then eq. A.24 can be rewritten as:

$$\sigma(\omega) = \frac{N^*e^2}{m^*}\frac{\tau(\varepsilon_F)}{1-i\omega\tau(\varepsilon_F)}, \tag{A.26}$$

as presented in Equation 6.10.

Bibliography

[1] E. Becquerel: Mémoire sur les effets électriques produits sous l'influence des rayons solaires. *Comptes Rendus de l'Académie des Sciences*, 9:561–567, 1839.

[2] P. Y. Yu and M. Cardona: *Fundamentals of semiconductors*, volume 28. Springer-Verlag, fourth edition, 2010. ISBN 9783642007095. doi:10.1016/j.msec.2007.10.028.

[3] P. Würfel: *Physics of solar cells*. Wiley-VCH, 1st edition, 2005.

[4] J. Bisquert: *The physics of solar cells*. Taylor Francis Group, 1st edition, 2018. ISBN 9781138099968. doi:10.1002/9781119033769.ch5.

[5] T. Kirchartz, T. Markvart, U. Rau, and D. A. Egger: Impact of small phonon energies on the charge-carrier lifetimes in metal-halide perovskites. *Journal of Physical Chemistry Letters*, 9(5):939–946, 2018. ISSN 19487185. doi:10.1021/acs.jpclett.7b03414.

[6] S. Byrnes: GitHub repository. URL https://github.com/sbyrnes321/SolarCellEfficiencyLimits.

[7] W. Shockley and H. J. Queisser: Detailed balance limit of efficiency of p-n junction solar cells. *Journal of Applied Physics*, 32(3):510–519, 1961. ISSN 00218979. doi:10.1063/1.1736034.

[8] L. C. Hirst and E. J. Ekins-Daukes: Fundamental losses in solar cells. *Progress in photovoltaics: research and applications*, 19:286–293, 2011. doi:10.1002/pip.

[9] O. E. Semonin, J. M. Luther, S. Choi, H. Y. Chen, J. Gao, A. J. Nozik, and M. C. Beard: Peak external photocurrent quantum efficiency exceeding 100% via MEG in a quantum dot solar cell. *Science*, 334(6062):1530–1533, 2011. ISSN 10959203. doi:10.1126/science.1209845.

[10] B. Ehrler, M. W. Wilson, A. Rao, R. H. Friend, and N. C. Greenham: Singlet exciton fission-sensitized infrared quantum dot solar cells. *Nano Letters*, 12(2):1053–1057, 2012. ISSN 15306984. doi:10.1021/nl204297u.

[11] K. Tanabe: A review of ultrahigh efficiency III-V semiconductor compound solar cells: Multijunction tandem, lower dimensional, photonic up/down conversion and plasmonic nanometallic structures. *Energies*, 2(3):504–530, 2009. ISSN 19961073. doi:10.3390/en20300504.

[12] R. T. Ross and A. J. Nozik: Efficiency of hot-carrier solar energy converters. *Journal of Applied Physics*, 53(5):3813–3818, 1982. ISSN 00218979. doi:10.1063/1.331124.

[13] P. Würfel, A. S. Brown, T. E. Humphrey, and M. A. Green: Particle conservation in the hot-carrier solar cell. *Progress in Photovoltaics: Research and Applications*, 13(4):277–285, 2005. ISSN 10627995. doi:10.1002/pip.584.

[14] S. Kahmann and M. A. Loi: Hot carrier solar cells and the potential of perovskites for breaking the ShockleyQueisser limit. *Journal of Materials Chemistry C*, 2019. ISSN 2050-7526. doi:10.1039/C8TC04641G. URL http://xlink.rsc.org/?DOI=C8TC04641G.

[15] T. Kirchartz, L. Krückemeier, and E. L. Unger: Research update : recombination and open-circuit voltage in lead-halide perovskites. *APl Materials*, 6:100702, 2018. doi:10.1063/1.5052164.

[16] U. Rau: Reciprocity relation between photovoltaic quantum efficiency and electroluminescent emission of solar cells. *Physical Review B - Condensed Matter and Materials Physics*, 76(8):1–8, 2007. ISSN 10980121. doi:10.1103/PhysRevB.76.085303.

[17] W. Shockley and W. T. Read: Statistics of the recombination of holes and electrons. *Physical Review*, 87(5):835–842, 1952.

[18] R. Hall: Electron-hole recombination in germanium. *Physical Review*, 87:387, 1952.

[19] A. Kojima, K. Teshima, Y. Shirai, and T. Miyasaka: Organometal halide perovskites as visible-light sensitizers for photovoltaic cells. *Journal of the American Chemical Society*, 131(17):6050–6051, 2009. ISSN 00027863. doi:10.1021/ja809598r.

[20] M. M. Lee, J. Teuscher, T. Miyasaka, T. N. Murakami, and H. J. Snaith: Efficient hybrid solar cells based on meso-superstructured organometal halide perovskites. *Science*, 338(6107):643–647, 2012. ISSN 10959203. doi:10.1126/science.1228604.

[21] C. Wehrenfennig, M. Liu, H. J. Snaith, M. B. Johnston, and L. M. Herz: Homogeneous emission line broadening in the organo lead halide perovskite $CH_3NH_3PbI_{3-x}Cl_x$. *Journal of Physical Chemistry Letters*, 5(8):1300–1306, 2014. ISSN 19487185. doi:10.1021/jz500434p.

[22] S. De Wolf, J. Holovsky, S. J. Moon, P. Löper, B. Niesen, M. Ledinsky, F. J. Haug, J. H. Yum, and C. Ballif: Organometallic halide perovskites: Sharp optical absorption edge and its relation to photovoltaic performance. *Journal of Physical Chemistry Letters*, 5(6):1035–1039, 2014. ISSN 19487185. doi:10.1021/jz500279b.

[23] C. Wehrenfennig, G. E. Eperon, M. B. Johnston, H. J. Snaith, and L. M. Herz: High charge carrier mobilities and lifetimes in organolead trihalide perovskites. *Advanced Materials*, 26(10):1584–1589, 2014. ISSN 15214095. doi:10.1002/adma.201305172.

[24] S. D. Stranks, G. E. Eperon, G. Grancini, C. Menelaou, M. J. Alcocer, T. Leijtens, L. M. Herz, A. Petrozza, and H. J. Snaith: Electron-hole diffusion lengths exceeding 1 micrometer in an organometal trihalide perovskite absorber. *Science*, 342(6156):341–344, 2013. ISSN 10959203. doi:10.1126/science.1243982.

[25] Y. Bi, E. M. Hutter, Y. Fang, Q. Dong, J. Huang, and T. J. Savenije: Charge carrier lifetimes exceeding 15 μs in methylammonium lead Iodide single crystals. *Journal of Physical Chemistry Letters*, 7(5):923–928, 2016. ISSN 19487185. doi:10.1021/acs.jpclett.6b00269.

[26] D. A. Egger, A. Bera, D. Cahen, G. Hodes, T. Kirchartz, L. Kronik, R. Lovrincic, A. M. Rappe, D. R. Reichman, and O. Yaffe: What remains unexplained about the properties of halide perovskites? *Advanced Materials*, 30(20):1–11, 2018. ISSN 15214095. doi:10.1002/adma.201800691.

[27] F. Brivio, J. M. Frost, J. M. Skelton, A. J. Jackson, O. J. Weber, M. T. Weller, A. R. Goni, A. M. A. Leguy, P. R. F. Barnes, and A. Walsh: Lattice dynamics and vibrational spectra of the orthorhombic , tetragonal , and cubic

phases of methylammonium lead iodide. *Phys. Rev. B*, 92:144308, 2015. doi: 10.1103/PhysRevB.92.144308.

[28] A. Létoublon, S. Paofai, B. Rufflé, P. Bourges, B. Hehlen, T. Michel, C. Ecolivet, O. Durand, S. Cordier, C. Katan, and J. Even: Elastic constants, optical phonons, and molecular relaxations in the high temperature plastic phase of the $CH_3NH_3PbBr_3$ hybrid perovskite. *Journal of Physical Chemistry Letters*, 7(19):3776–3784, 2016. ISSN 19487185. doi:10.1021/acs.jpclett.6b01709.

[29] Q. Sun, X. Liu, J. Cao, R. I. Stantchev, Y. Zhou, X. Chen, E. P. Parrott, J. Lloyd-Hughes, N. Zhao, and E. Pickwell-MacPherson: Highly sensitive terahertz thin-film total internal reflection spectroscopy reveals in situ photoinduced structural changes in methylammonium lead halide Perovskites. *Journal of Physical Chemistry C*, 122(30):17552–17558, 2018. ISSN 19327455. doi:10.1021/acs.jpcc.8b05695.

[30] L. M. Herz: Charge-carrier mobilities in metal halide perovskites: fundamental mechanisms and limits. 2017. doi:10.1021/acsenergylett.7b00276. URL http://pubs.acs.org/doi/10.1021/acsenergylett.7b00276.

[31] W. J. Yin, T. Shi, and Y. Yan: Unusual defect physics in $CH_3NH_3PbI_3$ perovskite solar cell absorber. *Applied Physics Letters*, 104(6), 2014. ISSN 00036951. doi:10.1063/1.4864778.

[32] A. Zakutayev, C. M. Caskey, A. N. Fioretti, D. S. Ginley, J. Vidal, V. Stevanovic, E. Tea, and S. Lany: Defect tolerant semiconductors for solar energy conversion. *Journal of Physical Chemistry Letters*, 5(7):1117–1125, 2014. ISSN 19487185. doi:10.1021/jz5001787.

[33] J. Berry, T. Buonassisi, D. A. Egger, G. Hodes, L. Kronik, Y. L. Loo, I. Lubomirsky, S. R. Marder, Y. Mastai, J. S. Miller, D. B. Mitzi, Y. Paz, A. M. Rappe, I. Riess, B. Rybtchinski, O. Stafsudd, V. Stevanovic, M. F. Toney, D. Zitoun, A. Kahn, D. Ginley, and D. Cahen: Hybrid organic-inorganic perovskites (HOIPs): opportunities and challenges. *Advanced Materials*, 27(35):5102–5112, 2015. ISSN 15214095. doi:10.1002/adma.201502294.

[34] R. E. Brandt, V. Stevanović, D. S. Ginley, and T. Buonassisi: Identifying defect-tolerant semiconductors with high minority-carrier lifetimes: Beyond hybrid lead halide perovskites. *MRS Communications*, 5(2):265–275, 2015. ISSN 21596867. doi:10.1557/mrc.2015.26.

[35] M. Grätzel: The light and shade of perovskite solar cells. *Nature Materials*, 13(9):838–842, 2014. ISSN 14764660. doi:10.1038/nmat4065. URL http://www.nature.com/articles/nmat4065.

[36] M. A. Green, A. Ho-Baillie, and H. J. Snaith: The emergence of perovskite solar cells. *Nature Photonics*, 8(7):506–514, 2014. ISSN 17494893. doi:10.1038/nphoton.2014.134.

[37] C. Eames, J. M. Frost, P. R. Barnes, B. C. O'Regan, A. Walsh, and M. S. Islam: Ionic transport in hybrid lead iodide perovskite solar cells. *Nature Communications*, 6(May):2–9, 2015. ISSN 20411723. doi:10.1038/ncomms8497.

[38] C. Li, X. Lu, W. Ding, L. Feng, Y. Gao, and Z. Guo: Formability of ABX 3 (X = F, Cl, Br, I) halide perovskites. *Acta Crystallographica Section B: Structural Science*, 64(6):702–707, 2008. ISSN 01087681. doi:10.1107/S0108768108032734.

[39] NREL Best Research-Cell Efficiencies Chart. URL https://www.nrel.gov/pv/cell-efficiency.html.

[40] H. L. Wells: Uber die casium-und kalium-blei halogenide. *Zeitschrift für anorganische und allgemeine Chemie*, 3:195–210, 1893.

[41] C. K. Moller: Crystal structure and photoconductivity of caesium plumbohalides. *Nature*, 182:1436, 1958.

[42] D. Weber: $CH_3NH_3PbX_3$, ein Pb(II)-System mit kubischer Perowskitstruktur. *Zeitschrift für Naturforschung B*, 33:1443–1445, 1978. URL http://zfn.mpdl.mpg.de/data/Reihe_B/33/ZNB-1978-33b-1443.pdf.

[43] D. Weber: $CH_3NH_3PbX_3$ (x = 0-3), ein Sn (II) -System mit kubischer Perowskitstruktur. *Zeitschrift für Naturforschung B*, 33:862–865, 1978.

[44] H. J. Snaith: Present status and future prospects of perovskite photovoltaics. *Nature Materials*, 17(5):372–376, 2018. ISSN 14764660. doi:10.1038/s41563-018-0071-z. URL http://dx.doi.org/10.1038/s41563-018-0071-z.

[45] A. K. Jena, A. Kulkarni, and T. Miyasaka: Halide perovskite photovoltaics: background, status, and future prospects. *Chemical Reviews*, 119(5):3036–3103, 2019. ISSN 15206890. doi:10.1021/acs.chemrev.8b00539.

[46] T. Leijtens, K. A. Bush, R. Prasanna, and M. D. McGehee: Opportunities and challenges for tandem solar cells using metal halide perovskite semiconductors. *Nature Energy*, 3(10):828–838, 2018. ISSN 20587546. doi:10.1038/s41560-018-0190-4. URL http://dx.doi.org/10.1038/s41560-018-0190-4.

[47] F. Brivio, K. T. Butler, A. Walsh, and M. Van Schilfgaarde: Relativistic quasiparticle self-consistent electronic structure of hybrid halide perovskite photovoltaic absorbers. *Physical Review B - Condensed Matter and Materials Physics*, 89(15):1–6, 2014. ISSN 1550235X. doi:10.1103/PhysRevB.89.155204.

[48] M. Monti, S. X. Tao, M. Staniforth, A. Crocker, E. Griffin, A. Wijesekara, R. A. Hatton, and J. Lloyd-Hughes: Efficient intraband hot carrier relaxation in the perovskite semiconductor $Cs_{1-x}Rb_xSnI_3$ mediated by strong electron-phonon coupling. *Journal of Physical Chemistry C*, 122(36):20669–20675, 2018. ISSN 19327455. doi:10.1021/acs.jpcc.8b07792.

[49] G. E. Eperon, S. D. Stranks, C. Menelaou, M. B. Johnston, L. M. Herz, and H. J. Snaith: Formamidinium lead trihalide: A broadly tunable perovskite for efficient planar heterojunction solar cells. *Energy and Environmental Science*, 7(3):982–988, 2014. ISSN 17545692. doi:10.1039/c3ee43822h.

[50] M. R. Filip, G. E. Eperon, H. J. Snaith, and F. Giustino: Steric engineering of metal-halide perovskites with tunable optical band gaps. *Nature Communications*, 5, 2014. ISSN 20411723. doi:10.1038/ncomms6757.

[51] R. M. I. Bandara, K. D. G. I. Jayawardena, S. O. Adeyemo, S. J. Hinder, J. A. Smith, M. H. Thirimanne, N. C. Wong, F. M. Amin, B. G. Freestone, A. J. Parnell, D. G. Lidzey, H. J. Joyce, R. A. Sporea, and S. R. P. Silva: Tin(iv) dopant removal through anti-solvent engineering enabling tin based perovskite solar cells with high charge carrier mobilities. *Journal of Materials Chemistry C*, 7:8389–8397, 2019. doi:10.1039/c9tc02003a.

[52] K. D. G. I. Jayawardena, R. M. I. Bandara, M. Monti, E. Butler-Caddle, T. Pichler, H. Shiozawa, Z. Wang, S. Jenatsch, S. J. Hinder, M. G. Masteghin, M. Patel, H. M. Thirimanne, W. Zhang, R. A. Sporea, J. Lloyd-Hughes, and S. R. P. Silva: Approaching the Shockley-Queisser limit for fill factors in lead-tin mixed perovskite photovoltaics. *Journal of Materials Chemistry A*, 8(2):693–705, 2020. ISSN 20507496. doi:10.1039/c9ta10543c.

[53] D. W. DeQuilettes, K. Frohna, D. Emin, T. Kirchartz, V. Bulovic, D. S. Ginger, and S. D. Stranks: charge-carrier recombination in halide perovskites. *Chemical Reviews*, 119(20):11007–11019, 2019. ISSN 15206890. doi:10.1021/acs.chemrev.9b00169.

[54] D. W. DeQuilettes, S. Koch, S. Burke, R. K. Paranji, A. J. Shropshire, M. E. Ziffer, and D. S. Ginger: Photoluminescence lifetimes exceeding 8 μs and quantum yields exceeding 30% in hybrid perovskite thin films by ligand passivation. *ACS Energy Letters*, 1(2):438–444, 2016. ISSN 23808195. doi:10.1021/acsenergylett.6b00236.

[55] A. M. Leguy, A. R. Goñi, J. M. Frost, J. Skelton, F. Brivio, X. Rodríguez-Martínez, O. J. Weber, A. Pallipurath, M. I. Alonso, M. Campoy-Quiles, M. T. Weller, J. Nelson, A. Walsh, and P. R. F. Barnes: Dynamic disorder, phonon lifetimes, and the assignment of modes to the vibrational spectra of methylammonium lead halide perovskites. *Physical Chemistry Chemical Physics*, 18(39):27051–27066, 2016. ISSN 14639076. doi:10.1039/c6cp03474h.

[56] K. Miyata, D. Meggiolaro, M. Tuan Trinh, P. P. Joshi, E. Mosconi, S. C. Jones, F. De Angelis, and X. Y. Zhu: Large polarons in lead halide perovskites. *Science Advances*, 3(8):e1701217, 2017. ISSN 23752548. doi:10.1126/sciadv.1701217. URL http://advances.sciencemag.org/lookup/doi/10.1126/sciadv.1701217.

[57] K. Miyata, T. L. Atallah, and X. Y. Zhu: Lead halide perovskites: Crystal-liquid duality, phonon glass electron crystals, and large polaron formation. 2017. doi:10.1126/sciadv.1701469. URL http://advances.sciencemag.org/lookup/doi/10.1126/sciadv.1701469.

[58] H. Fröhlich: Electrons in lattice fields. *Advances in Physics*, 3(11):325–361, 1954. ISSN 14606976. doi:10.1080/00018735400101213.

[59] R. P. Feynman: Slow electrons in a polar crystal. *Physical Review*, 97(3):660–665, 1955. ISSN 0031899X. doi:10.1103/PhysRev.97.660.

[60] J. S. Manser, M. I. Saidaminov, J. A. Christians, O. M. Bakr, and P. V. Kamat: Making and breaking of lead halide perovskites. *Accounts of Chemical Research*, 49(2):330–338, 2016. ISSN 15204898. doi:10.1021/acs.accounts.5b00455.

[61] C. C. Boyd, R. Cheacharoen, T. Leijtens, and M. D. McGehee: Understanding degradation mechanisms and improving stability of perovskite photovoltaics.

Chemical Reviews, 119(5):3418–3451, 2019. ISSN 15206890. doi:10.1021/acs.chemrev.8b00336.

[62] J. Li, H. L. Cao, W. B. Jiao, Q. Wang, M. Wei, I. Cantone, J. Lü, and A. Abate: Biological impact of lead from halide perovskites reveals the risk of introducing a safe threshold. *Nature Communications*, 11(1):1–5, 2020. ISSN 20411723. doi:10.1038/s41467-019-13910-y. URL http://dx.doi.org/10.1038/s41467-019-13910-y.

[63] Q. Zhang, M. M. Tavakoli, L. Gu, D. Zhang, L. Tang, Y. Gao, J. Guo, Y. Lin, S. F. Leung, S. Poddar, Y. Fu, and Z. Fan: Efficient metal halide perovskite light-emitting diodes with significantly improved light extraction on nanophotonic substrates. *Nature Communications*, 10(1):1–9, 2019. ISSN 20411723. doi:10.1038/s41467-019-08561-y.

[64] Q. Chen, J. Wu, X. Ou, B. Huang, J. Almutlaq, A. A. Zhumekenov, X. Guan, S. Han, L. Liang, Z. Yi, J. Li, X. Xie, Y. Wang, Y. Li, D. Fan, D. B. Teh, A. H. All, O. F. Mohammed, O. M. Bakr, T. Wu, M. Bettinelli, H. Yang, W. Huang, and X. Liu: All-inorganic perovskite nanocrystal scintillators. *Nature*, 561(7721):88–93, 2018. ISSN 14764687. doi:10.1038/s41586-018-0451-1. URL http://dx.doi.org/10.1038/s41586-018-0451-1.

[65] H. Wei and J. Huang: Halide lead perovskites for ionizing radiation detection. *Nature Communications*, 10(1):1–12, 2019. ISSN 20411723. doi:10.1038/s41467-019-08981-w. URL http://dx.doi.org/10.1038/s41467-019-08981-w.

[66] Y. Dong, Y. Zou, J. Song, X. Song, and H. Zeng: Recent progress of metal halide perovskite photodetectors. *Journal of Materials Chemistry C*, 5(44):11369–11394, 2017. ISSN 20507526. doi:10.1039/c7tc03612d.

[67] J. Feng, C. Gong, H. Gao, W. Wen, Y. Gong, X. Jiang, B. Zhang, Y. Wu, Y. Wu, H. Fu, L. Jiang, and X. Zhang: Single-crystalline layered metal-halide perovskite nanowires for ultrasensitive photodetectors. *Nature Electronics*, 1(7):404–410, 2018. ISSN 25201131. doi:10.1038/s41928-018-0101-5. URL http://dx.doi.org/10.1038/s41928-018-0101-5.

[68] F. Deschler, M. Price, S. Pathak, L. E. Klintberg, D. D. Jarausch, R. Higler, S. Hüttner, T. Leijtens, S. D. Stranks, H. J. Snaith, M. Atatüre, R. T. Phillips, and R. H. Friend: High photoluminescence efficiency and optically pumped lasing in solution-processed mixed halide perovskite semiconductors. *Journal*

of Physical Chemistry Letters, 5(8):1421–1426, 2014. ISSN 19487185. doi: 10.1021/jz5005285.

[69] H. Fu: Colloidal metal halide perovskite nanocrystals: A promising juggernaut in photovoltaic applications. *Journal of Materials Chemistry A*, 7(24):14357–14379, 2019. ISSN 20507496. doi:10.1039/c8ta12509k.

[70] G. Volonakis, M. R. Filip, A. A. Haghighirad, N. Sakai, B. Wenger, H. J. Snaith, and F. Giustino: Lead-free halide double perovskites via heterovalent substitution of noble metals. *Journal of Physical Chemistry Letters*, 7(7):1254–1259, 2016. ISSN 19487185. doi:10.1021/acs.jpclett.6b00376.

[71] F. Locardi, E. Sartori, J. Buha, J. Zito, M. Prato, V. Pinchetti, M. L. Zaffalon, M. Ferretti, S. Brovelli, I. Infante, L. De Trizio, and L. Manna: Emissive bi-doped double perovskite $Cs_2Ag_{1-x}Na_xInCl_6$ nanocrystals. *ACS Energy Letters*, 4(8):1976–1982, 2019. ISSN 23808195. doi:10.1021/acsenergylett.9b01274.

[72] G. Conibeer: Third-generation photovoltaics. *Materials Today*, 10(11):42–50, 2007. ISSN 13697021. doi:10.1016/S1369-7021(07)70278-X. URL http://dx.doi.org/10.1016/S1369-7021(07)70278-X.

[73] D. Konig, K. Casalenuovo, Y. Takeda, G. Conibeer, J. F. Guillemoles, R. Patterson, L. M. Huang, and M. A. Green: Hot carrier solar cells: Principles, materials and design. *Physica E: Low-Dimensional Systems and Nanostructures*, 42(10):2862–2866, 2010. ISSN 13869477. doi:10.1016/j.physe.2009.12.032.

[74] G. Conibeer, S. Shrestha, S. Huang, R. Patterson, H. Xia, Y. Feng, P. Zhang, N. Gupta, M. Tayebjee, S. Smyth, Y. Liao, S. Lin, P. Wang, X. Dai, and S. Chung: Hot carrier solar cell absorber prerequisites and candidate material systems. *Solar Energy Materials and Solar Cells*, 135:124–129, 2015. ISSN 09270248. doi:10.1016/j.solmat.2014.11.015. URL http://dx.doi.org/10.1016/j.solmat.2014.11.015.

[75] Y. Takeda, T. Ito, T. Motohiro, D. König, S. Shrestha, and G. Conibeer: Hot carrier solar cells operating under practical conditions. *Journal of Applied Physics*, 105(7), 2009. ISSN 00218979. doi:10.1063/1.3086447.

[76] Y. Takeda, T. Motohiro, D. König, P. Aliberti, Y. Feng, S. Shrestha, and G. Conibeer: Practical factors lowering conversion efficiency of hot carrier solar cells. *Applied Physics Express*, 3(10), 2010. ISSN 18820778. doi:10.1143/APEX.3.104301.

[77] A. Le Bris and J. F. Guillemoles: Hot carrier solar cells: achievable efficiency accounting for heat losses in the absorber and through contacts. *Applied Physics Letters*, 97(11), 2010. ISSN 00036951. doi:10.1063/1.3489405.

[78] S. C. Limpert and S. P. Bremner: Hot carrier extraction using energy selective contacts and its impact on the limiting efficiency of a hot carrier solar cell. *Applied Physics Letters*, 107(7):105–108, 2015. ISSN 00036951. doi:10.1063/1.4928750. URL http://dx.doi.org/10.1063/1.4928750.

[79] P. Würfel: Solar energy conversion with hot electrons from impact ionisation. *Solar Energy Materials and Solar Cells*, 46(1):43–52, 1997. ISSN 09270248. doi:10.1016/S0927-0248(96)00092-X.

[80] G. J. Conibeer, C. W. Jiang, D. König, S. Shrestha, T. Walsh, and M. A. Green: Selective energy contacts for hot carrier solar cells. *Thin Solid Films*, 516(20):6968–6973, 2008. ISSN 00406090. doi:10.1016/j.tsf.2007.12.031.

[81] G. J. Conibeer, D. König, M. A. Green, and J. F. Guillemoles: Slowing of carrier cooling in hot carrier solar cells. *Thin Solid Films*, 516(20):6948–6953, 2008. ISSN 00406090. doi:10.1016/j.tsf.2007.12.102.

[82] G. Conibeer, N. Ekins-Daukes, J. F. Guillemoles, D. Konig, E. C. Cho, C. W. Jiang, S. Shrestha, and M. Green: Progress on hot carrier cells. *Solar Energy Materials and Solar Cells*, 93(6-7):713–719, 2009. ISSN 09270248. doi:10.1016/j.solmat.2008.09.034.

[83] D. König, D. Hiller, M. Zacharias, S. Michard, and C. Flynn: Static hot carrier populations as a function of optical excitation energy detected through energy selective contacts by optically assisted IV. *Progress in Photovoltaics: Research and Applications*, 22(10):1070–1079, 2014. ISSN 1099159X. doi:10.1002/pip.2367.

[84] M. Li, J. Fu, Q. Xu, and T. C. Sum: Slow hot-carrier cooling in halide perovskites: prospects for hot-carrier solar cells. *Advanced Materials*, 31(47):1–17, 2019. ISSN 15214095. doi:10.1002/adma.201802486.

[85] P. P. Joshi, S. F. Maehrlein, and X. Zhu: Dynamic screening and slow cooling of hot carriers in lead halide perovskites. 1803054:1–10, 2019. ISSN 09359648. doi:10.1002/adma.201803054.

[86] Y. Yang, D. P. Ostrowski, R. M. France, K. Zhu, J. Van De Lagemaat, J. M. Luther, and M. C. Beard: Observation of a hot-phonon bottleneck in lead-iodide perovskites. *Nature Photonics*, 10(1):53–59, 2016. ISSN 17494893. doi:10.1038/nphoton.2015.213.

[87] G. Xing, N. Mathews, S. S. Lim, Y. M. Lam, S. Mhaisalkar, and T. C. Sum: Long-range balanced electron- and hole-transport lengths in organic-inorganic $CH_3NH_3PbI_3$. *Science*, 342(October):344–347, 2013.

[88] M. B. Price, J. Butkus, T. C. Jellicoe, A. Sadhanala, A. Briane, J. E. Halpert, K. Broch, J. M. Hodgkiss, R. H. Friend, and F. Deschler: Hot-carrier cooling and photoinduced refractive index changes in organicinorganic lead halide perovskites. *Nature Communications*, 6:8420, 2015. ISSN 01252208. doi:10.1038/ncomms9420. URL http://www.nature.com/articles/ncomms9420.

[89] O. Flender, J. R. Klein, T. Lenzer, and K. Oum: Ultrafast photoinduced dynamics of the organolead trihalide perovskite $CH_3NH_3PbI_3$ on mesoporous TiO_2 scaffolds in the 320-920 nm range. *Physical Chemistry Chemical Physics*, 17(29):19238–19246, 2015. ISSN 14639076. doi:10.1039/c5cp01973g.

[90] Z. Guo, Y. Wan, M. Yang, J. Snaider, K. Zhu, and L. Huang: Long-range hot-carrier transport in hybrid perovskites visualized by ultrafast microscopy. *Science*, 356(6333):59–62, 2017. ISSN 10959203. doi:10.1126/science.aam7744.

[91] J. W. M. Lim, D. Giovanni, M. Righetto, M. Feng, S. G. Mhaisalkar, N. Mathews, and T. C. Sum: Hot carriers in halide perovskites: how hot truly? *The Journal of Physical Chemistry Letters*, pages 2743–2750, 2020. ISSN 1948-7185. doi:10.1021/acs.jpclett.0c00504.

[92] H. Zhu, K. Miyata, Y. Fu, J. Wang, P. P. Joshi, D. Niesner, K. W. Williams, S. Jin, and X. Y. Zhu: Screening in crystalline liquids protects energetic carriers in hybrid perovskites. *Science*, 353(6306):1409–1413, 2016. ISSN 10959203. doi:10.1126/science.aaf9570.

[93] D. Niesner, H. Zhu, K. Miyata, P. P. Joshi, T. J. S. Evans, B. J. Kudisch, M. T. Trinh, M. Marks, and X.-Y. Zhu: Persistent energetic electrons in methylammonium lead iodide perovskite thin films. *Journal of the American Chemical Society*, 138(48):15717–15726, 2016. ISSN 0002-7863. doi:10.1021/jacs.6b08880. URL http://pubs.acs.org/doi/10.1021/jacs.6b08880.

[94] T. J. Evans, K. Miyata, P. P. Joshi, S. Maehrlein, F. Liu, and X. Y. Zhu: Competition between hot-electron cooling and large polaron screening in $CsPbBr_3$

perovskite single crystals. *Journal of Physical Chemistry C*, 122(25):13724–13730, 2018. ISSN 19327455. doi:10.1021/acs.jpcc.8b00476.

[95] J. M. Frost, L. D. Whalley, and A. Walsh: Slow cooling of hot polarons in halide perovskite solar cells. *ACS Energy Letters*, 2(12):2647–2652, 2017. ISSN 2380-8195. doi:10.1021/acsenergylett.7b00862. URL http://pubs.acs.org/doi/10.1021/acsenergylett.7b00862.

[96] J. M. Richter, F. Branchi, F. Valduga De Almeida Camargo, B. Zhao, R. H. Friend, G. Cerullo, and F. Deschler: Ultrafast carrier thermalization in lead iodide perovskite probed with two-dimensional electronic spectroscopy. *Nature Communications*, 8(1):1–7, 2017. ISSN 20411723. doi:10.1038/s41467-017-00546-z. URL http://dx.doi.org/10.1038/s41467-017-00546-z.

[97] D. M. Monahan, L. Guo, J. Lin, L. Dou, P. Yang, and G. R. Fleming: Room-temperature coherent optical phonon in 2D electronic spectra of $CH_3NH_3PbI_3$ perovskite as a possible cooling bottleneck. *Journal of Physical Chemistry Letters*, 8(14):3211–3215, 2017. ISSN 19487185. doi:10.1021/acs.jpclett.7b01357.

[98] H.-Y. Hsu, C.-Y. Wang, A. Fathi, J.-W. Shiu, C.-C. Chung, P.-S. Shen, T.-F. Guo, P. Chen, Y.-P. Lee, and E. W.-G. Diau: Femtosecond excitonic relaxation dynamics of perovskite on mesoporous films of Al_2O_3 and NiO nanoparticles. *Angewandte Chemie*, 126(35):9493–9496, 2014. ISSN 0044-8249. doi:10.1002/ange.201404213.

[99] S. A. Bretschneider, F. Laquai, and M. Bonn: Trap-free hot carrier relaxation in lead-halide perovskite films. *Journal of Physical Chemistry C*, 121(21):11201–11206, 2017. ISSN 19327455. doi:10.1021/acs.jpcc.7b03992.

[100] T. R. Hopper, A. Gorodetsky, J. M. Frost, C. Müller, R. Lovrincic, and A. A. Bakulin: Ultrafast intraband spectroscopy of hot-carrier cooling in lead-halide perovskites. *ACS Energy Letters*, 3(9):2199–2205, 2018. ISSN 23808195. doi:10.1021/acsenergylett.8b01227.

[101] S. S. Lim, D. Giovanni, Q. Zhang, A. Solanki, N. F. Jamaludin, J. W. M. Lim, N. Mathews, S. Mhaisalkar, M. S. Pshenichnikov, and T. C. Sum: Hot carrier extraction in $CH_3NH_3PbI_3$ unveiled by pump-push-probe spectroscopy. *Science Advances*, 5(11):eaax3620, 2019. ISSN 2375-2548. doi:10.1126/sciadv.aax3620. URL http://advances.sciencemag.org/lookup/doi/10.1126/sciadv.aax3620.

[102] S. A. Bretschneider, I. Ivanov, H. I. Wang, K. Miyata, X. Zhu, and M. Bonn: Quantifying polaron formation and charge carrier cooling in lead-iodide perovskites. *Advanced Materials*, 30(29):1–8, 2018. ISSN 15214095. doi: 10.1002/adma.201707312.

[103] S. Nah, B. M. Spokoyny, C. M. Soe, C. C. Stoumpos, M. G. Kanatzidis, and E. Harel: Ultrafast imaging of carrier cooling in metal halide perovskite thin films. *Nano Letters*, 18(2):1044–1048, 2018. ISSN 15306992. doi:10.1021/acs.nanolett.7b04520.

[104] T. Ghosh, S. Aharon, L. Etgar, and S. Ruhman: Free carrier emergence and onset of electron-phonon coupling in methylammonium lead halide perovskite films. *Journal of the American Chemical Society*, 139(50):18262–18270, 2017. ISSN 15205126. doi:10.1021/jacs.7b09508.

[105] J. Fu, Q. Xu, G. Han, B. Wu, C. H. A. Huan, M. L. Leek, and T. C. Sum: Hot carrier cooling mechanisms in halide perovskites. *Nature Communications*, 8(1):1300, 2017. ISSN 20411723. doi:10.1038/s41467-017-01360-3. URL http://www.nature.com/articles/s41467-017-01360-3.

[106] E. Cinquanta, D. Meggiolaro, S. G. Motti, M. Gandini, M. J. Alcocer, Q. A. Akkerman, C. Vozzi, L. Manna, F. De Angelis, A. Petrozza, and S. Stagira: Ultrafast THz probe of photo-induced polarons in lead-halide perovskite. *Physical Review Letters*, 122(16):166601, 2019. ISSN 10797114. doi:10.1103/PhysRevLett.122.166601. URL https://doi.org/10.1103/PhysRevLett.122.166601.

[107] A. Burgos-Caminal, J. M. Moreno-Naranjo, A. R. Willauer, A. A. Paraecattil, A. Ajdarzadeh, and J.-E. Moser: Hot carrier mobility dynamics unravel competing sub-ps cooling processes in lead halide perovskites. *ArXiv preprint*, 2019. URL http://arxiv.org/abs/1909.04589.

[108] X. Deng, X. Wen, S. Huang, R. Sheng, T. Harada, T. W. Kee, M. Green, and A. Ho-Baillie: Ultrafast carrier dynamics in methylammonium lead bromide perovskite. *Journal of Physical Chemistry C*, 120(5):2542–2547, 2016. ISSN 19327455. doi:10.1021/acs.jpcc.5b11640.

[109] W. Chu, Q. Zheng, O. V. Prezhdo, J. Zhao, and W. A. Saidi: Low-frequency lattice phonons in halide perovskites explain high defect tolerance toward electron-hole recombination. *Science Advances*, 6(7), 2020. ISSN 23752548. doi:10.1126/sciadv.aaw7453.

[110] A. Gold-Parker, P. M. Gehring, J. M. Skelton, I. C. Smith, D. Parshall, J. M. Frost, H. I. Karunadasa, A. Walsh, and M. F. Toney: Acoustic phonon lifetimes limit thermal transport in methylammonium lead iodide. *Proceedings of the National Academy of Sciences of the United States of America*, 115(47):11905–11910, 2018. ISSN 10916490. doi:10.1073/pnas.1812227115.

[111] J. Yang, X. Wen, H. Xia, R. Sheng, Q. Ma, J. Kim, P. Tapping, T. Harada, T. W. Kee, F. Huang, Y. B. Cheng, M. Green, A. Ho-Baillie, S. Huang, S. Shrestha, R. Patterson, and G. Conibeer: Acoustic-optical phonon up-conversion and hot-phonon bottleneck in lead-halide perovskites. *Nature Communications*, 8, 2017. ISSN 20411723. doi:10.1038/ncomms14120.

[112] Q. Shen, T. S. Ripolles, J. Even, Y. Ogomi, K. Nishinaka, T. Izuishi, N. Nakazawa, Y. Zhang, C. Ding, F. Liu, T. Toyoda, K. Yoshino, T. Minemoto, K. Katayama, and S. Hayase: Slow hot carrier cooling in cesium lead iodide perovskites. *Applied Physics Letters*, 111(15), 2017. ISSN 00036951. doi:10.1063/1.4991993. URL http://dx.doi.org/10.1063/1.4991993.

[113] K. K. Chauhan, S. Prodhan, D. Ghosh, P. Waghale, S. Bhattacharyya, P. K. Dutta, and P. K. Datta: Long carrier diffusion length and slow hot carrier cooling in thin film mixed halide perovskite. *IEEE Journal of Photovoltaics*, pages 1–8, 2020. ISSN 2156-3381. doi:10.1109/jphotov.2020.2976032.

[114] H. H. Fang, S. Adjokatse, S. Shao, J. Even, and M. A. Loi: Long-lived hot-carrier light emission and large blue shift in formamidinium tin triiodide perovskites. *Nature Communications*, 9(1):243, 2018. ISSN 20411723. doi:10.1038/s41467-017-02684-w. URL http://dx.doi.org/10.1038/s41467-017-02684-w.

[115] S. D. Verma, Q. Gu, A. Sadhanala, V. Venugopalan, and A. Rao: Slow carrier cooling in hybrid Pb-Sn hHalide herovskites. *ACS Energy Letters*, 4:736–740, 2019. ISSN 2380-8195. doi:10.1021/acsenergylett.9b00251.

[116] X. Jia, J. Jiang, Y. Zhang, J. Qiu, S. Wang, Z. Chen, N. Yuan, and J. Ding: Observation of enhanced hot phonon bottleneck effect in 2D perovskites. *Applied Physics Letters*, 112(14):4–9, 2018. ISSN 00036951. doi:10.1063/1.5021679. URL http://dx.doi.org/10.1063/1.5021679.

[117] J. Butkus, P. Vashishtha, K. Chen, J. K. Gallaher, S. K. Prasad, D. Z. Metin, G. Laufersky, N. Gaston, J. E. Halpert, and J. M. Hodgkiss: The Evolution of Quantum Confinement in $CsPbBr_3$ Perovskite Nanocrystals. *Chem-*

istry of Materials, 29(8):3644–3652, 2017. ISSN 15205002. doi:10.1021/acs.chemmater.7b00478.

[118] P. Papagiorgis, L. Protesescu, M. V. Kovalenko, A. Othonos, and G. Itskos: Long-lived hot carriers in formamidinium lead iodide nanocrystals. *Journal of Physical Chemistry C*, 121(22):12434–12440, 2017. ISSN 19327455. doi:10.1021/acs.jpcc.7b02308.

[119] M. Li, S. Bhaumik, T. W. Goh, M. S. Kumar, N. Yantara, M. Grätzel, S. Mhaisalkar, N. Mathews, and T. C. Sum: Slow cooling and highly efficient extraction of hot carriers in colloidal perovskite nanocrystals. *Nature Communications*, 8:14350, 2017. ISSN 2041-1723. doi:10.1038/ncomms14350. URL http://www.nature.com/doifinder/10.1038/ncomms14350.

[120] T. R. Hopper, A. Gorodetsky, A. Jeong, F. Krieg, M. I. Bodnarchuk, M. Maimaris, M. Chaplain, T. J. Macdonald, X. Huang, R. Lovrincic, M. V. Kovalenko, and A. A. Bakulin: Hot carrier dynamics in perovskite nanocrystal solids: role of the cold carriers, nanoconfinement, and the surface. *Nano Letters*, 2020. ISSN 1530-6984. doi:10.1021/acs.nanolett.9b04491.

[121] M. Cong, B. Yang, J. Chen, F. Hong, S. Yang, W. Deng, and K. Han: Carrier multiplication and hot-carrier cooling dynamics in quantum-confined $CsPbI_3$ perovskite nanocrystals. *Journal of Physical Chemistry Letters*, 11(5):1921–1926, 2020. ISSN 19487185. doi:10.1021/acs.jpclett.0c00188.

[122] R. Ulbricht, E. Hendry, J. Shan, T. F. Heinz, and M. Bonn: Carrier dynamics in semiconductors studied with time-resolved terahertz spectroscopy. *Reviews of Modern Physics*, 83(June):543, 2011. doi:10.1103/RevModPhys.83.543.

[123] P. U. Jepsen, D. G. Cooke, and M. Koch: Terahertz spectroscopy and imaging - Modern techniques and applications. *Laser and Photonics Reviews*, 5(1):124–166, 2011. ISSN 18638880. doi:10.1002/lpor.201000011.

[124] J. B. Baxter and G. W. Guglietta: Terahertz spectroscopy. *Analytical Chemistry*, 83(12):4342–4368, 2011. ISSN 00032700. doi:10.1021/ac200907z.

[125] J. Lloyd-Hughes and T.-I. Jeon: A review of the terahertz conductivity of bulk and nano-materials. *Journal of Infrared Millimeter and Terahertz Waves*, 33:871–925, 2012. doi:10.1007/s10762-012-9905-y.

[126] J. Neu and C. A. Schmuttenmaer: Tutorial: An introduction to terahertz time domain spectroscopy (THz-TDS). *Journal of Applied Physics*, 124(23), 2018.

ISSN 10897550. doi:10.1063/1.5047659. URL http://dx.doi.org/10.1063/1.5047659.

[127] J. Lloyd-hughes: Terahertz spectroscopy of quantum 2D electron systems. *Journal of Physics D: Applied Physics*, 47:374006, 2014. doi:10.1088/0022-3727/47/37/374006.

[128] H. J. Joyce, J. L. Boland, C. L. Davies, S. A. Baig, and M. B. Johnston: A review of the electrical properties of semiconductor nanowires: insights gained from terahertz conductivity spectroscopy. *Semiconductor Science and Technology*, 31(10):103003, 2016. ISSN 0268-1242. doi:10.1088/0268-1242/31/10/103003. URL http://stacks.iop.org/0268-1242/31/i=10/a=103003?key=crossref.0ff1aa7713a8c6078d6a89906e0c9d3d.

[129] P. Kužel and H. Němec: Terahertz spectroscopy of nanomaterials: a close look at charge-carrier transport. *Advanced Optical Materials*, 8(3):1–23, 2020. ISSN 21951071. doi:10.1002/adom.201900623.

[130] M. B. Johnston and L. M. Herz: Hybrid perovskites for photovoltaics: charge-carrier recombination, diffusion, and radiative efficiencies. *Accounts of Chemical Research*, 49(1):146–154, 2016. ISSN 0001-4842. doi:10.1021/acs.accounts.5b00411. URL http://pubs.acs.org/doi/10.1021/acs.accounts.5b00411.

[131] C. D. W. Mosley, M. Failla, D. Prabhakaran, and J. Lloyd-Hughes: Terahertz spectroscopy of anisotropic materials using beams with rotatable polarization. *Scientific Reports*, 7(1):1–9, 2017. ISSN 20452322. doi:10.1038/s41598-017-12568-0. URL http://dx.doi.org/10.1038/s41598-017-12568-0.

[132] N. W. Ashcroft and N. D. Mermin: *Solid state physics*. Holt, Rinehart and Winston,, 1st edition, 1977.

[133] C. Kittel: *Introduction to solid state physics*. Wiley, 7th edition, 1996.

[134] R. L. Milot, G. E. Eperon, H. J. Snaith, M. B. Johnston, and L. M. Herz: Temperature-dependent charge-carrier dynamics in $CH_3NH_3PbI_3$ perovskite thin films. *Advanced Functional Materials*, 25(39):6218–6227, 2015. ISSN 1616301X. doi:10.1002/adfm.201502340. URL http://doi.wiley.com/10.1002/adfm.201502340.

[135] R. L. Milot, G. E. Eperon, T. Green, H. J. Snaith, M. B. Johnston, and L. M. Herz: Radiative monomolecular recombination boosts amplified spontaneous emission in $HC(NH_2)_2SnI_3$ perovskite films. *The Journal of Physical Chemistry Letters*, 7(20):4178–4184, 2016. ISSN 1948-7185. doi:10.1021/acs.jpclett.6b02030. URL http://pubs.acs.org/doi/10.1021/acs.jpclett.6b02030.

[136] R. L. Milot, M. T. Klug, C. L. Davies, Z. Wang, H. Kraus, H. J. Snaith, M. B. Johnston, and L. M. Herz: The effects of doping density and temperature on the optoelectronic properties of formamidinium tin triiodide thin tilms. *Advanced Materials*, 30(44), 2018. ISSN 15214095. doi:10.1002/adma.201804506.

[137] S. E. Ralph, Y. Chen, J. Woodall, and D. McInturff: Subpicosecond photoconductivity of $In_{0.53}Ga_{0.47}As$: intervalley scattering rates observed via THz spectroscopy. *Phys. Rev. B*, 54:5568–5573, 1996.

[138] M. C. Beard, G. M. Turner, and C. A. Schmuttenmaer: Transient photoconductivity in GaAs as measured by time-resolved terahertz spectroscopy. *Phys. Rev. B*, 62:15764–15777, 2000.

[139] R. J. Elliott: Intensity of optical absorption by excitons. *Physical Review*, 108(6):1384–1389, 1957. ISSN 0031899X. doi:10.1103/PhysRev.108.1384.

[140] M. Baranowski and P. Plochocka: Excitons in metal-halide perovskites. *Advanced Energy Materials*, 1903659, 2020. ISSN 16146840. doi:10.1002/aenm.201903659.

[141] V. D'Innocenzo, G. Grancini, M. J. Alcocer, A. R. S. Kandada, S. D. Stranks, M. M. Lee, G. Lanzani, H. J. Snaith, and A. Petrozza: Excitons versus free charges in organo-lead tri-halide perovskites. *Nature Communications*, 5:1–6, 2014. ISSN 20411723. doi:10.1038/ncomms4586.

[142] D. Huang, J. I. Chyi, and H. Morkoç: Carrier effects on the excitonic absorption in GaAs quantum-well structures: Phase-space filling. *Physical Review B*, 42(8):5147–5153, 1990. ISSN 01631829. doi:10.1103/PhysRevB.42.5147.

[143] R. K. Pathria and P. D. Beale: *Statistical mechanics*. Butterworth-Heinemann, third edition, 2011. ISBN 9780123821881.

[144] G. J. Hedley, C. Quarti, J. Harwell, O. V. Prezhdo, D. Beljonne, and I. D. Samuel: Hot-hole cooling controls the initial ultrafast relaxation in methylammonium lead iodide perovskite. *Scientific Reports*, 8(1):1–9, 2018. ISSN

20452322. doi:10.1038/s41598-018-26207-9. URL http://dx.doi.org/10.1038/s41598-018-26207-9.

[145] J. Chen, M. E. Messing, K. Zheng, and T. Pullerits: Cation dependent hot carrier cooling in halide perovskite nanocrystals. *Journal of the American Chemical Society*, page jacs.8b11867, 2019. ISSN 0002-7863. doi:10.1021/jacs.8b11867. URL http://pubs.acs.org/doi/10.1021/jacs.8b11867.

[146] E. M. Conwell: Rate of energy loss to polar modes. *Physical Review*, 143(2):657–658, 1966. ISSN 0031-899X. doi:10.1103/PhysRev.143.657. URL https://link.aps.org/doi/10.1103/PhysRev.143.657.

[147] K. Seeger: *Semiconductor physics: an introduction*. Springer Berlin Heidelberg, 9th edition, 2004. ISBN 3540219579. doi:10.1007/978-3-662-09855-4. URL http://books.google.com/books?id=il4nyDF0IJIC&pgis=1.

[148] R. H. Groeneveld, R. Sprik, and A. Lagendijk: Femtosecond spectroscopy of electron-electron and electron-phonon energy relaxation in Ag and Au. *Physical Review B*, 51(17):11433–11445, 1995. ISSN 01631829. doi:10.1103/PhysRevB.51.11433.

[149] R. D. Averitt and A. J. Taylor: Ultrafast optical and far-infrared quasiparticle. *Journal of Physics: Condensed Matter*, 14:R1357, 2002.

[150] A. G. Kontos, A. Kaltzoglou, E. Siranidi, D. Palles, G. K. Angeli, M. K. Arfanis, V. Psycharis, Y. S. Raptis, E. I. Kamitsos, P. N. Trikalitis, C. C. Stoumpos, M. G. Kanatzidis, and P. Falaras: Structural stability, vibrational properties, and photoluminescence in $CsSnI_3$ perovskite upon the addition of SnF_2. *Inorganic Chemistry*, 56(1):84–91, 2017. ISSN 0020-1669. doi:10.1021/acs.inorgchem.6b02318. URL http://pubs.acs.org/doi/10.1021/acs.inorgchem.6b02318http://pubs.acs.org/doi/abs/10.1021/acs.inorgchem.6b02318.

[151] P. Maldonado, K. Carva, M. Flammer, and P. M. Oppeneer: Theory of out-of-equilibrium ultrafast relaxation dynamics in metals. *Physical Review B*, 96(17):1–13, 2017. ISSN 24699969. doi:10.1103/PhysRevB.96.174439.

[152] Z. Lu, A. Vallabhaneni, B. Cao, and X. Ruan: Phonon branch-resolved electron-phonon coupling and the multitemperature model. *Physical Review B*, 98(13):1–8, 2018. ISSN 24699969. doi:10.1103/PhysRevB.98.134309.

[153] M. Achermann, A. P. Bartko, J. A. Hollingsworth, and V. I. Klimov: The effect of Auger heating on intraband carrier relaxation in semiconductor quantum rods. *Nature Physics*, 2(8):557–561, 2006. ISSN 1745-2473. doi:10.1038/nphys363.

[154] P. G. Klemens: Anharmonic decay of optical phonons. *Physical Review*, 148(2):845–848, 1966. ISSN 01631829. doi:10.1103/PhysRevB.11.3206.

[155] B. K. Ridley: Electron scattering by confined LO polar phonons in a quantum well. *Physical Review B - Condensed Matter and Materials Physics*, 39(8):5282–5286, 1989. ISSN 01631829. doi:10.1103/PhysRevB.39.5282.

[156] F. Vallée and F. Bogani: Coherent time-resolved investigation of LO-phonon dynamics in GaAs. *Physical Review B - Condensed Matter and Materials Physics*, 43(14):12049–12052, 1991.

[157] S. Barman and G. P. Srivastava: Long-wavelength nonequilibrium optical phonon dynamics in cubic and hexagonal semiconductors. *Physical Review B - Condensed Matter and Materials Physics*, 69:235208, 2004. ISSN 01631829. doi:10.1103/PhysRevB.69.235208.

[158] D. J. Ecsedy and P. G. Klemens: Thermal resistivity of dielectric crystals due to four-phonon processes and optical modes. *Physical Review B - Condensed Matter and Materials Physics*, 15(12):5957–5962, 1977. ISSN 1098-6596. doi:10.1017/CBO9781107415324.004.

[159] T. A. Tyson, W. Gao, Y. S. Chen, S. Ghose, and Y. Yan: Large thermal motion in halide perovskites. *Scientific Reports*, 7:9401, 2017. ISSN 20452322. doi:10.1038/s41598-017-09220-2. URL http://dx.doi.org/10.1038/s41598-017-09220-2.

[160] A. Glushkova, K. Mantulnikovs, G. Giriat, K. Semeniuk, L. Forró, E. Horváth, and A. Arakcheeva: Effect of thermal cycling on the structural evolution of methylammonium lead iodide monitored around the phase transition temperatures. *Solar RRL*, 3(7):1900044, 2019. ISSN 2367-198X. doi:10.1002/solr.201900044.

[161] J. Yang, B. D. Siempelkamp, D. Liu, and T. L. Kelly: Investigation of $CH_3NH_3PbI_3$ degradation rates and mechanisms in controlled humidity environments using in situ techniques. *ACS Nano*, 9(2):1955–1963, 2015. doi:10.1021/nn506864k.

[162] K. P. Marshall, M. Walker, R. I. Walton, and R. A. Hatton: Enhanced stability and efficiency in hole-transport-layer-free $CsSnI_3$ perovskite photovoltaics. *Nature Energy*, 1(12):16178, 2016. ISSN 2058-7546. doi:10.1038/nenergy.2016.178. URL http://www.nature.com/articles/nenergy2016178.

[163] J. H. Noh, S. H. Im, J. H. Heo, T. N. Mandal, and S. I. Seok: Chemical management for colorful, efficient, and stable inorganic-organic hybrid nanostructured solar cells. *Nano Letters*, 13:1764–1769, 2013. doi:10.1021/nl400349b.

[164] D. Sabba, H. K. Mulmudi, R. R. Prabhakar, T. Krishnamoorthy, T. Baikie, P. P. Boix, S. Mhaisalkar, and N. Mathews: Impact of anionic Br-substitution on open circuit voltage in lead free perovskite ($CsSnI_{3-x}Br_x$) solar cells. *Journal of Physical Chemistry C*, 119(4):1763–1767, 2015. ISSN 19327455. doi:10.1021/jp5126624. URL http://pubs.acs.org/doi/10.1021/jp5126624.

[165] K. P. Marshall, S. X. Tao, M. Walker, D. S. Cook, J. Lloyd-Hughes, S. Varagnolo, A. Wijesekara, D. Walker, R. I. Walton, and R. A. Hatton: $Cs_{1-x}Rb_xSnI_3$ light harvesting semiconductors for pervoskite photovoltaics. *Materials Chemistry Frontiers*, 2:1515, 2018. doi:10.1039/c8qm00159f.

[166] Y.-K. Jung, J.-H. Lee, A. Walsh, and A. Soon: Influence of Rb/Cs cation-exchange on inorganic Sn halide perovskites: from chemical structure to physical properties. *Chemistry of Materials*, 29(7):3181–3188, 2017. ISSN 0897-4756. doi:10.1021/acs.chemmater.7b00260. URL http://pubs.acs.org/doi/10.1021/acs.chemmater.7b00260.

[167] T. W. Crothers, R. L. Milot, J. B. Patel, E. S. Parrott, J. Schlipf, P. Müller-Buschbaum, M. B. Johnston, and L. M. Herz: Photon reabsorption masks intrinsic bimolecular charge-carrier recombination in $CH_3NH_3PbI_3$ perovskite. *Nano Letters*, 17(9):5782–5789, 2017. ISSN 1530-6984. doi:10.1021/acs.nanolett.7b02834. URL http://pubs.acs.org/doi/10.1021/acs.nanolett.7b02834.

[168] L.-y. Huang and W. R. L. Lambrecht: Lattice dynamics in perovskite halides $CsSnX_3$ with X = I, Br, Cl. *Physical Review B*, 90(19):195201, 2014. ISSN 1098-0121. doi:10.1103/PhysRevB.90.195201. URL https://link.aps.org/doi/10.1103/PhysRevB.90.195201.

[169] C. E. Patrick, K. W. Jacobsen, and K. S. Thygesen: Anharmonic stabilization and band gap renormalization in the perovskite $CsSnI_3$. *Physical Review B - Condensed Matter and Materials Physics*, 92(20):201205, 2015. ISSN

1550235X. doi:10.1103/PhysRevB.92.201205. URL https://link.aps.org/doi/10.1103/PhysRevB.92.201205.

[170] E. L. da Silva, J. M. Skelton, S. C. Parker, and A. Walsh: Phase stability and transformations in the halide perovskite $CsSnI_3$. *Physical Review B*, 91(14):144107, 2015. ISSN 1098-0121. doi:10.1103/PhysRevB.91.144107. URL https://link.aps.org/doi/10.1103/PhysRevB.91.144107.

[171] M. Bernardi, D. Vigil-Fowler, C. S. Ong, J. B. Neaton, and S. G. Louie: Ab initio study of hot electrons in GaAs. *Proceedings of the National Academy of Sciences of the United States of America*, 112(17):5291–6, 2015. ISSN 1091-6490. doi:10.1073/pnas.1419446112. URL http://www.ncbi.nlm.nih.gov/pubmed/25870287http://www.pubmedcentral.nih.gov/articlerender.fcgi?artid=PMC4418885.

[172] M. Saliba, T. Matsui, J. Y. Seo, K. Domanski, J. P. Correa-Baena, M. K. Nazeeruddin, S. M. Zakeeruddin, W. Tress, A. Abate, A. Hagfeldt, and M. Grätzel: Cesium-containing triple cation perovskite solar cells: Improved stability, reproducibility and high efficiency. *Energy and Environmental Science*, 9(6):1989–1997, 2016. ISSN 17545706. doi:10.1039/c5ee03874j.

[173] B. Zhao, M. Abdi-jalebi, M. Tabachnyk, H. Glass, V. S. Kamboj, W. Nie, A. J. Pearson, Y. Puttisong, K. C. Gödel, H. E. Beere, D. A. Ritchie, A. D. Mohite, S. E. Dutton, and R. H. Friend: High open-circuit voltages in tin-rich low-bandgap perovskite-based planar heterojunction photovoltaics. *Advanced Materials*, 29:1604744, 2017. doi:10.1002/adma.201604744.

[174] T.-b. Song, T. Yokoyama, C. C. Stoumpos, J. Logsdon, D. H. Cao, M. R. Wasielewski, S. Aramaki, and M. G. Kanatzidis: Importance of reducing vapor atmosphere in the fabrication of tin-based perovskite solar cells. *Journal of the American Chemical Society*, 139:836–842, 2017. doi:10.1021/jacs.6b10734.

[175] E. S. Parrott, T. Green, R. L. Milot, M. B. Johnston, H. J. Snaith, and L. M. Herz: Interplay of structural and optoelectronic properties in formamidinium mixed tinlead triiodide perovskites. *Advanced Functional Materials*, 28(33):1–11, 2018. ISSN 16163028. doi:10.1002/adfm.201802803.

[176] C. Hamaguchi: *Basic semiconductors physics*. Springer International Publishing, 3rd edition, 2017. ISBN 9783319668604.

[177] F. Hao, C. C. Stoumpos, R. P. H. Chang, and M. G. Kanatzidis: Anomalous band gap behavior in mixed Sn and Pb perovskites enables broadening of

absorption spectrum in solar cells. *Journal of the American Chemical Society*, 136:8094–8099, 2014. doi:10.1021/ja5033259.

[178] G. E. Eperon, T. Leijtens, K. A. Bush, R. Prasanna, T. Green, J. T. W. Wang, D. P. McMeekin, G. Volonakis, R. L. Milot, R. May, A. Palmstrom, D. J. Slotcavage, R. A. Belisle, J. B. Patel, E. S. Parrott, R. J. Sutton, W. Ma, F. Moghadam, B. Conings, A. Babayigit, H. G. Boyen, S. Bent, F. Giustino, L. M. Herz, M. B. Johnston, M. D. McGehee, and H. J. Snaith: Perovskite-perovskite tandem photovoltaics with optimized band gaps. *Science*, 354(6314):861–865, 2016. ISSN 10959203. doi:10.1126/science.aaf9717.

[179] J. Im, C. C. Stoumpos, H. Jin, A. J. Freeman, and M. G. Kanatzidis: Antagonism between spin-orbit coupling and steric effects causes anomalous band gap evolution in the perovskite photovoltaic materials $CH_3NH_3Sn_{1-x}Pb_xI_3$. *Journal of Physical Chemistry Letters*, 6(17):3503–3509, 2015. ISSN 19487185. doi:10.1021/acs.jpclett.5b01738.

[180] J. A. Van Vechten and T. K. Bergstresser: Electronic structures of semiconductor alloys. *Physical Review B - Condensed Matter and Materials Physics*, 1(8):3351, 1970.

[181] L. Vegard: Die Konstitution der Mischkristalle und die Raumffillung der Atome. *Zeitschrift für Physik*, 5:17–26, 1921. ISSN 00222461. doi:10.1007/BF00549722.

[182] O. J. Weber, B. Charles, and M. T. Weller: Phase behaviour and composition in the formamidinium methylammonium hybrid lead iodide perovskite solid solution . 4:15375–15382, 2016. doi:10.1039/c6ta06607k.

[183] W. Rehman, D. P. Mcmeekin, J. B. Patel, R. L. Milot, M. B. Johnston, H. J. Snaith, and L. M. Herz: Photovoltaic mixed-cation lead mixed-halide perovskites: links between crystallinity, photo-stability and electronic properties. *Energy and Environmental Science*, 10:361–369, 2017. doi:10.1039/c6ee03014a.

[184] J. Feng: Mechanical properties of hybrid organic-inorganic $CH_3NH_3BX_3$ (B = Sn, Pb; X = Br, I) perovskites for solar cell absorbers. *APL Materials*, 2(8), 2014. ISSN 2166532X. doi:10.1063/1.4885256. URL http://dx.doi.org/10.1063/1.4885256.

[185] T. Ashley, L. Buckle, S. Datta, M. T. Emeny, D. G. Hayes, K. P. Hilton, R. Jefferies, T. Martin, T. J. Phillips, D. J. Wallis, P. J. Wilding, and R. Chau:

Heterogeneous InSb quantum well transistors on silicon for ultra-high speed , low power logic applications. *Eelectronics Letters*, 43(14):5–6, 2007. doi: 10.1049/el.

[186] K. Ueno, E. G. Camargo, T. Morishita, Y. Moriyasu, H. Goto, and N. Kuze: Uncooled InSb mid-infrared LED used dislocation filtering of AlInSb layer. *Journal of Crystal Growth*, 323(1):463–465, 2011. ISSN 0022-0248. doi:10.1016/j.jcrysgro.2010.11.072. URL http://dx.doi.org/10.1016/j.jcrysgro.2010.11.072.

[187] A. M. Gilbertson, M. Fearn, J. H. Jefferson, B. N. Murdin, P. D. Buckle, and L. F. Cohen: Zero-field spin splitting and spin lifetime in n-InSb/$In_{1x}Al_xSb$ asymmetric quantum well heterostructures. *Physical Review B - Condensed Matter and Materials Physics*, 77:165335, 2008. doi:10.1103/PhysRevB.77.165335.

[188] J. A. Alamo: Nanometre-scale electronics with III-V compound semiconductors. *Nature*, 479:316–323, 2011. doi:10.1038/nature10677.

[189] T. Ashley, A. R. Barnes, L. Buckle, S. Datta, A. B. Dean, M. T. Emeny, M. Fearn, D. G. Hayes, K. P. Hilton, R. Jefferies, T. Martin, K. J. Nash, T. J. Phillips, W. H. A. Tang, P. J. Wilding, and R. Chau: Novel InSb-based quantum well transistors for ultra-high speed, low power logic applications. In *Proceedings. 7th International Conference on Solid-State and Integrated Circuits Technology*, pages 2253–2256. Beijing, China, 2004. ISBN 078038511X.

[190] B. Nedniyom, R. J. Nicholas, M. T. Emeny, L. Buckle, A. M. Gilbertson, P. D. Buckle, and T. Ashley: Giant enhanced g-factors in an InSb two-dimensional gas. *Physical Review B - Condensed Matter and Materials Physics*, 80(12):1–5, 2009. ISSN 10980121. doi:10.1103/PhysRevB.80.125328.

[191] W. Zawadzki: Electron transport phenomena in small-gap semiconductors. *Advances in Physics*, 23:435–522, 1973. doi:10.1080/00018737400101371.

[192] E. O. Kane: Band structure of indium antimonide. *J. Phys. Chem. Solids.*, 1:249–261, 1957.

[193] J. Lloyd-Hughes: Generalized conductivity model for polar semiconductors at terahertz frequencies. *Applied Physics Letters*, 100(12):122103, 2012. ISSN 00036951. doi:10.1063/1.3695161. URL http://link.aip.org/link/?APPLAB/100/122103/1.

[194] Lmfit package v1.0.0. URL https://lmfit.github.io/lmfit-py/.

[195] J. Lloyd-Hughes, M. Failla, J. Ye, S. P. P. Jones, K. L. Teo, and C. Jagadish: Interfacial and bulk polaron masses in $Zn_{1x}Mg_xO$/ZnO heterostructures examined by terahertz time-domain cyclotron spectroscopy. *Applied Physics Letters*, 106:202103, 2015. doi:10.1063/1.4921469.

[196] Z. G. Zhu, T. Low, M. F. Li, W. J. Fan, P. Bai, D. L. Kwong, and G. Samudra: Pseudo-potential band structure calculation of InSb ultra-thin films and its application to assess the n-metal-oxide-semiconductor transistor performance. *Semiconductor Science and Technology*, 23(2), 2008. ISSN 02681242. doi: 10.1088/0268-1242/23/2/025009.

[197] M. Failla, M. Myronov, C. Morrison, D. R. Leadley, and J. Lloyd-Hughes: Narrow heavy-hole cyclotron resonances split by the cubic Rashba spin-orbit interaction in strained germanium quantum wells. *Physical Review B - Condensed Matter and Materials Physics*, 92:045303, 2015. doi:10.1103/PhysRevB.92.045303.

[198] A. A. Sutanto, N. Drigo, V. I. Queloz, I. Garcia-Benito, A. R. Kirmani, L. J. Richter, P. A. Schouwink, K. T. Cho, S. Paek, M. K. Nazeeruddin, and G. Grancini: Dynamical evolution of the 2D/3D interface: A hidden driver behind perovskite solar cell instability. *Journal of Materials Chemistry A*, 8(5):2343–2348, 2020. ISSN 20507496. doi:10.1039/c9ta12489f.

[199] A. M. Gilbertson, W. R. Branford, M. Fearn, L. Buckle, P. D. Buckle, T. Ashley, and L. F. Cohen: Zero-field spin splitting and spin-dependent broadening in high-mobility InSb/$In_{1x}Al_xSb$ asymmetric quantum well heterostructures. *Physical Review B - Condensed Matter and Materials Physics*, 79:235333, 2009. doi:10.1103/PhysRevB.79.235333.

[200] S. Stachel, G. V. Budkin, U. Hagner, V. V. Bel'kov, M. M. Glazov, S. A. Tarasenko, S. K. Clowes, T. Ashley, A. M. Gilbertson, and S. D. Ganichev: Cyclotron-resonance-assisted photon drag effect in InSb / InAlSb quantum wells excited by terahertz radiation. *Physical Review B - Condensed Matter and Materials Physics*, 89:115435, 2014. doi:10.1103/PhysRevB.89.115435.

[201] I. V. Weperen, B. Tarasinski, D. Eeltink, V. S. Pribiag, S. R. Plissard, E. P. A. M. Bakkers, L. P. Kouwenhoven, and M. Wimmer: Spin-orbit interaction in InSb nanowires. *Physical Review B - Condensed Matter and Materials Physics*, 91:201413(R), 2015. doi:10.1103/PhysRevB.91.201413.

[202] D. Car, S. Conesa-boj, H. Zhang, R. L. M. Op, M. W. A. D. Moor, E. M. T. Fadaly, O. Gu, S. Ko, S. R. Plissard, V. Toresen, M. T. Wimmer, K. Watanabe, T. Taniguchi, L. P. Kouwenhoven, and E. P. A. M. Bakkers: InSb nanowires with built-in $Ga_xIn_{1-x}Sb$ tunnel barriers for majorana devices. *Nano Letters*, 17:721–727, 2017. doi:10.1021/acs.nanolett.6b03835.